



universität
wien

DISSERTATION

Titel der Dissertation

„The effect of strain heterogeneities on Rb–Sr and Sm–Nd
isotopic re–equilibration in minerals and rocks“

Verfasser

Diplom–Geologe Tobias Eberlei

angestrebter akademischer Grad

Doktor der Naturwissenschaften (Dr.rer.nat.)

Wien, 2014

Studienkennzahl lt. Studienblatt:

A 796 605 426

Dissertationsgebiet lt. Studienblatt:

Erdwissenschaften

Betreuer:

Univ. Prof. Mag. Dr. Rainer Abart

„The result, therefore, of our present enquiry is, that we find no vestige of a beginning,—no prospect of an end.”

(James Hutton, 1788)



View towards the Matsch Unit in Southern Tyrol from the summit of Similaun

(Photographer: Tobias Eberlei, 19.08.2012)

Acknowledgements

Three years have passed since I came to Vienna for my dissertation. Many people deserve my thanks for making the past three years to a very instructive time, in which I learned a lot about geology and about myself.

First of all, I want to thank my supervisor Rainer Abart and my project leader Gerlinde Habler, for their valuable help and time to discuss various aspects of the project with me, for their willingness to perform detailed corrections of my paper manuscripts and for continuous motivation and encouragement. Then, I want to thank Bernhard Grasemann for many very fruitful discussions and also detailed comments on my paper manuscripts, which helped me to find my way through the complex subject.

Theo's coffee bar and the coffee group deserve a special "thank you" for a very good coffee, always open doors and, sometimes very lively, non-scientific discussions. Many thanks for discussions and support also goes to the social room "coffee bar" in the thin section laboratory. Wencke gets a very big "thank you" for always having time for discussion, coffees and, of course, the regular "Momo-evenings" in the very fine nepalese restaurant.

Sometimes, I still think back to the good old times of our 'Diplomandenzimmer' in Mainz, which helped me to come so far. Thank you guys!

Finally, my parents and my girlfriend in Germany deserve the biggest thank for their support, help and always open doors. Despite the fact that you were in Germany, and about 700 Kilometres were between us, you were always there for me. Thank you!

Table of contents

<i>Acknowledgements</i>	1
<i>Table of contents</i>	2
<i>Conference presentations</i>	3
1 Introduction	4
1.1 Deformation and Geochronology	4
1.2 Research questions and aims	11
1.3 Methodology	12
1.3.1 Electron beam microanalytics	13
1.3.2 Isotope analysis	15
1.4 Thesis structure	16
1.5 Contributions of authors, co–authors and technical staff	17
1.6 Summary of the results and conclusions	17
1.7 References	19
2 Papers and manuscripts	29
2.1 Paper #1 – printed	29
2.2 Paper #2 – under review	56
2.3 Paper #3 – in preparation	93
3 Supplementary data	121
3.1 OM and SEM	121
3.2 EPMA data	123
3.3 EBSD data	126
3.4 Sm/Nd whole–rock results	133
3.5 Mineral separate overview	134
3.6 References	135
<i>Abstract</i>	136
<i>Zusammenfassung</i>	138
<i>Curriculum vitae (CV)</i>	140

Conference presentations

- Eberlei, T., Habler, G., Grasemann, B., Thöni, M., 2012. Pre-Alpine and Alpine microfabrics in the Austroalpine crystalline basement (Matsch Unit, Italy). Geophysical Research Abstracts, 14, EGU2012–7764–2, 2012, EGU General Assembly 2012 (Poster)
- Eberlei, T., Habler, G., Grasemann, B., Thöni, M., 2012. The microstructural and mineral chemical basis for constraining the effect of deformation on the Rb–Sr system in white mica and feldspar. European Mineralogical Conference, 1, EMC2012–227–1, 2012, European Mineralogical Conference 2012 (Poster)
- Eberlei, T., Habler, G., Grasemann, B., Abart, R., 2013. Linking deformation and chemical re-equilibration: new results from the Cretaceous Vinschgau shear zone (Southern Tyrol, Italy). Geophysical Research Abstracts, 15, EGU2013–8745–1, 2013, EGU General Assembly 2013 (Poster)
- Eberlei, T., Habler, G., Abart, R., Grasemann, B., 2013. Deformation-related chemical alteration of meta-pegmatites. Goldschmidt 2013 (Florence, Italy)(Poster)
- Eberlei, T., Habler, G., Thöni, M., Schuster, R., 2013. New Rb–Sr data from Permian meta-pegmatites in the Austroalpine Matsch Unit. MinPet 2013 (Graz, Austria) (Talk)
- Eberlei, T., Habler, G., Abart, R., Grasemann, B., 2014. Plagioclase deformation in upper-greenschist facies meta-pegmatite mylonites from the Austroalpine Matsch Unit (Eastern Alps, Italy). Geophysical Research Abstracts, 16, EGU2014–11147–1, 2014, EGU General Assembly 2014 (Talk)

1 Introduction

This project is part of a doctoral school at the University of Vienna, with the title “Deformation of geological materials, the mechanical–chemical feedback and the coupling across scales”. At the same time it is embedded in a project running in the framework of the FWF–funded project I471–N19, granted to Gerlinde Habler, as part of the international research group FOR 741 D–A–CH. The main question addressed in this thesis is on deformation–assisted re–equilibration phenomena and more specifically on the effects of deformation and strain on isotopic re–equilibration on the hand specimen scale, which is an important aspect for the proper interpretation of age information derived from bulk sample isotopic analysis. Thus, general relations among deformation and isotopic re–equilibration, from which the project–specific questions and aims are derived, are highlighted first. This is followed by a presentation of the arrangement of the scientific papers, a chapter about the contribution of authors, co–authors and technical staff, a summary, the scientific papers and a supplementary data chapter.

1.1 Deformation and Geochronology

Rocks can be subjected to complex successions of deformation events, fluid infiltration and variable pressure–temperature conditions in collisional orogens and subduction zones (e.g. Etheridge et al., 1983; England and Thompson, 1984; Ranalli et al., 2005). Within natural shear zones in crustal rocks, complex relations among mineral reactions and the localization of deformation have been documented (Moecher and Wintsch, 1994; Handy and Stünitz, 2002; Tsurumi et al., 2003; Keller et al., 2004; Burlini and Bruhn, 2005; Habler et al., 2009; Oliot et al., 2010). The feedback between mineral reactions and strain localization has also been studied experimentally (de Ronde et al., 2005; Holyoke and Tullis, 2006; Goergen et al., 2008; Heidelberg et al., 2009). However, it is often difficult to decide whether the processes involved occurred simultaneously or sequentially and mutual feedbacks may appear ambiguous. The link between geochronological, petrological and microstructural information in polymetamorphic rocks is often difficult to assess, and linking an age to a specific process in a rock is commonly not a trivial task (Villa, 1998; Vance et al., 2003; Romer and Rötzler, 2011). A proper understanding of the timing and rates of processes occurring over a wide range of length and time scales inevitably requires absolute radiometric age dating.

Introduction

Diffusion and the closure temperature concept

Jäger et al. (1967) and Dodson (1973) provided a basis for the thermochronological interpretation of radiogenic isotope data by introducing the concept of 'blocking' and 'closure' temperature, based on the modification of the isotopic composition of a mineral by thermally activated volume diffusion. Chemical diffusion describes a transport process that is driven by macroscopic concentration gradients, according to Fick's 1st law:

$$J = -D * (\partial C / \partial x),$$

where J is the diffusion flux, the proportionality constant D is the diffusion coefficient and $(\partial C / \partial x)$ is the concentration gradient. More generally, diffusion is driven by gradients in the chemical potential ($\mu = (\partial G / \partial n_i)_{P,T,n_j \neq i}$) of the diffusing species, which is $(\partial \mu / \partial x)$. The above mentioned equation then becomes:

$$J = -L * (\partial \mu / \partial x),$$

where L is the phenomenological coefficient of diffusion. The diffusion equation relates changes in concentration of the diffusing species with time $(\partial C / \partial t)$ to the second derivative of the concentration profile with respect to distance $(\partial^2 C / \partial x^2)$; Crank, 1975). It is known as Fick's 2nd law:

$$\partial C / \partial t = D * \partial^2 C / \partial x^2.$$

As volume diffusion is a thermally activated process, diffusion generally obeys an Arrhenius relation in the form:

$$D = D_0 * \exp((-E_A + \Delta V * P) / (R * T))$$

in which D is the diffusivity, D₀ is the preexponential term, E_A the activation energy for diffusion, R the universal gas constant, T the temperature in Kelvin, ΔV the activation volume of diffusion and P the pressure (Spear, 1993). Following this relation, diffusion is exponentially increasing with temperature, but almost independent of pressure due to commonly very small activation volumes for diffusion.

While Jäger et al. (1967) and Purdy and Jäger (1976) correlated measured mineral ages with field metamorphic isogrades, and hence with temperature, Dodson (1973)

Introduction

introduced a theoretical mathematical model, assuming a grain boundary network that constantly maintains a zero concentration of the radiogenic daughter:

$$T_c = (E_A/R) / (\ln[(AR(T_c)^2 D_0)/(a^2)(E_A/(dT/dt))]),$$

where T_c is the closure temperature, E_A the activation energy for diffusion, D_0 the preexponential term, R the universal gas constant, A a factor describing the geometry of the grain, a the diffusion domain size or length scale and dT/dt the cooling rate. Consequently, the closure temperature depends not only on the activation energy E_A for diffusion, but also on the cooling rate dT/dt and on the diffusion length scale a . Consequently, allocating a unique closure temperature to one specific mineral is rather unrealistic and assuming a transitional temperature interval, where radiogenic isotopes start to accumulate within a mineral, is more appropriate. However, non-Fickian concentration profiles, enhanced diffusivities with increasing grain size and inverse relations between apparent mineral ages and grain sizes, all contradicting the above mentioned role of solely thermally activated volume diffusion, have been observed in deformed minerals (e.g. Lee, 1995). And, as deformation is very likely to have an effect on the characteristic diffusion length scale (e.g. Reddy and Potts, 1999), the interactions between deformation and isotopic re-equilibration are highlighted in more detail below.

Effects of deformation on isotopic re-equilibration

Deformation can broadly be subdivided into brittle and crystal-plastic deformation, and fluid-assisted dissolution-precipitation creep. The latter is a mechanism accommodating deformation by material dissolution at sites of relatively high local stress, transport of the dissolved matter in aqueous solutions and finally precipitation of the dissolved matter at sites of lower local stress, such as cracks, pressure shadows of porphyroclasts and kink axial planes (Wintsch and Yi, 2002; Imon et al., 2002; Passchier and Trouw, 2005). This process, also referred to as 'stress-induced solution transfer' (Vernon, 2004), is known to have a strong effect on, for example, the U-Th-Pb systematics of monazite (Wawrzenitz et al., 2012). These authors suggest using monazite, formed by stress-induced solution transfer, for dating of creep episodes linked to shear deformation.

Brittle deformation occurs by breaking of chemical bonds, fracturing, subsequent loss of cohesion and cataclastic flow (Passchier and Trouw, 2005). Cracks are macroscopically visible expressions of brittle deformation and represent lattice discontinuities that cause

Introduction

a significant macroscopic segmentation of the crystal lattice. Therefore, cracks can significantly shorten the length scale for thermally activated volume diffusion and they can act as intra-grain fast diffusion pathways. Deformation-induced neo- or recrystallization is likely to have a similar effect, and thus efficiently promote isotopic re-equilibration. This is assumed, because newly formed grains are normally significantly smaller than old grains, with shorter length scales for volume diffusion. Consequently, radiometric ages, derived from recrystallized grains, are also often interpreted to reflect the age of recrystallization-inducing deformation (e.g. George and Bartlett, 1996; Freeman et al., 1997; Müller et al., 1999, 2000; Cliff and Meffan-Main, 2003; Glodny et al., 2008; Halla and Heilimo, 2009).

Crystal-plastic deformation is related to the spatially continuous deformation of a crystal lattice by migration of point- and line defects and the formation and migration of low- and high-angle grain boundaries (Passchier and Trouw, 2005). When dislocations are able to move and accumulate within subgrain boundaries, they cause physical segmentation of the crystal lattice and hence significant shortening of the length scale for thermally activated volume diffusion. They also represent fast intragrain diffusion pathways for material exchange between intragranular domains and the grain boundary network (Hart, 1957; Love, 1964; Lee, 1995). However, before trace elements or impurity atoms can exploit such defects to leave the crystal, they must enter these intragrain fast-diffusion pathways. Therefore it is important to highlight possible interactions between (migrating) grain boundaries and such, potentially mobile, impurities. First, an impurity atom can eventually be brought passively into the fast intragrain diffusion pathway network by migrating grain boundaries (planar defects), sweeping across it, during dynamic grain boundary migration recrystallization (e.g. Humphreys and Hatherly, 2004). Second, planar defects that consist of an array of dislocations and their associated stress fields can affect the chemical potentials of impurity atoms (e.g. Larch and Cahn, 1985; MacDonald et al., 2013). As such, impurity atoms tend to migrate actively towards planar defects. Small local stress fields in the crystal lattice around them, which are caused by their large ionic radii, are consequently compensated through a stress release at the sites of the defects. In fact, elevated Ar concentrations at or near defect sites in muscovite (Mulch et al., 2002) and elevated trace element concentrations at similarly distorted lattice sites in zircon have been documented (MacDonald et al., 2013), basically supporting processes as mentioned above. The effect of higher trace element concentrations at or near defect sites was first

Introduction

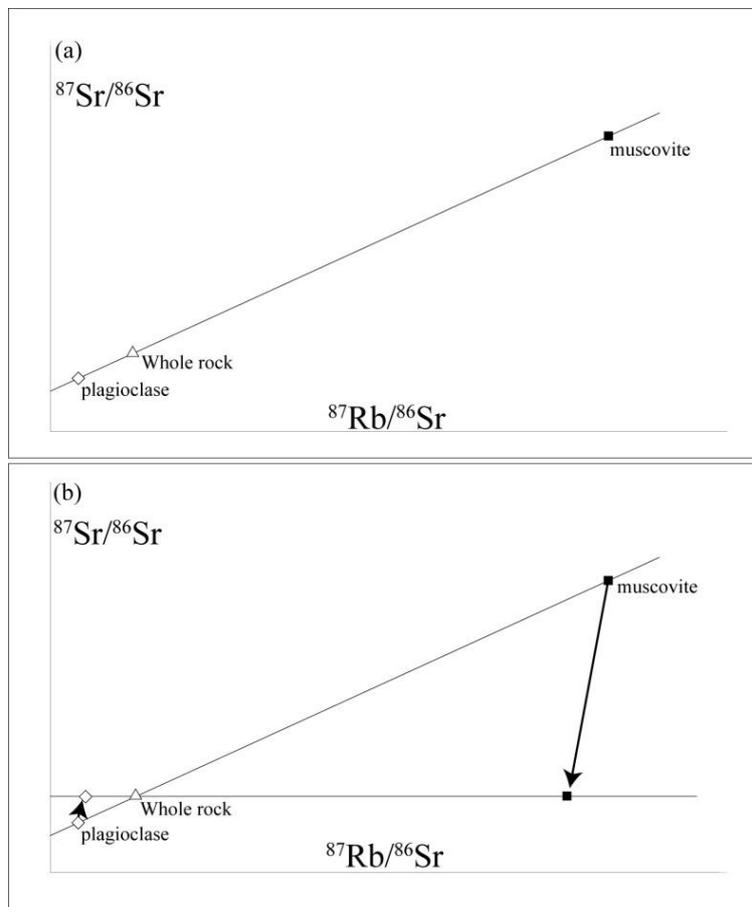
documented by Cottrell and Bilby (1949) in non-geological materials and later termed 'Cottrell atmosphere' by Takeuchi and Argon (1979). In combination with the role of line- and planar defects in shortening the length scales for volume diffusion and as acting as fast diffusion pathways, such processes can explain the increased bulk diffusivities observed in plastically deformed minerals (e.g. Lee, 1995). Since the first discovery of crystal-plastic deformation and associated planar crystal lattice defects in zircon for example, and their role in enhancing the chemical bulk diffusivity (Reddy et al., 2006), more studies have described a profound effect of crystal-plastic deformation and associated crystal lattice defects on enhancing the bulk diffusivity, a modification of the trace element geochemistry and the U-Pb isotopic system in this accessory mineral (Reddy et al., 2007; Reddy et al., 2009; MacDonald et al., 2013). In sheet silicates comparable relations between crystal-plastic deformation, associated lattice defects, including dislocations, subgrain walls and stacking faults, and the Ar-retentivity have been observed. Similar to the above mentioned relations in zircon, line- and planar defects and stacking faults with their net dilatation effect, are known to behave as fast diffusion pathways for Ar (e.g. Lee, 1995; Reddy and Potts, 1999; Dunlap and Kronenberg, 2001; Kramar et al., 2001, 2003; Mulch et al., 2002, 2005; Cosca et al., 2011). Contrastingly, garnet was shown to have a more refractory major and trace element composition during deformation and at high temperatures (Mezger et al., 1992; Habler and Thöni, 2001; Thöni and Miller, 2004; Habler et al., 2007). This probably relates to the high temperatures required for crystal-plastic deformation (e.g. Bestmann et al., 2008) and volume diffusion (e.g. Ganguly et al., 1998) in garnet. Due to these properties, garnet is often used to reconstruct pressure-temperature-time paths of metamorphic rocks (e.g. Spear, 1993).

The Rb-Sr isotopic system in deformed muscovite and analytical approaches

It still remains unclear how the Rb-Sr geochronometer of muscovite reacts to brittle and crystal-plastic deformation. Although Glodny et al. (1998) identified crystal-plastic deformation and slight lattice bending at elevated crustal temperatures of up to 600°C as the major cause for the re-opening of the Rb-Sr isotopic system of primary muscovite, a detailed description of the mechanisms affecting this isotopic system, is not provided. Additionally, it is stated that petrographic relics in a sample also contain isotopic relics (e.g. Glodny et al., 2008). Certainly, it is important to unravel such relations, because muscovite is not only an important microstructural indicator (e.g. Lister and Snoke,

Introduction

1984; ten Grotenhuis et al., 2003). It is also used in petrological applications (e.g. Coggon and Holland, 2002; Keller et al., 2005) and in geochronological studies by the dating of cooling through $c.550\text{--}500^\circ\text{C}$ (Purdy and Jäger, 1967; Blanckenburg et al., 1989; Freeman et al., 1997) and recrystallization, and thus deformation, below that temperature (e.g. Cliff and Meffan–Main, 2003). The Rb–Sr isotopic system is based on the β^- -decay of ^{87}Rb and the formation of radiogenic ^{87}Sr with a decay constant of $\lambda = 1.42 \cdot 10^{-11} \text{a}^{-1}$ (Steiger and Jäger, 1977). As Rb replaces K in the interlayer site of muscovite, while Sr does not enter the crystal structure of muscovite easily (e.g. Tischendorf et al., 2007), the potentially resulting high $^{87}\text{Rb}/^{86}\text{Sr}$ ratios make muscovite a suitable mineral for precise dating by this method. Besides the fractionation of Rb and Sr in muscovite, a further very important prerequisite for successful dating is initial isotopic homogeneity of the $^{87}\text{Sr}/^{86}\text{Sr}$ ratios among different minerals and the whole rock system. Furthermore, for a proper and complete analysis, the present-day $^{87}\text{Sr}/^{86}\text{Sr}$ and $^{87}\text{Rb}/^{86}\text{Sr}$ ratios of muscovite together with the ratios of one or better more other minerals or the whole rock must be plotted in a $^{87}\text{Sr}/^{86}\text{Sr}$ vs $^{87}\text{Rb}/^{86}\text{Sr}$ diagram (Fig. 1.1a).



Introduction

Figure 1.1 (previous page) (a) Hypothetical muscovite, plagioclase and whole rock isochron in a $^{87}\text{Rb}/^{86}\text{Sr}$ vs $^{87}\text{Sr}/^{86}\text{Sr}$ (Nicolaysen–)diagram (Nicolaysen, 1961) and (b) a hypothetical scenario of isotopic re–equilibration with homogenization of the $^{87}\text{Sr}/^{86}\text{Sr}$ ratios (modified from Dickin, 2005).

This type of diagram was first introduced by Nicolaysen (1961). The line connecting the points is called isochron and is described by the following equation:

$$(^{87}\text{Sr}/^{86}\text{Sr})_{\text{present}} = (^{87}\text{Sr}/^{86}\text{Sr})_{\text{initial}} + (^{87}\text{Rb}/^{86}\text{Sr})_{\text{present}} * (e^{\lambda t} - 1).$$

The slope of the isochron equals $(e^{\lambda t} - 1)$, and thus the amount of time t , since the radiogenic daughter product became immobile and the intercept with the $^{87}\text{Sr}/^{86}\text{Sr}$ axis marks the initial $^{87}\text{Sr}/^{86}\text{Sr}$ ratio. With at least two points or an educated guess for the initial $^{87}\text{Sr}/^{86}\text{Sr}$ ratio, an age can be calculated rearranging this equation to:

$$t = 1 / \lambda * \ln[(((^{87}\text{Sr}/^{86}\text{Sr})_{\text{present}} - (^{87}\text{Sr}/^{86}\text{Sr})_{\text{initial}}) / (^{87}\text{Rb}/^{86}\text{Sr})_{\text{present}}) + 1].$$

However, it remains unclear how the system is affected and how it re–equilibrates during deformation (cf. Glodny et al., 1998). Existing models of isotopic re–equilibration (e.g. Dickin, 2005; Faure and Mensing, 2005) are based on a rehomogenization of the $^{87}\text{Sr}/^{86}\text{Sr}$ ratios, and consequently a back rotation of the isochron into a horizontal orientation (Fig. 1.1b). In this case, the direction of the arrows, denoting the movement direction of single data during re–equilibration is rather arbitrary (cf. Fig. 1.1b). Especially during deformation, the points could theoretically move in any direction, and hence ‘artificially’ steepen or flatten the isochron, due to, possibly fluid–assisted, supply or removal of Rb or Sr or isotopic alteration.

To approach relations between deformation and Rb–Sr isotopic re–equilibration, several authors have used the microsampling technique for microstructurally controlled sampling of white mica on the grain–scale (e.g. Müller et al., 2000; Cliff and Meffan–Main, 2003; Müller, 2003; Meffan–Main et al., 2004; Charlier et al., 2006; Schneider et al., 2013). Unfortunately, this method remains problematic, due to small sample volumes of only a few μg . Furthermore, isobaric interferences of ^{87}Rb and ^{87}Sr impede the possibility to perform in–situ Rb–Sr dating by, for example, LA–ICP–MS (laser ablation inductively coupled plasma mass spectrometry). An alternative approach to this problem and microstructurally controlled sampling is the use of dynamic reaction cell ICP mass spectrometry for the in–situ Rb–Sr age determination (Vanhaecke et al., 2003). With this method, chemical separation of Rb and Sr is no longer necessary. Determination of the $^{87}\text{Sr}/^{86}\text{Sr}$ ratio without isobaric interferences is achieved by

Introduction

monitoring the signals of SrF^+ ions, that form from a selective reaction of Sr^+ with the reaction gas CH_3F (Vanhaecke et al., 2003). However, this method is still far from being available for routine age dating and the bulk sample isotopic analysis method and ID-TIMS is still the common approach of choice.

1.2 Research questions and aims

In the frame of the initially introduced topic of the effects of strain on isotopic re-equilibration on the hand specimen scale, this study focuses on the effects of deformation on the Rb–Sr isotopic system of muscovite and the mechanisms by which this isotope system is affected during deformation. More specifically, the project focus is on studying the stability of deformed, relic magmatic muscovite clasts from Permian meta-pegmatite with respect to Rb–Sr isotopic and chemical alteration (Fig. 1.2). The studied rocks stem from the Upper–Austroalpine Matsch Unit in Southern Tyrol and formed during the time interval 280–263 Ma, as derived from Sm–Nd garnet–whole rock isotopic data (Habler et al., 2009). The rocks were then deformed during Cretaceous upper–greenschist facies tectonometamorphism culminating at *c.*500°C and 4 kbar (Schmid and Haas, 1989; Habler et al., 2009). To approach the above mentioned problem and major overarching question of this study, concerning the effects of deformation on the Rb–Sr isotope system of muscovite, detailed microstructural and compositional mineral chemical analysis not only of muscovite, but also of albite feldspar and quartz, the major rock–forming minerals, are required. This is necessary to adequately characterize the deformation behaviour and related chemical alteration of these minerals and to evaluate the behaviour of the bulk rock system during Cretaceous deformation. Consequently, a set of questions is raised to outline the aims of this thesis:

- (1)** What are the main mechanisms accommodating deformation of the major rock–forming minerals albite feldspar and muscovite, and **(2)** how are different deformation mechanisms related with each other?
- (3)** How are different deformation–related microstructures especially in muscovite related with chemical alteration, and **(4)** how do major and trace element composition of dated muscovite correlate with isotopic composition and thus with deformation?
- (5)** Is the Rb–Sr geochronometer of muscovite significantly affected during deformation? **(6)** If yes, is this caused by a supply or removal of either Rb or Sr or an isotopic alteration? **(7)** Did the corresponding whole rock systems behave as open or as

Introduction

closed systems during deformation? **(8)** Can different well-characterized muscovite grain size- and magnet fractions provide information on the tectonometamorphic event and its timing?



Figure 1.2 Centimetre-sized muscovite clast in a quartz-feldspar matrix of a weakly foliated Permian meta-pegmatite from the Upper-Austroalpine Matsch Unit in Southern Tyrol (Italy) (Photographer: Tobias Eberlei, Autumn 2013)

In-situ $^{40}\text{Ar}/^{39}\text{Ar}$ spot age data of relic magmatic muscovite from two selected rocks were also collected for comparison with the Rb-Sr data and to constrain the lower age limit of the Cretaceous event.

The latter of the above mentioned aims of the collected Ar-dataset is based on the assumption of a closure temperature T_c for Ar diffusion in muscovite in the range of $c.350\text{--}400^\circ\text{C}$ (Purdy and Jäger, 1976; Steiger and Jäger, 1977). Although this value should be considered carefully (e.g. McDougall and Harrison, 1999), it is assumed to be below the Cretaceous metamorphic temperatures of 500°C (Schmid and Haas, 1989; Habler et al., 2009).

1.3 Methodology

Microstructural and textural characterization of the deformation behaviour of quartz, albite feldspar and muscovite was performed applying the electron backscatter diffraction method (EBSD). Compositional mineral analysis were performed using the electron probe microanalyzer (EPMA). The Rb-Sr isotopic systematics of different well-characterized grain size- and magnet fractions of muscovite and the corresponding

Introduction

Permian meta-pegmatite whole rocks was analyzed using the isotope dilution method and the thermal ionization mass spectrometer (ID-TIMS). A brief introduction into $^{40}\text{Ar}/^{39}\text{Ar}$ geochronology is given below. However, details of the analytical method and the sample specific settings of the in-situ $^{40}\text{Ar}/^{39}\text{Ar}$ spot dating are given in the methodology section of paper manuscript #3.

1.3.1 Electron beam microanalytics

Electron Probe Microanalysis (EMPA)

Quantitative compositional mineral analyses and element distribution maps of the major rock-forming minerals were performed using a CAMECA SX100 electron microprobe at the Center for Earth Sciences of the University of Vienna. Natural and synthetic oxides and silicates were used as standards for calibration.

The quantitative composition analysis is based on wavelength dispersive X-ray spectrometry (WDS). As the electron beam hits the sample surface at an angle of 90° , the emission of element-specific X-rays is initiated. After passing through a collimator, X-rays of one specific wavelength are diffracted on an analyzer crystal in a fixed position according to Bragg's law:

$$n * \lambda = 2 * d * \sin\theta,$$

where n is an integer, λ is the wavelength of the incident wave, d is the spacing between planes of the crystal lattice and θ is the angle between the incident beam and the crystal lattice planes. Thus, the analysis is only possible by sequentially moving the analysator crystal through different positions or using a set of different analysator crystals in different positions simultaneously. The quantitative compositional analysis of minerals is consequently based on the transformation of the intensity of the detected signal into concentrations by calibration against standards of known composition and the application of certain correction procedures. Energy-dispersive spectrometry (EDS) was used to pre-characterize fine-grained phases and inclusions in porphyroclasts. EDS has a lower compositional resolution as WDS. However, EDS is faster, because the entire spectrum can be analysed at one time. Mineral specific analytical settings are given in the respective methodology section of the papers.

Introduction

Microstructural and textural analysis

Electron backscatter diffraction analysis (EBSD) in a scanning electron microscope provides microstructural and crystallographic orientation information at high spatial resolution from relatively large sample areas (Prior et al., 1999; Schwarzer et al., 2009; Prior et al., 2009). EBSD is based on coherent scattering of electrons on a crystal lattice. For the analysis, the sample has to be tilted to 70°, so that the angle between the incident electron beam and the sample surface is 20°. Some of the incident electrons are coherently scattered on crystal lattice planes according to Bragg's law:

$$n * \lambda = 2 * d * \sin\theta,$$

where n is an integer, λ is the wavelength of the incident wave, d is the spacing between planes of the crystal lattice and θ is the angle between the incident beam and the crystal lattice planes. These coherently diffracted electrons cause fluorescence on the Al-coated phosphorous screen of the EBSD detector. The consequent light signal is then collected by a CCD camera behind the phosphorous screen. The coherently diffracted electrons reflect projections of the crystal lattice onto the EBSD detector surface. The resulting EBSD pattern is commonly referred to as the Kikuchi pattern, which consists of several bands and zone axes. These can be automatically or manually indexed by comparison with reference crystal structure data. By this method, the texture and crystallographic orientation of sample material of any of the existing crystal symmetries can be analyzed at high spatial resolution of $<0.1\mu\text{m}$. In the current study, this method is used to characterize the deformation behaviour and the major mechanisms accommodating deformation of albite feldspar and muscovite in the Permian meta-pegmatites. Furthermore, quartz grain sizes, microstructures and textures are studied, in order to estimate differences in strain rates between protomylonitic and ultramylonitic samples. However, detailed EBSD-based microstructural and textural analysis of the deformation behaviour of muscovite have long been considered as problematic, due to difficulties in sample preparation and indexing (e.g. Prior et al., 2009; Dempsey et al., 2011) and are new except for single investigations (Bestmann et al., 2011). Dempsey et al. (2011) showed, that the proportion of indexed points was highest in foliation parallel sample sections. Although the resulting fabric was similar, the degree of misindexing increased with increasing angle between the sample section and the mylonitic foliation in their samples.

1.3.2 Isotope analysis

Rb–Sr analysis

The Rb–Sr isotopic systematics of different well-characterized grain size- and magnet fractions of muscovite and the corresponding Permian meta-pegmatite whole rocks was analyzed using the isotope dilution method and the thermal ionization mass spectrometer (ID–TIMS). In contrast to the dynamic reaction cell ICP mass spectrometry (Vanhaecke et al., 2003), the isotope dilution (ID) analysis method requires a chemical separation of Rb and Sr using ion exchange chromatography prior to the analysis and an accurate determination of the concentrations of Rb and Sr. The first is done to avoid isobaric interferences of ^{87}Sr and ^{87}Rb during the analysis and the second is required for a correct calculation of the $^{87}\text{Rb}/^{87}\text{Sr}$ ratio of the natural sample. For the concentration determination, the isotope dilution method is the current method of choice. This method is based on the dilution of a natural sample with an unknown amount and isotopic composition of an element with a spike solution. This spike, which is added to the sample prior to dissolution in a mixture of HF and HNO₃, contains a known amount with known isotopic composition of the same element as the sample (Dickin, 2005). In this study, a mixed ^{87}Rb – ^{84}Sr spike was used. The amount and isotopic composition of the element in the natural sample can then be calculated from the measured isotope ratio and the known amount and isotopic composition of the spike. The resulting isotopic composition of at least two sample fractions can then be used to calculate an isochron age, as described above.

$^{40}\text{Ar}/^{39}\text{Ar}$ analysis

In principle, the $^{40}\text{Ar}/^{39}\text{Ar}$ dating method is a derivative of the K–Ar method, for which a general disadvantage is the often inhomogeneous distribution of radiogenic ^{40}Ar and the fact that K and Ar are measured on separate aliquotes of the same sample. Thus, to avoid this and to be able to analyze grain-internal variations of radiogenic ^{40}Ar , ^{39}K is transferred in-situ to ^{39}Ar during irradiation with fast neutrons in a nuclear reactor. With an half-life of 269 years, ^{39}Ar can be considered to be stable during the analytical period (Dickin, 2005). As neutron flux during irradiation is commonly not constant, the analysis of standards with known ages is required. For the samples with known ages, correction factors (J) are obtained, which are then used to interpolate J values for the

Introduction

sample with the unknown age in the nuclear reactor (e.g. Faure and Mensing, 2005). The age of the mineral to be dated can then be calculated according to:

$$t = (1 / \lambda) * \ln[(^{40}\text{Ar}/^{39}\text{Ar}) * J + 1].$$

The $^{40}\text{Ar}/^{39}\text{Ar}$ method was first applied by Merrihue and Turner (1966), and since then widely used in geochronology and thermochronology (e.g. McDougall and Harrison, 1999).

1.4 Thesis structure

The thesis is composed of three scientific papers or manuscripts for submission in peer-reviewed journals, each focusing on different aspects and questions of the project mentioned above. The deformation behaviour of rock-forming albite feldspar porphyroclasts, highlighting the role of the relative orientation between crystallographic anisotropies and the kinematic frame and dissolution-precipitation-related chemical alteration are explored in paper #1. This paper is entitled "Upper-greenschist facies intragrain deformation of albite in mylonitic meta-pegmatite and the influence of crystallographic anisotropy on microstructure formation". The paper has been published in the *Journal of Structural Geology* (Eberlei et al., 2014). The isotopic and compositional characteristics and the mechanisms of alteration of the Rb-Sr isotope systematics of Permian relic magmatic muscovite are discussed in paper #2. This paper has been submitted to *Lithos* with the title "Rb/Sr isotopic and compositional retentivity during deformation" on September 30th, 2014 and is currently under review. The EBSD-based microstructural and textural study focusing on questions concerning the deformation behaviour of muscovite is the central subject of paper #3, which is currently prepared for submission to a peer-reviewed journal. The preliminary title is "A combined EBSD- and in-situ $^{40}\text{Ar}/^{39}\text{Ar}$ study of Permian magmatic relic magmatic muscovite deformed in upper-greenschist facies Cretaceous shear zones". The thesis closes with an appendix chapter, which contains supplementary data that were not selected for the papers and manuscript. The supplementary data not only provide conclusions concerning the deformation behaviour of albite feldspar, which are similar to those presented in paper #1. They are also intended to serve as a motivation for further research on those or similar problems.

Introduction

1.5 Contributions of authors, co–authors and technical staff

Each of the co–authors in the following three scientific papers or manuscript contributed significantly to the project. Sigrid Hrabe and Claudia Beybel prepared thin sections for electron backscatter diffraction analysis and electron microprobe analysis. Franz Kiraly and Theo Ntaflos provided extensive assistance with the electron microprobe. Gerlinde Habler performed EBSD data acquisition. Wencke Wegner and Monika Horschinegg provided assistance during ID–TIMS analysis. Embedded mineral separates were produced by Franz Biedermann. ICP–OES/MS analyses of muscovite separates and whole rock powders were performed by Wilfried Körner from the Department of Environmental Geosciences at the University of Vienna. Dave Schneider from the University of Ottawa, Canada, performed in–situ $^{40}\text{Ar}/^{39}\text{Ar}$ spot dating of muscovite including sample preparation. For paper #1, Gerlinde Habler, Bernhard Grasemann and Rainer Abart contributed several interesting and fruitful ideas for sample selection as well as evaluation and interpretation of the dataset. For paper #2, Wencke Wegner, Ralf Schuster, Martin Thöni, Gerlinde Habler and Rainer Abart contributed with numerous discussions on sample preparation and the analytical strategy as well as with fruitful ideas for the evaluation and interpretation of Rb–Sr data. Paper #3 benefited extensively from ideas of Gerlinde Habler, Bernhard Grasemann and Dave Schneider. My own contributions in paper #1 comprised optical microscopy and SE–, BSE–imaging in order to select domains for EBSD investigation, the evaluation and interpretation of the data under consideration of the ideas and input by the co–authors as mentioned above and the writing and handling of the manuscript. My contributions within paper #2 comprised assistance with sample collection in the field, sample preparation, ID–TIMS and EPMA analysis, data evaluation and interpretation under consideration of the ideas and the input given by the co–authors and the writing and handling of the manuscript. Within the framework of paper #3, I performed optical microscopy as a basis for sample selection for EBSD data acquisition by Gerlinde Habler. My contributions also comprised the evaluation and interpretation of the EBSD and $^{40}\text{Ar}/^{39}\text{Ar}$ data under consideration of the work, ideas and inputs by the co–authors as mentioned above and the ID–TIMS analysis of the biotite fraction.

1.6 Summary of results and conclusions

The major question addressed in this thesis is on deformation–assisted re–equilibration phenomena and more specifically on the effects of deformation and strain on Rb–Sr

Introduction

isotopic re-equilibration in muscovite on the hand specimen scale, which is an important aspect for the proper interpretation of age information derived from bulk sample isotopic analysis. The approach includes a detailed microstructural and compositional mineral chemical analysis of the rock-forming minerals of Permian meta-pegmatites in order to adequately characterize their deformation behaviour and related chemical alteration and to evaluate the behaviour of the bulk rock system during Cretaceous deformation. The link between deformation (micro)structures and the Rb–Sr isotope systematics of muscovite is established through the major element chemical composition.

EBSD-based microstructural and textural data of this study show, that dissolution–precipitation of albite is an important mechanism accommodating deformation at upper–greenschist facies pressure–temperature conditions, and that it is intimately related with grain–internal formation of (micro)kinks, cracks, low–angle boundaries, stylolites and chemical alteration. It is shown by the data that crystallographic anisotropies in albite exert a strong control on the development of specific deformation–related microstructures as indicated by the different deformation behaviour of two clasts with different angular relations between their (010) plane and the mylonitic foliation. Contrastingly, the deformation behaviour of muscovite is obviously not controlled by the relative orientation of crystallographic anisotropies with respect to the kinematic frame, except for the preferred orientation of the (001) planes. The Y–axis of shear flow seems to be the rotation axis for crystal lattice rotation, irrespective of the initial clast orientation, confirming earlier results from Bestmann et al. (2011). Combined microstructural and mineral chemical analysis of the rock-forming minerals muscovite and albite feldspar indicate that significant portions of the Permian meta-pegmatites were affected by deformation, coupled with significant deformation–related chemical alteration of both, muscovite and albite feldspar. However, the data demonstrate that Rb–Sr isotopic data of muscovite obviously do not correlate with major element composition as deformation does. Detailed results of the Rb–Sr isotopic analysis of several well-characterized grain size– and magnet–fractions of deformed Permian relic magmatic muscovite from single samples contest existing models of isotopic rehomogenization during an overprinting event (cf. Fig. 1.1b; Faure and Mensing, 2005; Dickin, 2005). The results demonstrate that a, presumably deformation–related, loss of total Sr was found to have a significant effect on the $^{87}\text{Rb}/^{86}\text{Sr}$ ratios of muscovite without significant $^{87}\text{Sr}/^{86}\text{Sr}$ isotopic rehomogenization. Meanwhile, it is interpreted that

Introduction

the Permian meta-pegmatite whole rock systems largely remained closed during the Cretaceous. This is consistent with a poorly defined whole rock errorchron age of 257 ± 130 Ma that still supports a Permo-Triassic formation age. However, the slopes of muscovite-internal 'errorchrons', which are constructed by up to five muscovite grain size- and magnet-fractions, obviously bracket the timing of the event that affected the geochronometer. Yet another point is the presence of at least one muscovite grain size- and magnet-fraction, typically the one with the lowest $^{87}\text{Rb}/^{86}\text{Sr}$ and $^{87}\text{Sr}/^{86}\text{Sr}$ ratios, in almost every sample that is interpreted to still reflect a Permo-Triassic formation or cooling age.

In general, investigations of different grain size- and magnet-fractions from single samples provide a comprehensive dataset documenting significant systematic variations in the Rb-Sr isotopic system even at hand specimen scale. This study highlights the dependence of major and trace element, and isotope distribution on local deformation and effective deformation mechanisms.

1.7 References

- Bestmann, M., Habler, G., Heidelbach, F., Thöni, M., 2008. Dynamic recrystallization of garnet and related diffusion processes. *Journal of Structural Geology*, 30, 777–790.
- Bestmann, M., Pennacchioni, G., Frank, G., Göken, M., de Wall, H., 2011. Pseudotachylite in muscovite-bearing quartzite: Coseismic friction-induced melting and plastic deformation of quartz. *Journal of Structural Geology*, 33, 169–186.
- Blanckenburg, F.v., Villa, I., Baur, H., Morteani, G., Steiger, R.H., 1989. Time calibration of a PT-path from the Western Tauern Window, Eastern Alps: the problem of closure temperatures. *Contributions to Mineralogy and Petrology* 101, 1–11.
- Burlini, L., Bruhn, D., 2005. High-strain zones: laboratory perspectives on strain softening during ductile deformation. In: Bruhn, D., Burlini, L. (eds), 2005. *High-Strain Zones: Structure and Physical Properties*. Geological Society, London, Special Publications, 245, 1–24.

Introduction

- Charlier, B.L.A., Ginibre, C., Morgan, D., Nowell, G.M., Pearson, D.G., Davidson, J.P., Ottley, C.J., 2006. Methods for the microsampling and high-precision analysis of strontium and rubidium isotopes at single crystal scale for petrological and geochronological applications. *Chemical Geology*, 232, 114–133.
- Cliff, R.A., Meffan–Main, S., 2003. Evidence from Rb–Sr microsampling geochronology for the timing of Alpine deformation in the Sonnblick Dome, SE Tauern Window, Austria. In: Vance, D., Müller, W., Villa, I.M. (eds), 2003. *Geochronology: Linking the Isotopic Record with Petrology and Textures*. Geological Society, London, Special Publications, 220, 159–172.
- Coggon, R., Holland, T.J.B., 2002. Mixing properties of phengitic micas and revised garnet–phengite thermobarometers. *Journal of Metamorphic Geology*, 20, 683–696.
- Cosca, M., Stünitz, H., Bourgeix, A.L., Lee, J.P., 2011. $^{40}\text{Ar}^*$ loss in experimentally deformed muscovite and biotite with implications for $^{40}\text{Ar}/^{39}\text{Ar}$ geochronology of naturally deformed rocks. *Geochimica et Cosmochimica Acta*, 75, 7759–7778.
- Cottrell, A.H., Bilby, B.A., 1949. Dislocation theory of yielding and strain ageing of iron. *Proceedings of the Physical Society, London, Section A* 62(1), 49–62.
- Crank, J., 1975. *The Mathematics of Diffusion*. Oxford University Press, London, 414p.
- Dempsey, E.D, Prior, D.J., Mariani, E., Toy, V.G., Tatham, D.J., 2011. Mica-controlled anisotropy within mid-to-upper crustal mylonites: an EBSD study of mica fabrics in the Alpine Fault Zone, New Zealand. In: Prior, D.J., Rutter, E.H., Tatham, D.J. (eds), 2011. *Deformation Mechanisms, Rheology and Tectonics: Microstructures, Mechanics and Anisotropy*. Geological Society, London, Special Publications, 360, 33–47.
- Dickin, A.P., 2005. *Radiogenic Isotope Geology – 2nd edition*. Cambridge University Press, 492 p.
- Dodson, M.H., 1973. Closure Temperature in Cooling Geochronological and Petrological Systems. *Contributions to Mineralogy and Petrology* 40, 259–274.

Introduction

- Dunlap, W.J., Kronenberg, A.K., 2001. Argon loss during deformation of micas: constraints from laboratory deformation experiments. *Contributions to Mineralogy and Petrology*, 141, 174–185.
- Eberlei, T., Habler, G., Grasemann, B., Abart, R., 2014. Upper–greenschist facies intragrain deformation of albite in mylonitic meta–pegmatite and the influence of crystallographic anisotropy on microstructure formation. *Journal of Structural Geology*, 69A, 47–58.
- England, P.C., Thompson, A.B., 1984. Pressure–Temperature–time paths of regional metamorphism I. heat transfer during the evolution of regions of thickened continental crust. *Journal of Petrology*, 25(4), 894–928.
- Etheridge, M.A., Wall, V.J., Vernon, R.H., 1983. The role of the fluid phase during regional metamorphism and deformation. *Journal of Metamorphic Geology*, 1, 205–226.
- Faure, G., Mensing, T.M., 2005. *Isotopes – Principles and Applications*, 3rd edition, 897p., Wiley
- Freeman, S.R., Inger, S., Butler, R.W.H., Cliff, R.A., 1997. Dating deformation using Rb–Sr in white mica: Greenschist facies deformation ages from the Entrelor shear zone, Italian Alps. *Tectonics* 16/1, 57–76.
- Ganguly, J., Cheng, W., Chakraborty, S., 1998. Cation diffusion in aluminosilicate garnets: experimental determination in pyrope–almandine diffusion couples. *Contributions to Mineralogy and Petrology*, 131, 171–180.
- George, M.T., Bartlett, J.M., 1996. Rejuvenation of Rb–Sr mica ages during shearing on the northwestern margin of the Nanga Parbat–Haramosh massif. *Tectonophysics* 260, 167–185.
- Glodny, J., Grauert, B., Fiala, J., Vejnar, Z., Krohe, A., 1998. Metapegmatites in the western Bohemian massif: ages of crystallisation and metamorphic overprint, as constrained by U–Pb zircon, monazite, garnet, columbite and Rb–Sr muscovite data. *Geologische Rundschau*, 87, 124–134.

Introduction

- Glodny, J., Kühn, A., Austrheim, H., 2008. Diffusion versus recrystallization processes in Rb–Sr geochronology: Isotopic relics in eclogite facies rocks, Western Gneiss Region, Norway. *Geochimica et Cosmochimica Acta* 72, 506–525.
- Goergen, E.T., Whitney, D.L., Zimmerman, M.E., Hiraga, T., 2008. Deformation–induced polymorphic transformation: experimental deformation of kyanite, andalusite, and sillimanite. *Tectonophysics*, 454, 23–35.
- Habler, G., Thöni, M., 2001. Preservation of Permo–Triassic low–pressure assemblages in the Cretaceous high–pressure metamorphic Saualpe crystalline basement (Eastern Alps, Austria). *Journal of Metamorphic Geology*, 19, 679–697.
- Habler, G., Thöni, M., Miller, C., 2007. Major and trace element chemistry and Sm–Nd age correlation of magmatic pegmatite garnet overprinted by eclogite–facies metamorphism. *Chemical Geology*, 241, 4–22.
- Habler, G., Thöni, M., Grasemann, B., 2009. Cretaceous metamorphism in the Austroalpine Matsch Unit (Eastern Alps): The interrelation between deformation and chemical equilibration processes. *Mineralogy and Petrology* 97, 149–171.
- Halla, J., Heilimo, E., 2009. Deformation–induced Pb isotope exchange between K–feldspar and whole rock in Neoproterozoic granitoids: Implications for assessing Proterozoic imprints. *Chemical Geology*, 265, 303–312.
- Handy, M.R., Stünitz, H. Strain localization by fracturing and reaction weakening – a mechanism for initiating exhumation of subcontinental mantle beneath rifted margins. In: de Meer, S., Drury, M.R., de Bresser, J.H.P. (eds), 2002. *Deformation Mechanisms, Rheology and Tectonics: Current Status and Future Perspectives*. Geological Society, London, Special Publications, 200, 387–407.
- Hart, E.W., 1957. On the role of dislocations in bulk diffusion. *Acta Metallurgica*, 5(10), 597.
- Heidelberg, F., Terry, M.P., Bystricky, M., Holzapfel, C., McCammon, C., 2009. A simultaneous deformation and diffusion experiment: Quantifying the role of deformation in enhancing metamorphic reactions. *Earth and Planetary Science Letters*, 278, 386–394.

Introduction

- Holyoke III, C.W., Tullis, J., 2006. The interaction between reaction and deformation: an experimental study using a biotite + plagioclase + quartz gneiss. *Journal of Metamorphic Geology*, 24, 743–762.
- Humphreys, F.J., Hatherly, M., 2004. Recrystallization and related annealing phenomena – 2nd edition. Elsevier, 574 p.
- Imon, R., Okudaira, T., Fujimoto, A., 2002. Dissolution and precipitation processes in deformed amphibolites: an example from the ductile shear zone of the Ryoke metamorphic belt, SW Japan. *Journal of metamorphic Geology* 20, 297–308.
- Jäger, E., 1967. Die Bedeutung der Biotit–Alterswerte. In: Rb–Sr Altersbestimmungen an Glimmern der Zentralalpen. From E. Jäger, E. Niggli and E. Wenk (eds). *Beiträge zur Geologischen Karte der Schweiz*, NF, 134, 28–31.
- Keller, L.M., Abart, R., Stünitz, H., de Capitani, C., 2004. Deformation, mass transfer and mineral reactions in an eclogite facies shear zone in a polymetamorphic metapelite (Monte Rosa nappe, western Alps). *Journal of Metamorphic Geology*, 22, 97–118.
- Keller, L.M., De Capitani, C., Abart, R., 2005. A Quarternary Solution Model for White Micas Based on Natural Coexisting Phengite–Paragonite Pairs. *Journal of Petrology*, 46(10), 2129–2144.
- Kramar, N., Cosca, M.A., Hunziker, J.C., 2001. Heterogeneous ⁴⁰Ar* distributions in naturally deformed muscovite: in situ UV–laser ablation evidence for microstructurally controlled intragrain diffusion. *Earth and Planetary Science Letters*, 192, 377–388.
- Kramar, N., Cosca, M., Buffat, P.A., Baumgartner, L., 2003. Stacking fault–enhanced argon diffusion in naturally deformed muscovite. From Vance, D, Müller, W and Villa, I (eds) 2003, *Geochronology: Linking the Isotopic Record with Petrology and Textures*. Geological Society, London, Special Publications 220, 249–260.
- Larche, F.C., Cahn, J.W., 1985. The interactions of composition and stress in crystalline solids. *Acta Metallurgica*, 33(3), 331–357.
- Lee, J.K.W., 1995. Multipath diffusion in geochronology. *Contributions to Mineralogy and Petrology*, 120, 60–82.

Introduction

- Lister, G.S., Snoke, A.W., 1984. S–C mylonites. *Journal of Structural Geology*, 6, 617–638.
- Love, G.R., 1964. Dislocation Pipe Diffusion. *Acta Metallurgica*, 12, 731–737.
- MacDonald, J.M., Wheeler, J., Harley, S.L., Mariani, E., Goodenough, K.M., Crowley, Q., Tatham, D., 2013. Lattice distortion in a zircon population and its effects on trace element mobility and U–Th–Pb isotope systematics: examples from the Lewisian Gneiss Complex, northwest Scotland. *Contributions to Mineralogy and Petrology*, 166, 21–41.
- McDougall, I., Harrison, T.M., 1999. *Geochronology and Thermochronology by the $^{40}\text{Ar}/^{39}\text{Ar}$ method – 2nd edition*. Oxford University Press, 269 p.
- Meffan–Main, S., Cliff, R.A., Barnicoat, A.C., Lombardo, B., Compagnoni, R., 2004. A Tertiary age for Alpine high–pressure metamorphism in the Gran Paradiso massif, Western Alps: a Rb–Sr microsampling study. *Journal of Metamorphic Geology*, 22, 267–281.
- Merrihue, C., Turner, G., 1966. Potassium–Argon Dating by Activation with Fast Neutrons. *Journal of Geophysical Research*, 71, 2852–2857.
- Mezger, K., Essene, E.J., Halliday, A.N., 1992. Closure temperatures of the Sm–Nd system in metamorphic garnets. *Earth and Planetary Science Letters*, 113, 397–409.
- Moecher, D.P., Wintsch, R.P., 1994. Deformation–induced reconstitution and local resetting of mineral equilibria in polymetamorphic gneisses: tectonic and metamorphic implications. *Journal of Metamorphic Geology*, 12, 523–538.
- Mulch, A., Cosca, M., Handy, M., 2002. In–Situ UV–laser $^{40}\text{Ar}/^{39}\text{Ar}$ geochronology of a micaceous mylonite: an example of defect–enhanced argon loss. *Contributions to Mineralogy and Petrology* 142, 738–752.
- Mulch, A., Cosca, M.A., Andresen, Fiebig, J., 2005. Time scales of deformation and exhumation in extensional detachment systems determined by high–spatial resolution in situ UV–laser $^{40}\text{Ar}/^{39}\text{Ar}$ dating. *Earth and Planetary Science Letters*, 233, 375–390.

Introduction

- Müller, W., Dallmeyer, D., Neubauer, F., Thöni, M 1999. Deformation-induced resetting of Rb/Sr and $^{40}\text{Ar}/^{39}\text{Ar}$ mineral systems in a low-grade, polymetamorphic terrane (Eastern Alps, Austria). *Journal of the Geological Society, London* 156, 261–278.
- Müller, W., Mancktelow, N., Meier, M 2000. Rb–Sr microchrons of synkinematic mica in mylonites: an examples from the DAV fault of the Eastern Alps. *Earth and Planetary Science Letters* 180, 385–397.
- Müller, W., 2003. Strengthening the link between geochronology, textures and petrology. *Earth and Planetary Science Letters*, 206, 237–251.
- Nicolaysen, L.O., 1961. Graphic interpretation of discordant age measurements on metamorphic rocks. *Annals of the New York Academy of Sciences*, 91, 198–206.
- Oliot, E., Goncalves, P., Marquer, D., 2010. Role of plagioclase and reaction softening in a metagranite shear zone at mid-crustal conditions (Gotthard Massif, Swiss Central Alps). *Journal of Metamorphic Geology*, 28, 849–871.
- Passchier, C.W., Trouw, R.A.J., 2005. *Microtectonics*. Springer–Verlag, Berlin Heidelberg, New York, 366p.
- Prior, D.J., Boyle, A.P., Brenker, F., Cheadle, M.C., Day, A., Lopez, G., Peruzzo, L., Potts, G.J., Reddy, S., Spiess, R., Timms, N.E., Trimby, P., Wheeler, J., Zetterström, L., 1999. The application of electron backscatter diffraction and orientation contrast imaging in the SEM to textural problems in rocks. *American Mineralogist* 84, 1741–1759.
- Prior, D.J., Mariani, E., Wheeler, J., 2009. EBSD in the Earth Sciences: Applications, Common Practice, and Challenges. In: Schwartz, A.J., Kumar, M., Adams, B.L., Field, D.P., (eds), 2009. *Electron Backscatter Diffraction in Materials Science*, 2nd edition, Springer, 345–360.
- Purdy J.W., Jäger, E., 1976. K–Ar Ages on Rock-forming minerals from the Central Alps. *Memorie degli Istituti di Geologia e Mineralogia dell'Università di Padova* 30, 1–31.
- Ranalli, G., Martin, S., Mahatsente, R., 2005. Continental subduction and exhumation: an example from the Ulten Unit, Tonale Nappe, Eastern Austroalpine. In: Gapais,

Introduction

- D., Brun, J.P., Cobbold, P.R. (eds), 2005. Deformation Mechanisms, Rheology and Tectonics: from Minerals to the Lithosphere. Geological Society, London, Special Publications, 243, 159–174.
- Reddy, S.M., Potts, G.J., 1999. Constraining absolute deformation ages: the relationship between deformation mechanisms and isotope systematics. *Journal of Structural Geology*, 21, 1255–1265.
- Reddy, S.M., Timms, N.E., Trimby, P., Kinny, P.D., Buchan, C., Blake, K., 2006. Crystal–plastic deformation of zircon: A defect in the assumption of chemical robustness. *Geology*, 34, 257–260.
- Reddy, S.M., Timms, N.E., Pantleon, W., Trimby, P., 2007. Quantitative characterization of plastic deformation of zircon and geological implications. *Contributions to Mineralogy and Petrology*, 153, 625–645.
- Reddy, S.M., Timms, N.E., Hamilton, P.J., Smyth, H.R., 2009. Deformation–related microstructures in magmatic zircon and implications for diffusion. *Contributions to Mineralogy and Petrology*, 157, 231–244.
- Romer, R.L., Rötzler, J., 2011. The role of element distribution for the isotopic dating of metamorphic minerals. *European Journal of Mineralogy*, 23, 17–33.
- de Ronde, A.A., Stünitz, H., Tullis, J., Heilbronner, R., 2005. Reaction–induced weakening of plagioclase–olivine composites. *Tectonophysics*, 409, 85–106.
- Schmid, S.M., Haas, R., 1989. Transition from near–surface thrusting to intrabasement decollement, Schlinig thrust, Eastern Alps. *Tectonics* 8, 697–718.
- Schneider, S., Hammerschmidt, K., Rosenberg, C.L., 2012. Dating the longevity of ductile shear zones: Insight from $^{40}\text{Ar}/^{39}\text{Ar}$ in situ analyses. *Earth and Planetary Science Letters*, 369–370, 43–58.
- Schwarzer, R.A., Field, D.P., Adams, B.L., Kumar, M., Schwartz, A.J., 2009. Present State of Electron Backscatter Diffraction and Prospective Developments. In: Schwartz, A.J., Kumar, M., Adams, B.L., Field, D.P., (eds), 2009. *Electron Backscatter Diffraction in Materials Science*, 2nd edition, Springer, 1–20.
- Spear, F.S., 1993. *Metamorphic Phase Equilibria and Pressure–Temperature–Time Paths*. 799p., Mineralogical Society of America.

Introduction

- Steiger, R.H., Jäger, E., 1977. Subcommittee on Geochronology: Convention on the use of decay constants in geo- and cosmochronology. *Earth and Planetary Science Letters* 36, 359–362.
- Takeuchi, S., Argon, A.S., 1979. Glide and climb resistance to the motion of an edge dislocation due to dragging a Cottrell atmosphere. *Philosophical Magazine a-Physics of Condensed Matter Structure Defects and Mechanical Properties*, 40(1), 65–75.
- ten Grotenhuis, S.M., Trouw, R.A.J., Passchier, C.W., 2003. Evolution of mica fish in mylonitic rocks. *Tectonophysics*, 372, 1–21.
- Thöni, M., Miller, C., 2004. Ordovician meta-pegmatite garnet (N–W Ötztal basement, Tyrol, Eastern Alps): preservation of magmatic garnet chemistry and Sm–Nd age during mylonitization. *Chemical Geology*, 209, 1–26.
- Tischendorf, G., Förster, H.J., Gottesmann, B., Rieder, M., 2007. True and brittle micas: composition and solid–solution series. *Mineralogical Magazine*, 71(3), 285–320.
- Tsurumi, J., Hosonuma, H., Kanagawa, K., 2003. Strain localization due to a positive feedback of deformation and myrmekite-forming reaction in granite and aplite mylonites along the Hatagawa Shear Zone of NE Japan. *Journal of Structural Geology* 25, 557–574.
- Vance, D., Müller, W., Villa, I.M., 2003. Geochronology: linking the isotopic record with petrology and textures – an introduction. In: Vance, D., Müller, W., Villa, I.M. (2003). *Geochronology: Linking the Isotopic Record with Petrology and Textures*. Geological Society, London, Special Publications, 220, 1–24.
- Vanhaecke, F., Wannemacker, G., Balcaen, L., Moens, L., 2003. The use of dynamic reaction cell ICP mass spectrometry to facilitate Rb–Sr age determination. In: Vance, D., Müller, W., Villa, I.M. (2003). *Geochronology: Linking the Isotopic Record with Petrology and Textures*. Geological Society, London, Special Publications, 220, 173–181.
- Vernon, R.H., 2004. *A practical guide to Rock Microstructure*. Cambridge University Press, Cambridge, 94 p.
- Villa, I.M., 1998. Isotopic closure. *Terra Nova*, 10, 42–47.

Introduction

Wawrzenitz, N., Krohe, A., Rhede, D., Romer, R.L., 2012. Dating rock deformation with monazite: The impact of dissolution precipitation creep. *Lithos*, 134–135, 52–74.

Wintsch, R.P., Yi, K., 2002. Dissolution and replacement creep: a significant deformation mechanism in mid–crustal rocks. *Journal of Structural Geology* 24, 1179–1193.

Papers and manuscripts

2.1 Paper #1

**Upper–greenschist facies intragrain deformation of albite in mylonitic meta–
pegmatite and the influence of crystallographic anisotropy on microstructure
formation**

Tobias Eberlei, Gerlinde Habler, Bernhard Grasemann, Rainer Abart

(2014)

Journal of Structural Geology

Volume 69, Part A, Pages 47–58

DOI: 10.1016/j.jsg.2014.10.001

**Upper–greenschist facies intragrain deformation of albite in mylonitic meta–
pegmatite and the influence of crystallographic anisotropy on microstructure
formation**

Tobias Eberlei ^{a, *}, Gerlinde Habler ^a, Bernhard Grasemann ^b, Rainer Abart ^a

^a Department of Lithospheric Research, University of Vienna, Althanstraße 14, A–1090
Vienna, Austria (* Corresponding author: Tobias Eberlei; E-mail:
tobias.eberlei@univie.ac.at; phone: +43 1 4277 53362)

^b Department of Geodynamics and Sedimentology, University of Vienna, Althanstraße
14, A–1090 Vienna, Austria

E-mail addresses: gerlinde.habler@univie.ac.at (Gerlinde Habler)
bernhard.grasemann@univie.ac.at (Bernhard Grasemann)
rainer.abart@univie.ac.at (Rainer Abart)

Keywords: dissolution–precipitation, crystal plasticity, crystallographic anisotropy,
greenschist facies deformation, electron backscatter diffraction

Abstract

We studied the deformation behaviour of albite from Permian meta-pegmatite in Cretaceous upper-greenschist facies shear zones from the Austroalpine Matsch Unit in the Eastern Alps (Italy). Sodium-feldspars from these rocks provide excellent natural examples for studying mechanisms of intragranular deformation under mid-crustal conditions in grains with different angular relations between their (010) planes and the kinematic frame. The studied rocks were deformed at c. 500°C in localized shear zones with well characterized top-W shear kinematics supposedly during the Cretaceous upper-greenschist facies tectonometamorphic event. Microstructural and chemical data suggest that crystallographic anisotropies in albite exert a strong control on microstructure formation and that albite primarily deformed by a combination of brittle fracturing, dissolution-precipitation and incipient crystal plasticity as a function of the orientation of the crystallographic anisotropy relative to the supposed shortening direction. Dissolution along discontinuities forming stylolites perpendicular to the shortening direction is associated with the precipitation of fine-grained albite with some compositional variability (Ab_{96-98} and Ab_{89-91}) in cracks. New albite precipitates form aggregates with straight segments of high angle grain boundaries, nearly 120° dihedral angles and only a poor or no orientation relation to the hosting clast. Intragranular kinking is related to continuous lattice rotation of up to 15° by a misorientation axis close to albite [100] and the formation of subgrain boundaries with maximum misorientations of 7°. Synthetic microshear zones supposedly nucleated on pre-existing cracks, and are associated with formation of subgrain boundaries in shortening quadrants and cracks together with precipitates of potassium feldspar in extensional quadrants adjacent to the microshear zone. New microstructural and textural data from mylonitic Permian meta-pegmatites document various closely linked crystal plastic and brittle deformation mechanisms and highlight the role of crystallographic anisotropies and their orientation with respect to the kinematic frame in microstructure formation.

1. Introduction

Feldspars are key constituents of the Earth's crust because they are stable over a wide range of rock compositions and P-T conditions. Their deformation and recrystallization behaviour plays an important role in rheological models (e.g. Mehl and Hirth, 2008; Bürgmann and Dresen, 2008) and therefore they have received considerable attention in natural and experimental studies in the past (Vernon, 1975; Tullis and Yund, 1987;

Simpson and Wintsch, 1989; Pryer, 1993; Fitz Gerald and Stünitz, 1993; Prior and Wheeler, 1999; Jiang et al., 2000; Heidelbach et al., 2000; McLaren and Pryer, 2001; Imon et al., 2001; Tsurumi et al., 2003; Menegon et al., 2006; McLaren and Reddy, 2008; Menegon et al., 2013), covering a wide spectrum of crustal P–T conditions, at greenschist facies (Prior and Wheeler, 1999; Jiang et al., 2000), amphibolite facies (Leiss et al., 2002; Rosenberg and Stünitz, 2003; Brander et al., 2012; Fukuda et al., 2012; Fukuda and Okudaira, 2013; Menegon et al., 2008) and granulite facies metamorphic grade (Olsen and Kohlstedt, 1984; Kruse et al., 2001). Experimental studies were mainly carried out at high temperatures of $>700^{\circ}\text{C}$, with experimental strain rates being larger by several orders of magnitude ($10^{-5} \text{ s}^{-1} - 10^{-7} \text{ s}^{-1}$, Heidelbach et al., 2000; McLaren and Pryer, 2001; Stünitz et al., 2003) than natural strain rates ($10^{-12} \text{ s}^{-1} - 10^{-16} \text{ s}^{-1}$, e.g. Rybacki and Dresen, 2004). However, the feldspar deformation mechanisms, in particular the interaction of brittle and crystal plastic deformation and the onset of crystal plasticity in feldspars were focus of recent research and are still debated (McLaren and Pryer, 2001; Stünitz et al., 2003). Earlier studies have reported microkinks in feldspars and interpreted these as the result of brittle failure at sites of dislocation tangles (Tullis and Yund, 1987; Pryer, 1993). Crystal plastic deformation is assumed to occur above $450\text{--}550^{\circ}\text{C}$ (Fitz Gerald and Stünitz, 1993 and references therein). However, due to perfect cleavage along the (010) and (001) planes, fracturing may also play an important role at higher temperatures (Menegon et al., 2013; Tullis and Yund, 1987). Tullis and Yund (1987) argued that microstructures resembling those associated with crystal plasticity may have been caused by cataclastic flow on the sub- μm scale.

The electron backscatter diffraction (EBSD) method allows to map crystallographic orientations at high spatial resolution ($<100 \text{ nm}$ lateral resolution) and to characterize grain- and subgrain boundaries based on misorientation angles of neighbouring grains (Prior et al., 1999). This method has successfully been applied to various rock-forming minerals with different crystal symmetries, such as quartz (Stipp and Kunze, 2008), calcite (Bestmann and Prior, 2003), garnet (Prior et al., 2002), K-feldspar (McLaren and Reddy, 2008), albite (Prior and Wheeler, 1999; Jiang et al., 2000) and olivine (Demouchy et al., 2014).

Permian pegmatites in the Austroalpine Matsch Unit in South Tyrol (Italy) were overprinted by localized shear deformation at upper-greenschist facies conditions

during the Cretaceous (Schmid & Haas, 1989; Habler et al., 2009). Coarse-grained albite clasts within these mylonitic meta-pegmatites provide excellent natural examples for studying the deformation behaviour of feldspar under P–T conditions of the middle crust.

The aim of this study is to present and discuss the formation of intragranular deformation-related microstructures and textures highlighting the influence of the crystallographic anisotropies in albite clasts and their orientation with respect to the kinematic frame.

2. Methods

2.1. Electron microprobe (EPMA)

Compositional mineral analyses were performed at the Department of Lithospheric Research at the University of Vienna using a Cameca SX100 instrument at an acceleration voltage of 15 KeV, a beam current of 25 nA and a beam diameter of 6 μm for albite feldspar. Natural and synthetic standards were used for calibration. The PAP routine (Pouchou and Pichoir, 1991) was used for matrix corrections. Cations in feldspar are normalized to 8 oxygens and recalculated assuming all Fe as Fe^{3+} . Representative mineral analyses are given in Table 1.

2.2. Electron backscatter diffraction analysis (EBSD)

EBSD analyses were performed on a FEITM Quanta 3D FEG instrument at the Faculty of Geosciences, Geography and Astronomy at the University of Vienna. The system is equipped with a field-emission electron source and an EDAXTM Digiview IV EBSD camera. Polished thin sections were prepared by first mechanical and then mechano-chemical polishing using a colloidal silica suspension with a pH of 9.2–10 for the final preparation step. Electrical conductivity of the samples was established by very thin carbon coating under high vacuum conditions ($<10^{-5}$ mbar) using a single carbon thread. During EBSD analyses, the sample was tilted to 70° at a working distance of 14 mm. Beam settings were at an acceleration voltage of 15 KeV and a beam current of 4 nA in analytic mode. The OIMTM software v6.2 was used for data collection and processing. EBSD crystallographic orientation mapping was performed by beam scanning with step sizes varying from 0.5 to 2 μm . A 4x4 binning of the EBSD camera resolution was used. General parameters of the Hough settings for indexing 6–12 Hough peaks were a

Theta step sizes of 1° , a binned pattern size of 160, a minimum peak distance of 8–15 pixels in Hough space and applying a 9x9 convolution mask. The datasets were cleaned using the “Grain CI (= confidence index) Standardization” and “Neighbor Orientation Correlation” cleanup routines of the OIMTM Analysis software. EBSD data provide information on the spatial arrangement of grains, quantitative grain-size and – distribution information, the geometry of grain-boundary traces and the full crystallographic orientation. In the current study, the crystallographic orientation data are primarily presented as pole figures, whereas microstructures are shown in pattern quality maps (IQ). The latter give pattern contrast values as greyscales and were combined with data for angular misorientations between grains and subgrains. Orientation deviation maps are color coded by rainbow colors for the angular misorientation of each point with respect to a reference point within the corresponding grain. This reference point is either the average orientation of that grain or the point in this grain with the lowest kernel average misorientation.

3. Regional geology

The Matsch Unit is situated at the southern margin of the Austroalpine Ötztal–Stubai Complex (ÖSC). This Unit is lithologically dominated by biotite–sillimanite gneisses and garnet–staurolite–two mica schists with frequent intercalations of meta–pegmatites (Fig. 1; Ratschiller, 1953). Localized shear zones with largely north–dipping mylonitic foliation, ~E–W trending stretching lineations of feldspar and quartz (Figs 1b & 1c), locally varying finite–strain intensity at the cm– to m–scale (Fig. 1d) and top–W shear kinematics (Schmid and Haas, 1989) are developed at contacts of lithological subunits at the northern and southern boundary of the Matsch Unit (Habler et al., 2009). The southern tectonic boundary of the Matsch Unit is referred to as the “Vinschgau Shear Zone”, along which the metamorphic grade of deformation is supposed to increase from W to E (Schmid and Haas, 1989). The polymetamorphic evolution of the Matsch Unit comprises Variscan amphibolite facies regional metamorphism, a Permian high–temperature/low–pressure event related to the emplacement of the pegmatites (Fig. 1d), and finally upper–greenschist facies metamorphism and localized deformation at $480\pm 26^\circ\text{C}$ and 4 ± 1.6 kbar during the Cretaceous (Habler et al., 2009). Characteristic metamorphic mineral reactions for this event include the formation of chloritoid at the expense of Variscan staurolite in metapelites and the formation of a second, more Ca–rich garnet generation in both, the metapelites and meta–pegmatites (Haas, 1985; Habler

et al., 2009). The Permian age of pegmatite emplacement is constrained by garnet–whole rock Sm–Nd ages of 263–280 Ma (Habler et al., 2009). The age of intense mylonitization during the Cretaceous is independently constrained by Rb–Sr thin slab data of mylonitic meta–pegmatites yielding 83 Ma (Thöni, 1986).

Permian meta–pegmatites are frequent within the biotite–sillimanite gneisses of the Matsch Unit forming cm– to m– wide bodies, which may extend over several tens of metres along strike (Fig. 1d). Their primary magmatic mineral assemblage consists of quartz + albite + muscovite ± garnet ± K–feldspar ± apatite ± biotite ± accessories such as zircon and monazite. The metamorphic assemblage contains albite + quartz ± K–feldspar ± muscovite ± apatite ± clinozoisite/epidote. The meta–pegmatites often show increasing deformation intensities towards lithological contacts as the Cretaceous deformation is localized along rheological boundaries (Pennacchioni and Mancktelow, 2007). Strongly mylonitic meta–pegmatites have lithological contacts parallel to the foliation in their metapelitic host rocks, whereas weakly strained meta–pegmatites cross–cut the foliation in the biotite–sillimanite gneisses. Within the high–strain zones the meta–pegmatites are strongly foliated showing a compositional layering of alternating quartz–rich and feldspar–rich layers.

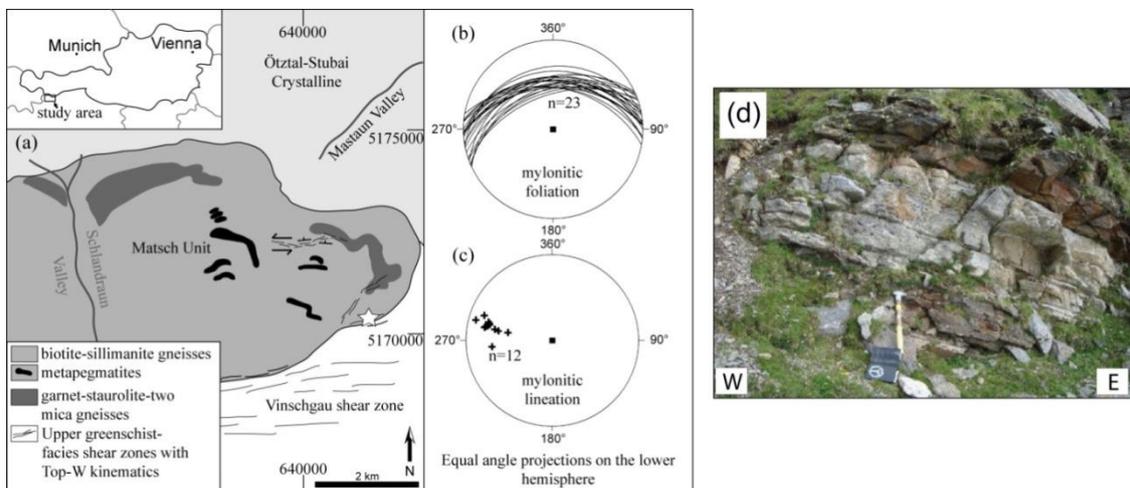


Figure 1 (a) Simplified geological sketch map of the eastern part of the Matsch Unit in the southern Ötztal–Stubai Complex (ÖSC) (modified after Habler et al., 2009) with the location of the outcrop shown in (d) (white star, Coordinates according to UTM Zone 32T, WGS84). (b) Equal angle and lower hemisphere projections of the mylonitic foliation and (c) stretching lineation as measured in the meta–pegmatite outcrop shown in (d). (Location of the outcrop: 641012m East, 5170310m North in UTM Zone 32T, WGS 84).

4. Sample description

Deformation intensity increases across single meta-pegmatite bodies towards lithological contacts. For this study, two samples were selected. The mylonitic sample HM00305 was used for EBSD analysis, while the other mylonitic sample M1201B2 was also used for mineral chemical analysis of feldspar. Both samples are briefly described below.

The EBSD sample HM00305 comes from the easternmost part of the Matsch Unit shown in Fig. 1a (North-east of white star in Fig. 1a, Location: 641362m East, 5170466m North in UTM Zone 32T, WGS84). The sample exhibits a north-dipping mylonitic foliation (003/80), a stretching lineation of quartz and feldspar at 277/23 and a top-W (sinistral) sense of shear (Figs 2a–c). Sample M1201B2 comes from the outcrop shown in Fig. 1d at a position west of sample HM00305 (Location 641012m East, 5170310m North in UTM Zone 32T, WGS84).

4.1. Lithological characterization

Both samples are mylonites with mm-sized clasts of albite, muscovite and garnet in a fine-grained matrix of the same minerals with additional quartz, apatite, biotite clinozoisite/epidote and accessory monazite and zircon.

The thin section plane of sample HM00305 in Fig. 2a is oriented parallel to the mineral stretching lineation and perpendicular to the mylonitic foliation of the hand specimen. Albite clasts are broken dominantly along crystallographic defined planes (010) and (001) into several fragments, which have been stretched and rotated forming domino and shear band boudins (Goscomb et al., 2004; Fig. 2c). They also contain numerous very fine-grained inclusions of muscovite, clinozoisite/epidote and apatite. In the strain shadows of albite clasts and the mylonitic matrix, fine-grained precipitates of albite \pm quartz \pm muscovite \pm apatite form polymineralic aggregates (Figs 2b–c). Garnet clasts are broken into numerous sub-mm sized pieces, delineating the mylonitic foliation of the sample together with alternating layers of quartz, albite and aligned fine-grained muscovite (<150 μ m, Fig. 2c). Muscovite clasts occur as mm-sized mica fish, often inclined with respect to the mylonitic foliation (Fig. 2a). Their tips are recrystallized and sheared into the foliation. Quartz forms recrystallized small grains (<150 μ m) in the mylonitic matrix.

M1201B2 also has a north-dipping mylonitic foliation (359/42) and an E–W trending stretching lineation of quartz and feldspar. Albite clasts in this sample are internally deformed and also broken along crystallographic defined planes into several fragments (Figs 2d–e). Especially in this sample, mm-sized albite clasts have a fine-grained aggregate of albite \pm quartz \pm apatite in their pressure shadows (Figs 2d–e).

The EBSD study focuses on two albite clasts from sample HM00305, shown in Figs 2b (Clast I) and 2c (Clast II). These two clasts have been selected because of the different orientations of the traces of their (010) planes with respect to the traces of the mylonitic foliation. Traces of albite twin planes are roughly perpendicular in Clast I (Fig. 2b) and parallel to the foliation in Clast II (Fig. 2c). The different orientations of the clast internal anisotropy with respect to the imposed shear flow in the matrix might have a strong influence on the deformation mechanisms operating within the clasts, which is the focus of the present study.

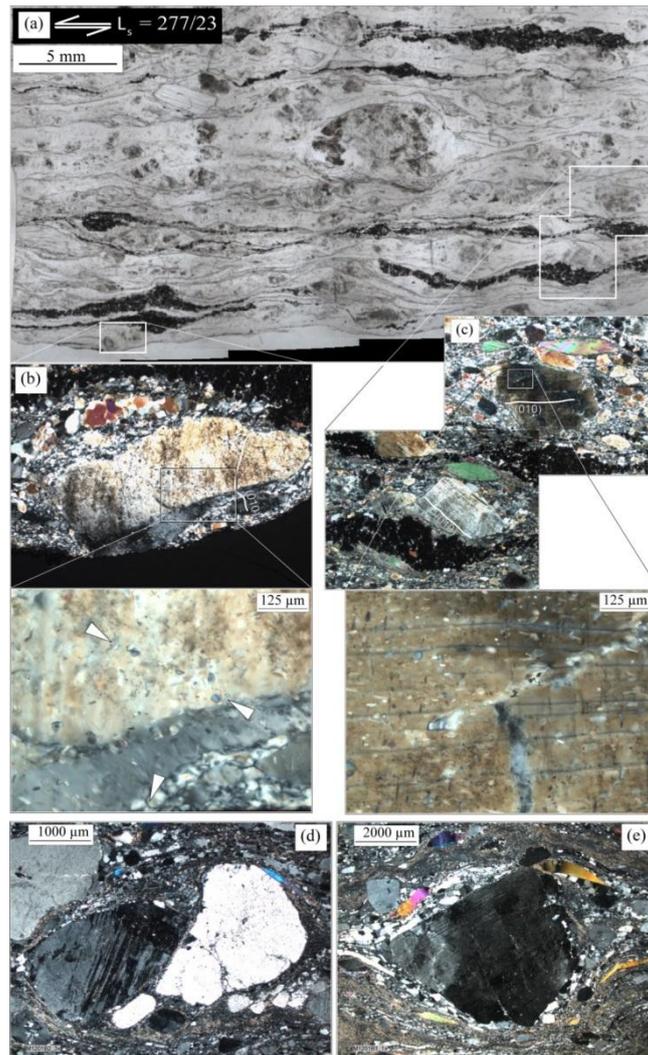


Figure 2 (previous page) (a–c) Meta–pegmatite mylonite showing a top–W (sinistral) sense of shear (Sample HM00305). (b) Clast I and (c) Clast II show albite clasts selected for EBSD analysis. Note the different orientations of the albite (010) traces with respect to the mylonitic foliation. Small boxes in (b) and (c) show high–magnification thin section images under crossed polarised light. (d–e) Albite clasts from sample M1201B2 with fine–grained albite aggregates in their pressure shadows.

4.2. Albite composition

Albite in the two mylonitic samples HM00305 and M1201B2 form two grain–size populations. Coarse grained clasts are almost pure albite with $Ab_{>95}$ (Table 1) without significant core–rim zonation in the major elements Na, Ca and K. The second group is represented by fine–grained albite in the rock matrix and in the strain shadows of the larger clasts of both samples (Figs 2d–e). These small grains (<50 μm) often have the same composition as the coarse–grained population. However, especially in the mylonite sample M1201B2, two compositionally different groups are recognized within the fine–grained albite. These are $Ab_{96–98}$ and $Ab_{89–91}$, with potassium contents of all albites analysed below 0.1 wt.% K_2O (Table 1). This is possibly caused by the peristerite miscibility gap in Na–Ca feldspars, which is well in line with the known P–T conditions of Cretaceous deformation in the upper–greenschist facies (Habler et al., 2009).

Table 1 Mineral chemical composition of albite

Phase Generation	Albite	Albite	Albite	K-feldspar	K-feldspar
	P	C	C	P	C
Sample	M1201B2	M1201B2	M1201B2	M1203	M1203
Position	clast	strain shadow	strain shadow	clast	Matrix
SiO_2	67.92	68.11	66.77	64.65	63.88
TiO_2	0.01	0.00	0.00	0.00	0.00
Al_2O_3	20.13	20.06	21.10	18.74	18.40
Cr_2O_3	0.00	0.00	0.00	0.00	0.00
Fe_2O_3	0.02	0.02	0.01	0.02	0.02
MnO	0.02	0.00	0.00	0.00	0.00
MgO	0.00	0.00	0.01	0.00	0.00
CaO	0.71	0.55	1.95	0.03	0.17
Na_2O	11.20	11.13	10.57	0.71	0.43
K_2O	0.09	0.07	0.06	15.63	15.81
BaO	0.00	0.02	0.06	0.09	0.03
Total	100.09	99.95	100.54	99.87	98.74
Oxygens	8	8	8	8	8
Si	2.97	2.98	2.92	2.99	2.99
Ti	0.00	0.00	0.00	0.00	0.00
Al	1.04	1.03	1.09	1.02	1.01
Cr	0.00	0.00	0.00	0.00	0.00
Fe-III	0.00	0.00	0.00	0.00	0.00
Mn	0.00	0.00	0.00	0.00	0.00
Mg	0.00	0.00	0.00	0.00	0.00
Ca	0.03	0.03	0.09	0.00	0.01
Na	0.95	0.94	0.89	0.06	0.04
K	0.01	0.00	0.00	0.92	0.94
Ba	0.00	0.00	0.00	0.00	0.00
Total	4.99	4.98	4.99	5.00	5.00
Xan	0.03	0.03	0.10	0.00	0.01
Xab	0.96	0.97	0.90	0.06	0.04
Xor	0.01	0.00	0.00	0.92	0.94

P = Permian, C = Cretaceous

4.3. *Microstructures and Textures*

The following description of microstructures and textures within albite clasts is based on EBSD mapping and will be subdivided into (i) Clast I with (010) at high angle to the mylonitic foliation (Fig. 2b) and (ii) Clast II with (010) sub-parallel to the mylonitic foliation (Fig. 2c). Both clasts show twinning according to the albite twin law and a number of low-angle grain boundaries with $<7^\circ$ misorientation (Figs 2–3 & 5).

Clast I

The most prominent microstructure in Clast I is a kink band, which is geometrically consistent with shear bands of that sample (Fig. 3). The blue color scale highlighting of one albite twin individual indicates a continuous crystal lattice rotation by up to 15° adjacent to the kink band (from point A to point B in the IQ map of Fig. 3a).

The continuous crystal lattice rotation towards the kink band is associated with short segments of low-angle grain boundaries with $2\text{--}7^\circ$ misorientation. These boundaries are roughly perpendicular to the traces of the (010) plane ((1) in Fig. 3a). Within the kink band in the lower right quadrant, there are numerous small grains ($<50\ \mu\text{m}$) with high-angle grain boundaries frequently forming 120° dihedral angles and lacking significant intragrain deformation (Figs 2b and 4c). A closer inspection of the kink band reveals a close relationship between the continuous crystal lattice rotation by up to 15° and the kink geometry, as indicated by the dark green and dark red highlighting of the albite clast at both sides of the kink. The data indicate that the green highlighted area has a misorientation axis with rotation angles of up to 40° , which is parallel to albite [100] (Fig. 3f). In the red highlighted part of the crystal, the situation is slightly more complex, as there is a larger scatter of misorientation axes with rotation angles of $<10^\circ$ (Fig. 3g). Furthermore, the data indicate a rotation angle of $20^\circ\text{--}50^\circ$ between the green and red highlighted areas (Fig. 3h). The corresponding direction is close to albite [100]. The rotation axis might once have been the [100] direction. However, some distortion of this rotation axis might possibly have been caused by rigid body rotation, post-dating the formation of the kink.

Besides of the kink, remarkable microstructures within Clast I are traces of serrated stylolite surfaces, running diagonally from upper left to lower right across the clast (marked by the white arrows in Fig. 2b and (2) in Fig. 3a).

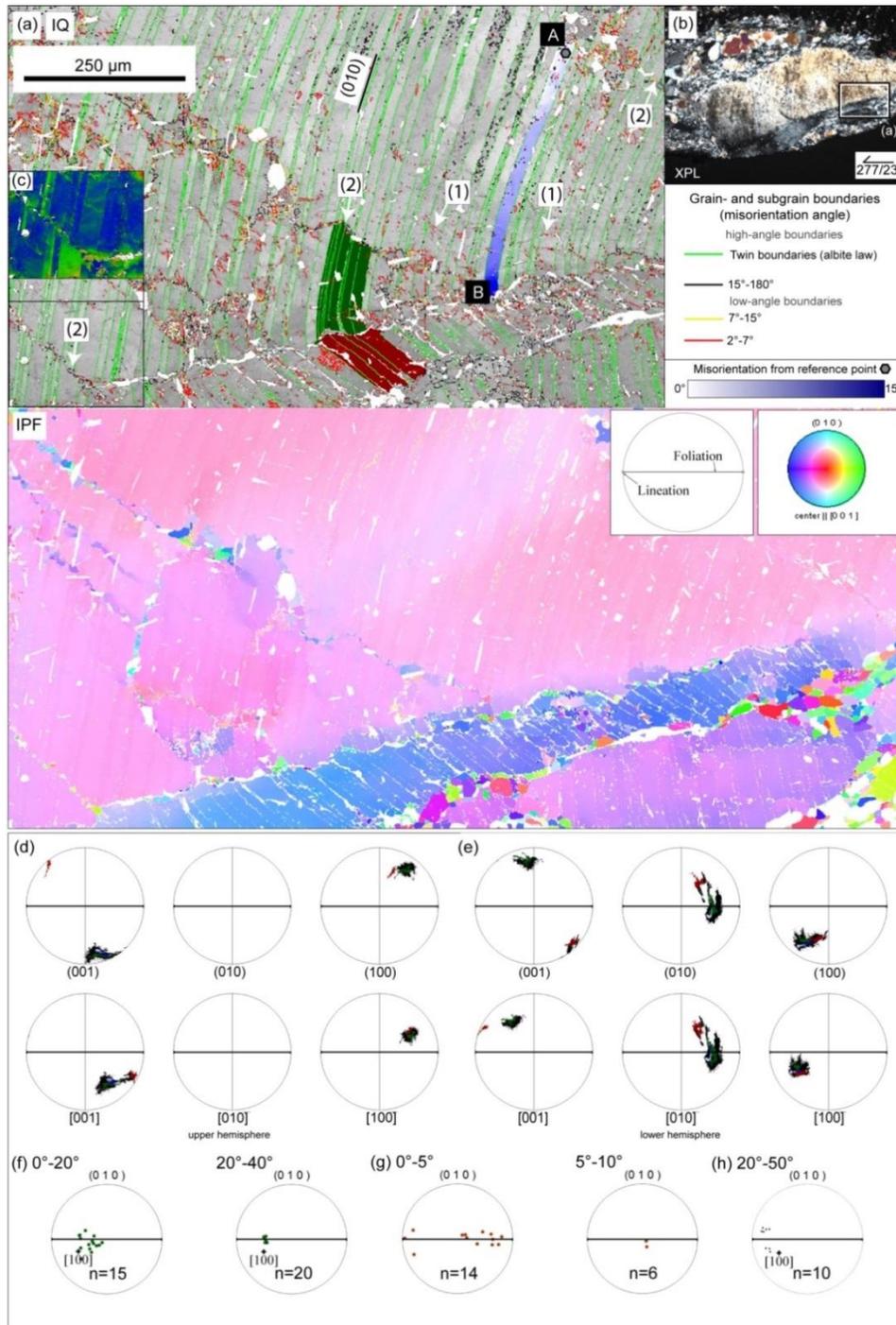


Figure 3 (a) EBSD pattern quality map (IQ) and inverse pole figure map (IPF) of Clast I. The direction normal to the sample surface is used as reference for the IPF map. The pattern quality map is highlighted for misorientations across (sub)grain boundaries and for orientation change within a single twin individual (A–B). The dark green area highlights part of the undeformed clast adjacent to the kink band, whereas the dark red area highlights part of the kink band. Numbers in round brackets point to specific features discussed in the text. (b) Corresponding thin section microphotograph in crossed polarized light. (c) Orientation deviation map with rainbow color highlighting from blue to red showing grain internal orientation variations of 0–10°. (d) Upper hemisphere equal area projection and (e) lower hemisphere equal area projection of different crystallographic orientations of the entire albite clast (>50 μm) with highlighting as in (a). (f–h) Constant misorientation angle sections for (f) the green highlighted area, (g) the red highlighted area and (h) across the kink. Both the intragranular orientation variations and the kink lamination show lattice rotation around [100]. In (h) the green and red highlighted parts of the grain are approximately rotated by about 20–50°. Maps and projections are based on the same reference frame. The orientation of the foliation and lineation is shown in (a).

In some places, very small grains of albite are present along the stylolite surfaces (Fig. 2b). A detailed view of one of the stylolite surfaces with interlocked teeth reveals an apparent off-set of the (010) plane traces. An orientation deviation (OD) map of a small area covering one of these traces (Fig. 3c) shows $<10^\circ$ grain internal misorientation adjacent to this surface, indicating the absence of significant crystal plastic or cataclastic deformation related with the stylolite formation. A fine-grained ($<50\ \mu\text{m}$) albite-fraction occurs in the kink band, as well as along the serrated stylolite surfaces (Fig. 4). Part of these grains (highlighted in grey in Fig. 4b) do not have a systematic orientation relation to the clast, whereas other grains (highlighted by a red–yellow color gradient in Fig. 4b) obviously have an orientation similar to the albite clast (cf. Figs 3 d–e and Fig. 4b). Additionally, most of the latter also show some internal deformation with $<15^\circ$ grain internal misorientation (Fig. 4c). The difference in magnitude of grain internal orientation variations is supposed to indicate, whether fine-grained albite represents fragments of the albite clast (having significant intragrain deformation), or whether they are precipitates (without intragrain deformation).

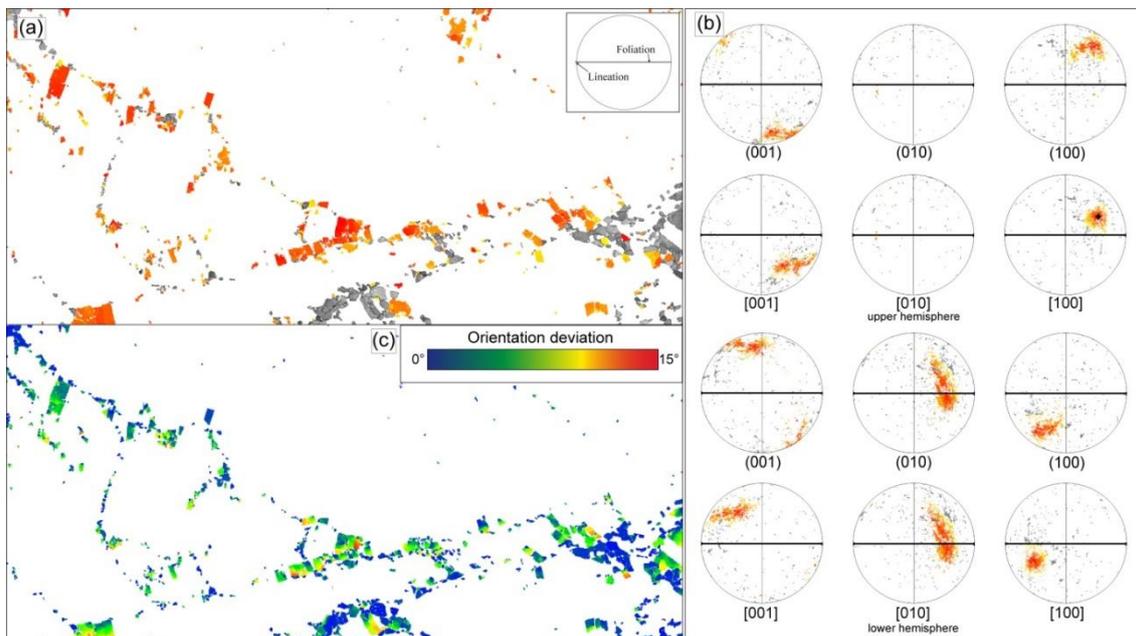


Figure 4 (a) Pattern quality map of the same area as in Fig. 3 restricted to grains $<50\ \mu\text{m}$. (b) Upper and lower hemisphere equal area projections of the crystallographic orientations of grains $<50\ \mu\text{m}$. Highlighting shows misorientation angles from 0° to 20° (red–yellow color gradient) relative to one reference point (small black cross) shown in the upper hemisphere equal area projection of [100] in (b). This reference point represents the maximum of the [100] directions of the coarse clast (cf. Fig. 3d) and has been calculated using the Harmonic Series Expansion method (Series rank (l) = 16) with an angular resolution of 3° and a Gaussian Smoothing of 12° . Thus, the threshold misorientation value for the grey data points is a minimum of 20° . Note that the clustered data points (highlighted in red–yellow color gradient) have an orientation similar to that of the clast (cf. Figs 3 d–e). (c) Orientation deviation map of the same area as in (a) with rainbow color highlighting from blue to red showing grain internal orientation variations of 0 – 15° . Maps and projections are based on the same reference frame. The orientation of the foliation and lineation is shown in (a).

Clast II

In albite clast II the (010) plane traces are parallel to the mylonitic foliation (Figs 2c and 5). Clast II contains a microshear zone, which (in bulk sample coordinates) has a similar orientation as the kink band in clast I, being kinematically compatible with synthetic slip on a shear band (Fig. 2c). This microshear zone is related to a crack (Fig. 2c). Several fine-grained albite grains within the microshear zone obviously have no crystallographic orientation relation to the hosting clast, as their misorientation with respect to the hosting clast exceeds 15° (Fig. 5a).

The EBSD IQ map (Fig. 5a) reveals the presence of low-angle boundaries with $2\text{--}7^\circ$ misorientation in roughly two different orientations, located mainly above the microshear zone. One set of traces is roughly perpendicular to the microshear zone and has maximum misorientations of approximately 4° (Fig. 5c, Line A–B). The change in orientation is rather continuous towards the low-angle boundary and reaches maximum point to point misorientation of less than 0.5° (Fig. 5c), which is in the range of the angular resolution of these EBSD data. Right at the boundary there is a sharp step of $\sim 3^\circ$ misorientation between neighboring points (Fig. 5c, Line A–B).

The other set of low-angle boundaries has traces parallel to the (001) plane traces (Fig. 5a). They commonly occur in pairs with lengths of $<20\ \mu\text{m}$, a spacing of $<5\ \mu\text{m}$ and an angular misorientation of $<7^\circ$ (Fig. 5). A misorientation profile across one of these is presented in Fig. 5c (Line C–D). The point to point misorientation is also very low ($\sim 0.5^\circ$) with two points of $\sim 7^\circ$ misorientation at 4 and 6 μm from Point C (Fig. 5c). In this paper the term ‘microkink’ is used for these microstructural features. Similar microstructures were observed by Pryer (1993) in coarse-grained (cm-sized) K-feldspar clasts from a major thrust zone in the Greenville Front in Ontario, Canada in the optical microscope. However, the microkinks in our samples are too small to be discovered under the optical microscope.

It is important to note, that the low-angle grain boundaries are scarce in the area below the microshear zone (Fig 5a). Instead, this area comprises a crack tracing parallel to feldspar (001) and perpendicular to (010), filled with K-feldspar (Kfs, see Fig. 5a).

The implications of the microstructural and textural observations from the two different clasts with their crystallographic anisotropies at different angles relative to the mylonitic foliation are discussed in the following section.

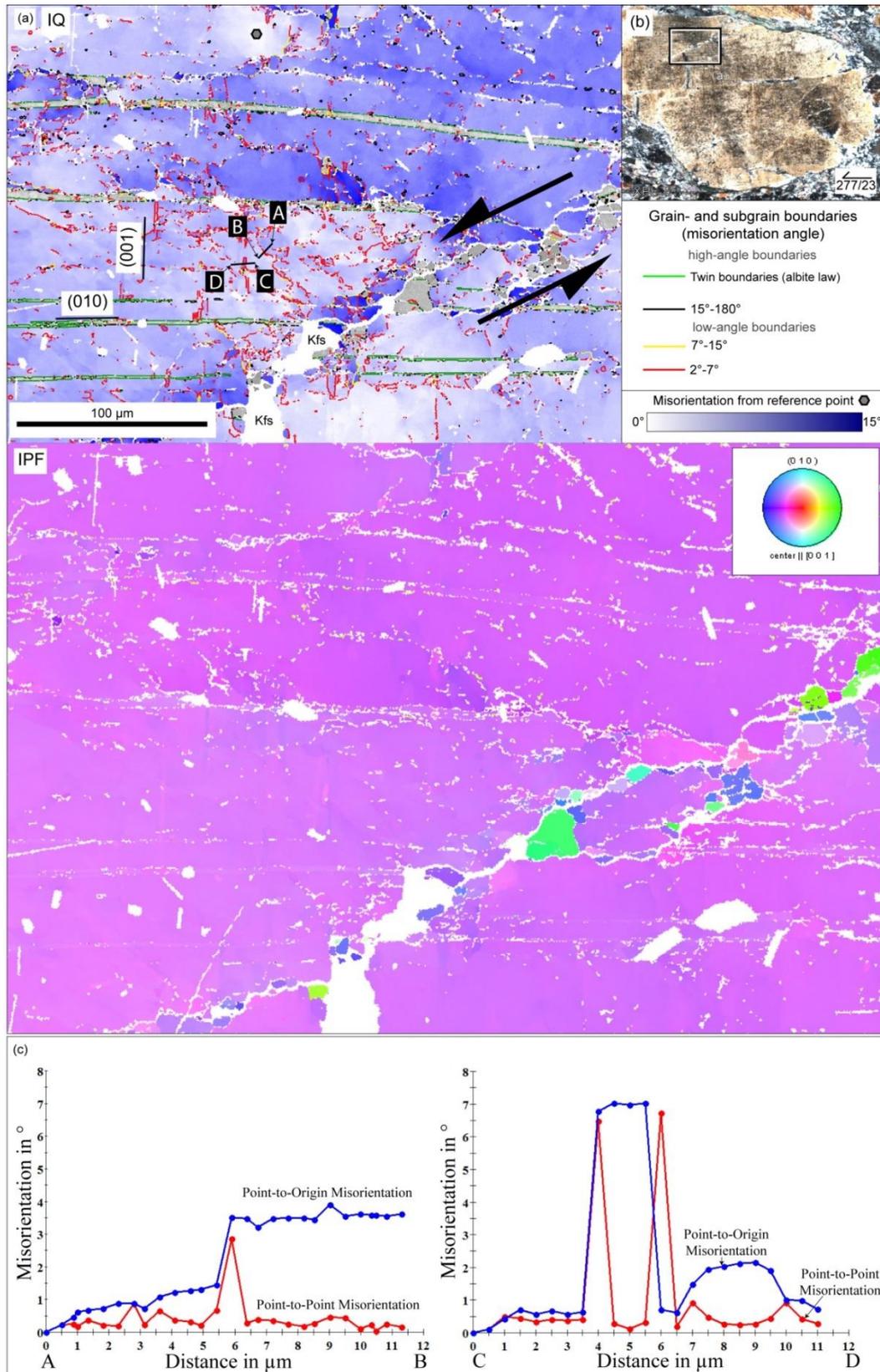


Figure 5 (a) EBSD pattern quality map (IQ, step size: 0.5 μm) and inverse pole figure map (IPF) of Clast II. The direction normal to the sample surface is used as reference for the IPF map. The pattern quality map is shown with (sub)grain boundaries colored according to misorientation across the boundary and blue highlighting giving the misorientation with respect to a reference point (upper central position). Black arrows indicate displacement on the microshear zone. Lines A–B and C–D give the position of misorientation profiles presented in Fig. 5c. (b) Thin section photomicrograph (crossed polarized light) with the studied area within the white box. (c) Misorientation profiles of lines A–B and C–D (position given in Fig 5a).

5. Discussion

Previous EBSD studies on albite focused on the fundamental development of this technique for the collection of crystallographic orientation data (Prior and Wheeler, 1999, Jiang et al., 2000). In this study, we applied the EBSD method for the simultaneously combined crystallographic orientation mapping and microstructural analysis of albite from upper–greenschist facies mylonitic metapegmatites in the Austroalpine Unit of the central Eastern Alps.

Under these crustal P–T conditions, feldspar typically shows a transitional behaviour between brittle and crystal plastic behaviour. According to Fitz Gerald and Stünitz (1993), this transition occurs at about 450–550°C. Since slip systems are crystallographically controlled, minerals with low symmetries may have only a small number of easily activated slip systems, such as (010)[001] in feldspar (Olsen and Kohlstedt, 1984), compared to phases with higher symmetries. Therefore, crystal plastic deformation by dislocation glide in feldspars is expected to be strongly direction dependent (e.g. Vernon, 2004). In addition to pressure, temperature, fluid availability, stress and strain–rate, the orientation of σ_1 with respect to the major slip system will have a significant control on the activation of specific deformation mechanisms (Stünitz et al., 2003). However, cataclastic and plastic deformation mechanisms are often related within the semi–brittle field (McLaren and Pryer, 2001). Tullis and Yund (1987) have shown with TEM analyses that deformation microstructures on the optical scale suggesting crystal plasticity, are actually caused by cataclastic flow on the sub– μm scale. This highlights the importance of the scale of observations on which the interpretations of active deformation mechanisms are based (e.g. Vernon, 2004). The microstructures of Clast I and II studied in this work suggests that the orientation of anisotropies within the clasts have a strong influence on the active deformation mechanisms and therefore on microstructure formation processes.

5.1. Dissolution–precipitation of albite

Dissolution–precipitation or ‘stress–induced solution transfer’ (Vernon, 2004) occurs by dissolution of crystalline material at sites of high compressive stresses (e.g. grain or phase boundaries), diffusion of the dissolved matter in an aqueous solution along grain and phase boundaries and subsequently precipitation of the material in low stress sites, such as cracks (Wintsch and Yi, 2002; Imon et al., 2002; Passchier and Trouw, 2005).

The serrated stylolite surfaces running diagonally from upper left to lower right across Clast I (white arrows in Fig. 2b and (2) in Fig. 3a) are located at a high angle of approximately 90° relative to the supposed shortening direction and roughly perpendicular to the (010) plane traces (i.e. parallel to (001), Fig. 6a), hence they are in suitable orientations for the dissolution of albite. Furthermore, these surfaces are obviously not related to significant intracrystalline crystal plastic deformation (Fig. 3c; Passchier and Trouw, 2005). Numerous small albite grains ($<50 \mu\text{m}$) with straight grain boundary segments and no significant internal deformation are present in the vicinity of the kink (Figs 2b, 3a and 4c). As the crystallographic orientation data of these grains prove, they do not have an orientation relation to the entire clast (Figs 3a and 4b). Thus, we interpret these microstructures as related to dissolution of albite along the stylolitic surfaces and subsequent precipitation of the dissolved material in a location near its origin, probably a low stress site. Such a site would be equivalent to the pressure shadows of large albite clasts and cracks within them, in which we also found fine-grained aggregates of albite related to stress-induced solution transfer. A similar scenario seems likely for the grains within the microshear zone in Clast II (Fig. 5). The grains within this zone, potentially representing clast fragments, do not have a crystallographic orientation relation to the clast (Fig. 5). This is assumed to be due to a free rotation of these grain fragments during or after the formation of the crack preceding the microshear zone. After that they potentially have acted as nuclei for the further precipitation of albite related to dissolution-precipitation, thus explaining the lack of a strong orientation relation to the clast.

Especially this last point is typically taken as a characteristic feature of dissolution-precipitation (e.g. Knipe, 1989). However, this should be seen with care as experimental studies (Heidelbach et al., 2000) and numerical models (Bons and den Brok, 2000) have shown, that stress-induced solution transfer can be related to the formation of a crystallographic preferred orientation. This might be due to anisotropic rates of dissolution and growth of the related material or to epitaxial overgrowth on pre-existing grains. Nevertheless, this is unlikely in our samples, as most of the grains related to dissolution-precipitation have only a very weak or even no orientation relation to the respective clasts or associated grain fragments.

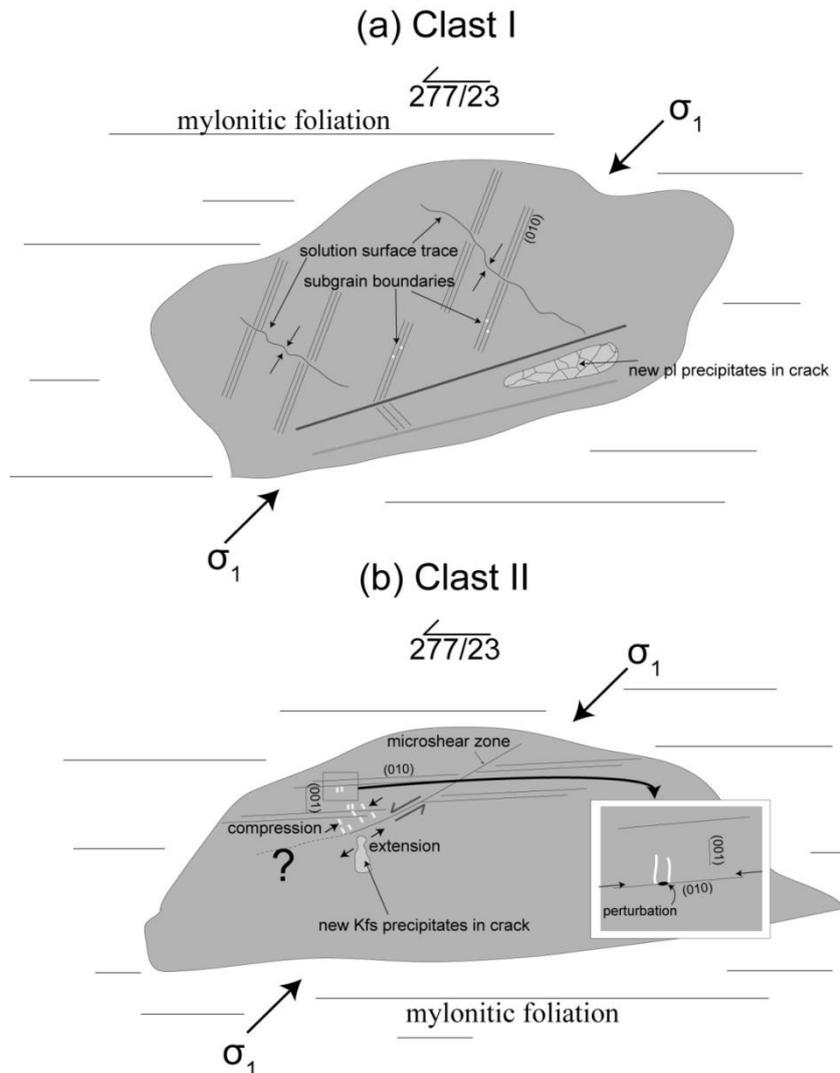


Figure 6 Simplified sketches highlighting the relation between a common kinematic frame (the orientation of the σ_1 -axis) and the microstructures in (a) Clast I with (010) at high angle and (b) Clast II with (010) sub-parallel to the mylonitic foliation in sample HM00305.

5.2. Cataclastic vs crystal-plastic deformation

Albite in our samples clearly preserves evidence for cataclastic deformation, especially along the crystallographic defined planes (010) and (001) (Figs 2c–d, 5b). We interpret the ‘microkinks’, occurring in pairs parallel to the traces of the (001) feldspar plane, to be due to microkinking on a μm -scale, probably associated with small perturbing inclusions (Fig. 6b). The rather abrupt change in orientation across such a microkink instead of a more continuous orientation change is also consistent with this interpretation (Fig. 5c). The microshear zone presented in Clast II (Fig. 5a) is interpreted to have originated as a mode I/II crack on which the microshear zone subsequently nucleated, because it is almost parallel to and therefore in a suitable

orientation for fracturing with respect to the supposed shortening direction (Fig. 6). The off-set of the traces of the (010) planes at the microshear zone indicates a sinistral/synthetic sense of shear (Fig. 5, black arrows). As it is very likely, that the microshear zone terminates in the vicinity of the studied area towards the lower left in Fig. 2c, this necessitates compression above and extension below the microshear zone. This is perfectly consistent with our microstructural observations of low-angle boundaries with a continuous crystallographic orientation change perpendicular to and above and a Kfs-filled crack below the microshear zone (Fig. 5a). This example clearly shows the mutual interrelation and contemporaneity of cataclastic and crystal plastic deformation within a single clast.

However, despite the fact that microstructures resembling ductile deformation may in fact be due to cataclastic flow on the sub- μm scale (e.g. Tullis and Yund, 1987), we show, based on our observation scale, that the other microstructures associated with the continuous crystal lattice rotation by up to 15° and the kink are due to crystal plastic deformation (Fig. 3).

The short segments of the low-angle boundaries perpendicular to the traces of the (010) plane and the continuous crystal lattice rotation with the [100] rotation axis (Fig. 3) are related. This is due to dislocation glide as it is unlikely to achieve such a homogeneous strain with regularly spaced microcracks on the sub- μm scale. Otherwise it cannot be excluded, based on our observation scale, that the low-angle boundaries are actually sub- μm cracks due to high stresses at sites of tangled dislocations. This is only possible to see with the transmission electron microscope.

For the common slip system in feldspar (010)[001] (Stünitz et al., 2003, Olsen and Kohlstedt, 1984), in the case of edge dislocations, the misorientation axis m [100] lies in the glide plane (010) and is parallel to the dislocation line g . In this case, the burgers vector $b=[001]$ is at an angle of 116° to the misorientation axis (Fig. 7a). In the case of screw dislocations, the misorientation axis m would be perpendicular to the glide plane (010) and the burgers vector b would be parallel to the dislocation line $g=[001]$ (Fig. 7b). As we identified the feldspar [100] direction as the rotation axis for the continuous crystal lattice rotation, our observations are consistent with an edge character of dislocations related with the activity of the glide system (010)[001]. This is supposed to have caused the formation of subgrain boundaries and associated continuous crystal lattice rotation.

As the kink band lamination also appears rotated by an axis close to albite $[100]$ with respect to the undeformed clast (Figs 3e and 3h), this indicates a close relation to dislocation glide on $(010)[001]$ (Fig. 7) associated with the continuous crystal lattice rotation of up to 15° . Due to potentially limited dislocation mobility at the given T-conditions of about 500°C (Habler et al., 2009), dislocations might have tangled, finally leading to strain hardening and consequently to fracturing. This, in turn, might have enabled rigid body rotation and consequently the formation of a brittle kink band and the slight distortion of a $[100]$ -parallel rotation axis (Figs 3e and 3h).

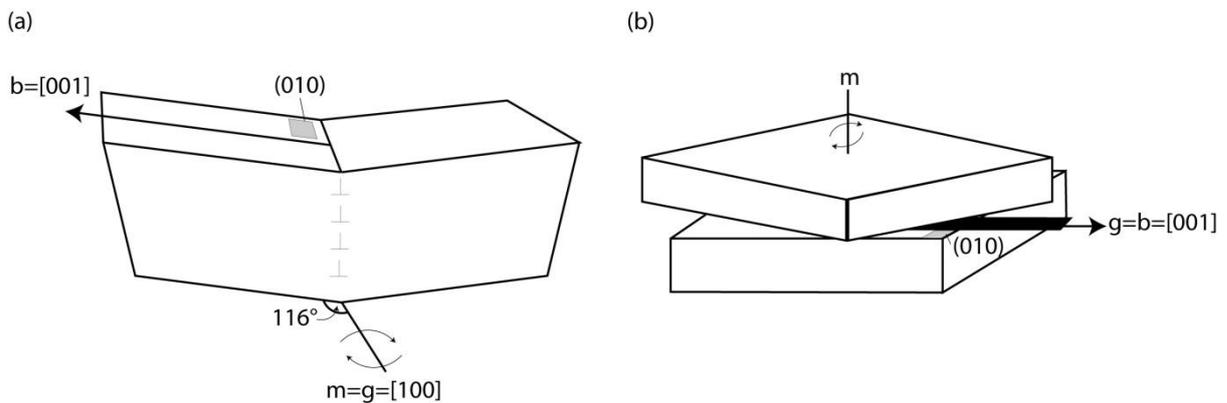


Figure 7 Schematic sketches illustrating (a) edge and (b) screw dislocations of the slip system $(010)[001]$ in plagioclase feldspar (modified from Kruse et al., 2001).

5.3. Timing of microstructure formation

Unravelling the relative formation timing of the various microstructures is very important for the potential discrimination of pre-Alpine deformation from the major event during the Cretaceous. In Clast I (Fig. 2b), we found a direct relation between continuous crystal lattice rotation by dislocation glide and a kink together with strong evidence for dissolution-precipitation-related precipitation of albite predominantly within the kink band (Figs 3 and 4). Therefore, the different deformation mechanisms operated simultaneously within the same clast. Within Clast II crystal plastic and brittle deformation in the host clast are kinematically controlled by shear deformation within the studied microshear zone, which in turn is related to the top-W kinematics of the Cretaceous deformation (Schmid & Haas, 1989). Therefore, all observed deformation-related microstructures discussed in this study, may have formed during a single tectonometamorphic event within a single top-W kinematic frame at temperature conditions of about 500°C , previously reported for the Cretaceous event (Habler et al.,

2009; Schmid and Haas, 1989). Evidence for pre-Alpine, especially Permian high-temperature deformation, was not found.

6. Conclusions

A range of different deformation microstructures within albite clasts of Permian meta-pegmatites from the Austroalpine basement in the Matsch Unit in the Eastern Alps were identified and characterized by microstructural investigations as well as crystallographic orientation mapping using electron backscatter diffraction. The following conclusions can be drawn highlighting the interplay of various contemporaneously formed microstructures and the role of crystallographic anisotropies in microstructure formation in albite at upper-greenschist facies conditions (Fig. 6):

1. Fluid-assisted dissolution-precipitation of albite represents the predominant mechanism accommodating the deformation of feldspars at upper-greenschist facies conditions, but is intimately related with the grain-internal formation of (micro)kinks, cracks, low-angle boundaries, stylolites and the activity of microshear zones
2. Dissolution-precipitation led to precipitation of fine-grained albite grains and aggregates in the matrix and in extensional quadrants of clasts (Fig. 2d-e) as well as in dilatational/low-stress sites along cracks and kink planes within the clast (Figs 3-5). Fine-grained feldspar aggregates in our samples, formed by dissolution-precipitation, lack a crystallographic preferred orientation and consist mainly of grains without significant intragrain deformation (Figs 2b and 4)
3. Crystal plastic intragranular lattice rotation in albite has a misorientation axis parallel to albite [100] and kink formation is associated with a misorientation axis close to albite [100] (Figs 3 f-h) indicating a crystallographic control on the microstructure formation. However, some distortion of this common rotation axis potentially indicates rigid body rotation post-dating the crystal plastic lattice rotation and the kink formation
4. Crystal plastic deformation of albite supposedly has been accommodated by dislocation glide on the common (010)[001] slip system in case of a favorable lattice orientation with respect to the external stress field

5. Microkink formation parallel to the traces of (001) is likely associated with small perturbing inclusions and minor intracrystalline slip on the (010) plane (Fig. 6b)
6. The orientation of crystallographic anisotropy in albite exerts a strong control on the development of specific deformation-related microstructures as indicated by the different deformation behaviour of clasts with different angular relations between their (010) and the mylonitic foliation (Figs 2 and 6). Similar dependencies have been observed elsewhere in muscovite (Mares and Kronenberg, 1993) and in plagioclase (Stünitz et al., 2003)

Acknowledgements

Funding was provided by the University of Vienna (Doctoral School IK052) and the Austrian Science Fund (FWF): I471–N19 as part of the International Research Group FOR 741 D–A–CH. The authors acknowledge access to the Electron Microprobe Laboratory and the Laboratory for scanning electron microscopy and focused ion beam applications of the Faculty of Geosciences, Geography and Astronomy at the University of Vienna (Austria). T. Griffiths, C. Trepmann and A.–K. Schäffer are thanked for discussions and S. Hrabe and C. Beybel for sample preparation. We are grateful to T. Okudaira and H. Stünitz for very constructive reviews and T. Takeshita for comments and editorial handling of the manuscript.

References

- Bestmann, M., Prior, D.J., 2003. Intragranular dynamic recrystallization in naturally deformed calcite marble: diffusion accommodated grain boundary sliding as a result of subgrain rotation recrystallization. *Journal of Structural Geology* 25, 1597–1613.
- Bons, P.D., den Brok, D., 2000. Crystallographic preferred orientation development by dissolution–precipitation creep. *Journal of Structural Geology* 22, 1713–1722.
- Brander, L., Svahnberg, H., Piazzolo, S., 2012. Brittle–plastic deformation in initially dry rocks at fluid–present conditions: transient behaviour of feldspar at mid–crustal levels. *Contributions Mineralogy Petrology* 163, 403–425.

- Bürgmann, R., Dresen, G., 2008. Rheology of the Lower Crust and Upper Mantle: Evidence from Rock Mechanics, Geodesy, and Field Observations. *Annual Review of Earth and Planetary Sciences* 36, 531–567.
- Demouchy, S., Mussi, A., Barou, F., Tommasi, A., Cordier, P., 2014. Viscoplasticity of polycrystalline olivine experimentally deformed at high pressure and 900°C. *Tectonophysics* 623, 123–135.
- Fitz Gerald, J.D., Stünitz, H., 1993. Deformation of granitoids at low metamorphic grade. I: Reactions and grain size reduction. *Tectonophysics* 221, 269–297.
- Fukuda, J., Okudaira, T., Satsukawa, T., Michibayashi, K., 2012. Solution–precipitation of K–feldspar in deformed granitoids and its relation with water distribution. *Tectonophysics* 532–535, 175–185.
- Fukuda, J., Okudaira, T., 2013. Grain–size–sensitive creep of plagioclase by solution–precipitation and mass transfer under mid–crustal conditions. *Journal of Structural Geology* 51, 61–73.
- Goscombe, B.D., Passchier, C.W., Hand, M., 2004. Boudinage classification: end–member boudin types and modified boudin structures. *Journal of Structural Geology* 26, 739–763.
- Haas, R., 1985. Zur Metamorphose des südlichen Ötztalkristallins unter besonderer Berücksichtigung der Matscher Einheit (Vinschgau/Südtirol). PhD thesis, University of Innsbruck, 118 pages.
- Habler, G., Thöni, M., Grasemann, B., 2009. Cretaceous metamorphism in the Austroalpine Matsch Unit (Eastern Alps): The interrelation between deformation and chemical equilibration processes. *Mineralogy and Petrology* 97, 149–171.
- Heidelbach, F., Post, A., Tullis, J., 2000. Crystallographic preferred orientation in albite samples deformed experimentally by dislocation and solution precipitation creep. *Journal of Structural Geology* 22, 1649–1661.
- Imon, R., Okudaira, T., Fujimoto, A., 2002. Dissolution and precipitation processes in deformed amphibolites: an example from the ductile shear zone of the Ryoke metamorphic belt, SW Japan. *Journal of metamorphic Geology* 20, 297–308.

- Jiang, Z., Prior, D.J., Wheeler, J., 2000. Albite crystallographic preferred orientation and grain misorientation distribution in a low-grade mylonite: implications for granular flow. *Journal of Structural Geology* 22, 1663–1674.
- Knipe, R.J., 1989. Deformation mechanisms—recognition from natural tectonites. *Journal of Structural Geology* 11, 127–146.
- Kruse, R., Stünitz, H., Kunze, K., 2001. Dynamic recrystallization processes in plagioclase porphyroclasts. *Journal of Structural Geology* 23, 1781–1802.
- Leiss, B., Gröger, H.R., Ullemeyer, K., Lebit, H., 2002. Textures and microstructures of naturally deformed amphibolites from the northern Cascades, NW USA: methodology and regional aspects. In: *Deformation Mechanisms, Rheology and Tectonics: Current Status and Future Perspectives* (eds De Meer, S., Drury, M.R., De Bresser, J.H.P., Pennock, G.M.), Geological Society, London, Special Publications 200, 219–238.
- Mares, V.M., Kronenberg, A.K., 1993. Experimental deformation of muscovite. *Journal of Structural Geology* 15, 1061–1075.
- McLaren, A.C., Pryer, L.L., 2001. Microstructural investigation of the interaction and interdependence of cataclastic and plastic mechanisms in Feldspar crystals deformed in the semi-brittle field. *Tectonophysics* 335, 1–15.
- McLaren, S., Reddy, S.M., 2008. Automated mapping of K-feldspar by electron backscatter diffraction and application to $^{40}\text{Ar}/^{39}\text{Ar}$ dating. *Journal of Structural Geology* 30, 1229–1241.
- Mehl, L., Hirth, G., 2008. Plagioclase preferred orientation in layered mylonites: Evaluation of flow laws for the lower crust. *Journal of Geophysical Research* 113, 1–19.
- Menegon, L., Pennacchioni, G., Stünitz, H., 2006. Nucleation and growth of myrmekite during ductile shear deformation in metagranites. *Journal of metamorphic Geology* 24, 553–568.
- Menegon, L., Pennacchioni, G., Spiess, R., 2008. Dissolution–precipitation creep of K-feldspar in mid-crustal granite mylonites. *Journal of Structural Geology* 30, 565–579.

- Menegon, L., Stünitz, H., Nasipuri, P., Heilbronner, R., Svahnberg, H., 2013. Transition from fracturing to viscous flow in granulite facies perthitic feldspar (Lofoten, Norway). *Journal of Structural Geology* 48, 95–112.
- Olsen, T.S., Kohlstedt, D.L., 1984. Analysis of Dislocations in Some Naturally Deformed Plagioclase Feldspars. *Physics and Chemistry of Minerals* 11, 153–160.
- Passchier, C.W., Trouw, R.A.J., 2005. *Microtectonics*. Springer–Verlag, Berlin Heidelberg, New York, 366p.
- Pennacchioni, G., Mancktelow, N.S., 2007. Nucleation and initial growth of a shear zone network within compositionally and structurally heterogeneous granitoids under amphibolite facies conditions. *Journal of Structural Geology* 29, 1757–1780.
- Pouchou, J.L., Pichoir, F., 1991. Quantitative analysis of homogeneous or stratified microvolumes applying the model “PAP”. In: *Electron Probe Quantitation*, (eds Heinrich, K.F.J., Newbury, D.E.), 31–75.
- Prior, D.J., Wheeler, J., 1999. Feldspar fabrics in a greenschist facies albite–rich mylonite from electron backscatter diffraction. *Tectonophysics* 303, 29–49.
- Prior, D.J., Boyle, A.P., Brenker, F., Cheadle, M.C., Day, A., Lopez, G., Peruzzo, L., Potts, G.J., Reddy, S., Spiess, R., Timms, N.E., Trimby, P., Wheeler, J., Zetterström, L., 1999. The application of electron backscatter diffraction and orientation contrast imaging in the SEM to textural problems in rocks. *American Mineralogist* 84, 1741–1759.
- Prior D.J., Wheeler, J., Peruzzo, L., Spiess, R., Storey, C., 2002. Some garnet microstructures: an illustration of the potential of orientation maps and misorientation analysis in microstructural studies. *Journal of Structural Geology* 24, 999–1011.
- Pryer, L.L., 1993. Microstructures in feldspars from a major crustal thrust zone: the Grenville Front, Ontario, Canada. *Journal of Structural Geology* 15, 21–36.
- Ratschiller, L.K., 1953. Beiträge zur regionalen Petrographie des Vintschgau–Gebietes (Südtirol). *Neues Jahrbuch Mineralogische Abhandlungen* 85, 247–302.

- Rosenberg, C.L., Stünitz, H., 2003. Deformation and recrystallization of plagioclase along a temperature gradient: an example from the Bergell tonalite. *Journal of Structural Geology* 25, 389–408.
- Rybacki, E., Dresen, G., 2004. Deformation mechanism maps for feldspar rocks. *Tectonophysics* 382, 173–187.
- Schmid, S.M., Haas, R., 1989. Transition from near–surface thrusting to intrabasement decollement, Schlinig thrust, Eastern Alps. *Tectonics* 8, 697–718.
- Simpson, C., Wintsch, R.P., 1989. Evidence for deformation–induced K–feldspar replacement by myrmekite. *Journal of metamorphic Geology* 7, 261–275.
- Stipp, M., Kunze, K., 2008. Dynamic recrystallization near the brittle–plastic transition in naturally and experimentally deformed quartz aggregates. *Tectonophysics* 448, 77–97.
- Stünitz, H., Fitz Gerald, J.D., Tullis, J., 2003. Dislocation generation, slip systems, and dynamic recrystallization in experimentally deformed plagioclase single crystals. *Tectonophysics* 372, 215–233.
- Thöni, M., 1986. The Rb–Sr thin slab isochron method – an unreliable geochronological method for dating geologic events in polymetamorphic terrains? Evidence from the Austroalpine basement nappe, the Eastern Alps. *Memorie di Scienze Geologiche* 38, 283–352.
- Tsurumi, J., Hosonuma, H., Kanagawa, K., 2003. Strain localization due to a positive feedback of deformation and myrmekite–forming reaction in granite and aplite mylonites along the Hatagawa Shear Zone of NE Japan. *Journal of Structural Geology* 25, 557–574.
- Tullis, J., Yund, R.A., 1987. Transition from cataclastic flow to dislocation creep of feldspar: Mechanisms and microstructures. *Geology* 15, 606–609.
- Vernon, R.H., 1975. Deformation and Recrystallization of a Plagioclase Grain. *American Mineralogist* 60, 884–888.
- Vernon, R.H., 2004. *A practical guide to Rock Microstructure*. Cambridge University Press, Cambridge, 94 p.

Papers and manuscripts

Wintsch, R.P., Yi, K., 2002. Dissolution and replacement creep: a significant deformation mechanism in mid-crustal rocks. *Journal of Structural Geology* 24, 1179–1193.

Papers and manuscripts

2.2 Paper #2

Rb/Sr isotopic and compositional retentivity of muscovite during deformation

Eberlei, T., Habler, G., Wegner, W., Schuster, R., Körner, W., Thöni, M., Abart, R.

(2014)

Lithos

Under Review

Rb/Sr isotopic and compositional retentivity of muscovite during deformation

Eberlei, T.^{a,*}, Habler, G.^a, Wegner, W.^a, Schuster, R.^b, Körner, W.^c,

Thöni, M.^a, Abart, R.^a

^aDepartment of Lithospheric Research, University of Vienna, Althanstraße 14, A–1090 Vienna, Austria (* corresponding author: Tobias Eberlei; E–mail: tobias.eberlei@univie.ac.at; phone: +43 1 4277 53362)

^bAustrian Geological Survey, Neulinggasse 38, A–1030 Vienna, Austria

^cDepartment of Environmental Geosciences, University of Vienna, Althanstraße 14, A–1090 Vienna, Austria

E–mail addresses and phone numbers:

gerlinde.habler@univie.ac.at; +43 1 4277 53475 (Gerlinde Habler)

wencke.wegner@univie.ac.at; +43 1 4277 53104 (Wencke Wegner)

Ralf.Schuster@geologie.ac.at; +43 1 712 56 74 210 (Ralf Schuster)

wilfried.koerner@univie.ac.at; +43 1 4277 53120 (Wilfried Körner)

martin.thoeni@univie.ac.at; (Martin Thöni)

rainer.abart@univie.ac.at; + 43 1 4277 53319 (Rainer Abart)

Abstract

Permian metapegmatite muscovite from the Upper–Austroalpine Matsch Unit in Southern Tyrol (Italy) was investigated regarding its Rb/Sr isotopic and compositional retentivity during Cretaceous deformation. The data imply, that microstructurally relic Permian magmatic muscovite largely maintained its major and trace element composition during deformation, whereas the Rb–Sr geochronometer is strongly

affected by, presumably deformation-related, Sr-loss. Three possible scenarios of Sr-loss at different times are discussed in this paper. These are consistent with our data and can explain variations in Rb-Sr muscovite-whole rock ages among different grain-size and magnetic fractions of muscovite that had crystallised during Permian pegmatite emplacement. The proposed scenarios can explain the presence of Permo-Triassic muscovite formation/cooling ages of muscovite grain size- and magnetic fractions with relatively low $^{87}\text{Rb}/^{86}\text{Sr}$ and $^{87}\text{Sr}/^{86}\text{Sr}$ ratios. Presuming that the isotopic composition is not changed during any late-stage fluid-related alteration, the present-day muscovite-internal age should approximate the timing of the Sr-loss event. The results imply that brittle and crystal plastic deformation play an important role in controlling the Rb-Sr geochronometer of muscovite porphyroclasts and their compositional retentivity during upper-greenschist facies Cretaceous mylonitisation.

1. Introduction

As one of the most common minerals in the Earth's crust, muscovite is stable in various igneous and metamorphic rock types and a wide range of P-T conditions. The Rb-Sr geochronometer in muscovite has commonly been used to infer cooling, neo-crystallisation and recrystallisation ages, often in conjunction with the associated whole rock or other coexisting phases (e.g. Armstrong et al., 1966; Jäger et al., 1967; Thöni, 1981; George and Bartlett, 1996; Freeman et al., 1997; Glodny et al., 1998; Müller et al., 1999; Kühn et al., 2000; Müller et al., 2000; Glodny et al., 2002; Glodny et al., 2003; Glodny et al., 2008; Bröcker et al., 2013). The original concept of the 'blocking' or 'closure' temperature (Jäger et al., 1967; Dodson, 1973) implies that temperature is the rate-limiting factor for isotope mobility and that isotopes leaving the crystal by temperature-dependent volume diffusion are exchanged with an infinite reservoir. Other important factors are the effective diffusion domain size (i.e. grain size), dynamic recrystallisation, the cooling rate, the diffusion coefficients for elements and isotopes in the mineral under investigation, the modal composition of a rock, the presence or absence of grain boundary fluids which could influence rates of material exchange with an infinite reservoir, chemical exchange among different minerals during cooling and the mineral composition (Ganguly and Ruiz, 1987; Yund and Tullis, 1991; Jenkin et al., 1995; Jenkin, 1997; Villa, 1998; Jenkin et al., 2001; Glodny et al., 2003). For example, Kühn et al. (2000) found Grenvillian biotite Rb-Sr ages in rocks which had experienced Caledonian eclogite facies metamorphism at temperatures exceeding 650°C, which they

attributed to the absence of a free fluid phase during metamorphism. The Rb–Sr isotopic system of cm–sized, undeformed muscovite from granitic metapegmatites in the western Bohemian massif remained closed at temperatures exceeding 600°C (Glodny et al., 1998). Commonly reported closure temperatures for the Rb–Sr geochronometer in white micas are in the range of 500°C–550°C (e.g. Purdy and Jäger, 1967; Blanckenburg et al., 1989; Freeman et al., 1997). Glodny et al. (1998) also identified plastic deformation at these temperatures in shear zones as cause for resetting the Rb–Sr isotopic system of muscovites. In ^{40}Ar – ^{39}Ar geochronology, it is well known, that dislocations, subgrain boundaries, kinks and stacking faults can act as fast–diffusion pathways and therefore influence the Ar–retentivity of crystals at temperatures below the closure temperature of Ar (e.g. Reddy et al., 1996; Hames and Cheney, 1997; Baldwin and Lister, 1998; Dunlap and Kronenberg, 2001; Mulch et al., 2002; Kramar et al., 2003; Cosca et al., 2011). It is also known, that changes in the mica polytype during metamorphism can influence the Ar–retentivity (Beltrando et al., 2013).

Permian metapegmatites in the Austroalpine Matsch Unit (Ötztal–Stubai Basement Complex, OSC) in Southern Tyrol (Italy) were overprinted by localised shear deformation at upper–greenschist facies conditions of *c.* 500°C and 5 kbar during the Cretaceous Eo–Alpine tectonometamorphic event (Schmid and Haas, 1989; Habler et al., 2009). Therefore, the Permian metapegmatites provide excellent natural examples to study the Rb/Sr isotopic and compositional retentivity of coarse–grained microstructurally relic muscovite clasts and the mechanisms affecting their Rb–Sr system during deformation. For this purpose, we used several different bulk mineral separates from single samples. Different muscovite grain–size and magnetic fractions were used for the combined analysis of Rb and Sr by ID–TIMS and the major and trace elements by EPMA, ICP–OES and ICP–MS. The new data provide insights into the behaviour of the Rb–Sr system and major and trace elements in Permian muscovite porphyroclasts during Cretaceous deformation.

2. Geological Setting

Samples of Permian metapegmatites were collected in the Matsch Unit in Southern Tyrol (Italy). A list of studied samples with UTM coordinates (UTM Zone 32T, WGS84) is given in Table 1. The Matsch Unit is located at the southern margin of the Upper–Austroalpine Ötztal–Stubai Crystalline complex (OSC, Fig. 1a). The km–wide ‘Vinschgau Shear Zone’ (Schmid and Haas, 1989) defines its southern tectonic

boundary. Eo–Alpine T–conditions are supposed to gradually increase from W to E in shear direction of the Vinschgau Shear Zone. The predominant lithologies in the Matsch Unit are biotite–sillimanite gneisses and garnet–staurolite–two mica schists with frequently intercalated Permian metapegmatites (Figs 1b–c, Ratschiller, 1953). Cretaceous deformation is localised in shear zones and characterised by north–dipping foliations, E–W trending fold axes and stretching lineations of quartz and feldspar, locally varying gradients of finite–strain at the cm– to m–scale and top–W shear kinematics (Schmid and Haas, 1989). The polymetamorphic evolution of the Matsch Unit is characterised by Carboniferous amphibolite facies regional metamorphism, a Permian HT/LP event related with pegmatite formation (Fig. 1c) and finally upper–greenschist facies tectonometamorphism culminating in P–T conditions of $480\pm 26^{\circ}\text{C}$ at 4 ± 1.6 kbar (Habler et al., 2009). The timing of pegmatite emplacement was constrained to 263–280 Ma by Sm–Nd garnet–whole rock data (Habler et al., 2009). Eo–Alpine deformation was dated at 83 ± 1 Ma based on Rb–Sr thin slab data of mylonitic meta–pegmatites (Thöni, 1986). Eo–Alpine metamorphism in the OSC formed a sequence of NE–SW trending mineral zones which document increasing Cretaceous metamorphism from NW to SE by: (i) a zone without Cretaceous metamorphic mineral content, (ii) a Stilpnomelane zone, (iii) a Chloritoid zone (Purtscheller, 1967) and (iv) the Eo–Alpine Staurolite zone (Thöni, 1981, 1983). These zones correlate with characteristic K–Ar and Rb–Sr biotite ages (Thöni, 1981). Zone (i) correlates with Carboniferous biotite cooling ages (Fig. 1a). The stilpnomelane and chloritoid zones are characterised by opening and incomplete resetting of the K–Ar isotopic system in biotite, or excess ^{40}Ar in biotite (Fig. 1a, Thöni, 1981) whereas the zone of Eo–Alpine staurolite correlates with Late Cretaceous biotite cooling ages. Regarding the regional distribution of Cretaceous minerals, the studied rocks of the Matsch Unit are part of the chloritoid zone, wherefrom biotite K–Ar isotopic data showed disturbance but no complete Cretaceous isotopic resetting (Thöni, 1981, 1983).

Table 1 Sampling locations (UTM Zone 32T, WGS 84) of the studied samples. Sampling locations are given with an accuracy of ± 10 m.

Sample	Rock type	North [m]	East [m]	Altitude [m]
M1210	meta-pegmatite	5170589	640300	2830
M1217	meta-pegmatite	5170206	640396	2680
HM00305	protomylonitic Meta-pegmatite	5170494	641263	2596
M1203	protomylonitic Meta-pegmatite	5170319	640984	2624
M1201	mylonitic meta-pegmatite	5170319	640984	2624
M1206	ultramylonitic meta-pegmatite	5170310	640963	2620

The metapegmatites are commonly intercalated in biotite–sillimanite gneisses, rarely in Grt–St micaschist (Figs 1b–c). The primary magmatic mineral assemblage of the pegmatites consists of quartz + albite + muscovite ± garnet ± K–feldspar ± apatite ± accessory zircon and monazite. The metamorphic mineral assemblage contains albite + quartz + muscovite ± K–feldspar ± apatite ± biotite ± garnet ± clinozoisite/allanite. Despite of intense deformation, muscovite and feldspar clasts of the primary magmatic mineral assemblage were preserved as microstructural relics.

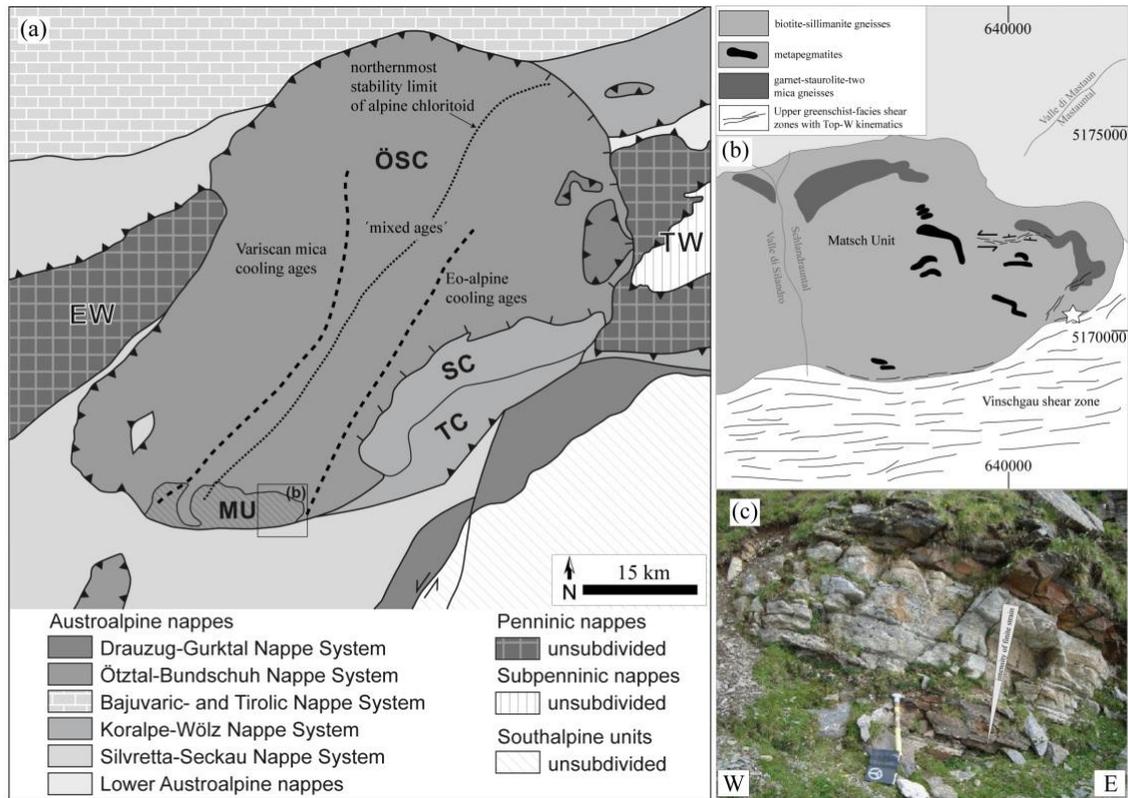


Figure 1 (a) Simplified geological sketch map of the Upper–Austroalpine Ötztal–Stubai Crystalline complex based on Schmid et al. (2004) and Thöni (1981). Abbreviations: EW = Engadine window; TW = Tauern window; OSC = Ötztal–Stubai Complex; SC = Schneeberg Complex; TC = Texel Complex; MU = Matsch Unit. (b) Simplified sketch map of the eastern portion of the Matsch Unit (based on Habler et al., 2009). (c) Representative metapegmatite outcrop within the biotite–sillimanite gneisses (see white star for location in (b)) Coordinates are UTM Zone 32T, WGS 84.

3. Analytical Methods

3.1. Electron microprobe (EPMA)

Compositional mineral analyses were performed at the Department of Lithospheric Research at the University of Vienna using a Cameca SX100 instrument with an acceleration voltage of 15 keV, a beam current of 20 nA and a beam diameter of 3 μm for white mica and apatite and 6 μm for feldspar. Natural and synthetic standards were used for calibration. The PAP routine (Pouchou and Pichoir, 1991) was used for matrix

corrections. Mineral formulae of white mica are normalised to 11 oxygen and assuming all Fe as Fe²⁺. Element distribution maps were obtained by continuous stage movement with dwell times of 40 ms and a step size of 1 µm. Representative muscovite analyses are given in Table B1 in the appendix.

3.2. Rb/Sr isotope dilution analysis (ID–TIMS)

Selected rock samples were crushed in a jaw crusher and a rolling mill, and sieved. Whole rock splits were taken after crushing the kg-sized samples. White mica concentrates were obtained by using a vibrating table, repeated grinding in ethanol and sieving, magnetic purification on a Frantz isodynamic magnetic separator and washing in acetone. Subsequently impurities were removed by handpicking under an optical microscope, increasing the optical purity to >99 %. Different well-defined primary grain size- and magnetic fractions were produced (see Table 2).

For isotope dilution analysis, 100–200 mg of each muscovite concentrate were weighed into Savillex® screw top beakers, mixed with a ⁸⁷Rb–⁸⁴Sr spike and dissolved in a 4:1 HF/HNO₃ mixture on a hot plate for 2 weeks at 110°C. Rb and Sr were extracted applying standard cation exchange techniques. Sr isotope ratios were measured on a FINNIGAN® Triton multicollector thermal ionisation mass spectrometer. Within-run mass-dependent Sr isotope fraction was corrected for with ⁸⁶Sr/⁸⁸Sr=0.1194. The ⁸⁷Rb/⁸⁵Rb ratio was measured on a FINNIGAN® MAT262 mass spectrometer. Both instruments are part of the Laboratory of Geochronology at the University of Vienna. During the 9-month measuring period, the ⁸⁷Sr/⁸⁶Sr value of the NBS standard SRM 987 was 0.710269 ± 4 (2σ, n = 17). Total procedural blanks of Rb and Sr were consistently below 0.03 ng. By default, a 1 % relative error is assigned to the ⁸⁷Rb/⁸⁶Sr ratio. All other errors are quoted on the 2σ level (95% confidence). Age calculations are based on a ⁸⁷Rb decay constant of 1.42*10⁻¹¹ a⁻¹ (Steiger and Jäger, 1977). A second aliquot of each muscovite concentrate was used for the production of a mineral separate embedded in epoxy resin. Polished thin sections prepared from the embedded separates were used for major element compositional analysis with the electron microprobe.

3.3. Major and trace element analysis by ICP–OES/MS

A third aliquot of separated muscovite fractions and the whole rocks were used for major and trace element analysis by ICP–OES and ICP–MS. Selected elements (K, Na, Ca, P, Be, Li, Cs, REE) were measured on a Agilent 7700 Series inductively coupled

mass spectrometer (ICP–MS) and a PerkinElmer Optima 5300 DV inductively coupled optical emission spectrometer instrument (ICP–OES) at the Department of Environmental Sciences at the University of Vienna. REE were exclusively analysed by ICP–MS. Standards were run at the end of each measuring cycle. The reproducibility of the standards is generally better than 20% (see Tables A1 and A2 in the appendix). Detection limits for the trace elements are: 0.1 ppm (Be, Li, REE) and 0.05 ppm (Cs).

4. Results

4.1. Sample description

For the isotopic and compositional analyses, 6 samples have been selected (Table 1). Four of them stem from a single proto– to ultramylonitic meta–pegmatite layer (Fig. 1c) of about 1.5 m thickness and extending laterally over >50 meters. The remaining two were sampled from two different pegmatite bodies about 25 meters (sample M1217) and 450 meters (sample M1210) structurally above the former outcrop, estimated approximately normal to the mylonitic foliation. Deformation intensity increases across the sampled metapegmatite body towards the footwall and is expressed by a pronounced grain–size reduction especially of albite, K–feldspar, muscovite and –if present– garnet (Figs 1c–d and 2). Sample M1210 stems from the centre of a massive, largely undeformed metapegmatite body and M1217 was collected near the core of a massive, weakly foliated metapegmatite. Whereas samples M1210 and M1217 stem from positions at some distance from a Cretaceous shear zone, the remaining samples HM00305, M1203, M1201 and M1206 stem from a Cretaceous high strain zone localised within meta–pegmatite at the lithological boundary between Bt–Sill gneiss and orthogneiss.

Muscovite

Permian magmatic relic muscovite generally occurs as cm– to mm–sized clasts, with decreasing grain–size from the undeformed metapegmatite M1210 (>1 cm) to the ultramylonite M1206 (<500 μm ; Figs 2a–f). Several samples show prominent kinks with kink band widths of several hundred μm ((1) in Figs 2a,c,e). Additionally, muscovite clasts in several samples contain numerous microkinks with lengths of <20–30 μm and slight lattice bendings as displayed by undulous extinction in polarised light microscope images ((2) in Figs 2a,c,d). According to Bell et al. (1986), kinks are generally associated with dislocations and cleavage cracks parallel to muscovite (001).

The strong lattice deformation along the kink axial planes is associated with a fine-grained ($<50\ \mu\text{m}$) muscovite generation ((3) in Figs 2a,b). Additionally in the deformed samples, fine-grained muscovite is also present in the quartzo-feldspathic rock matrix, defining a weak to strong mylonitic foliation by its shape preferred orientation (Figs 2c-f). However, in none of the samples a correlation between clast grain-size and presence/absence of large kinks or microkinks was observed. Coarse-grained clasts in a few samples (M1210 and M1217) contain numerous, μm -sized, acicular inclusions of Fe-oxides and -sulphides with a clear shape preferred orientation parallel to muscovite (001) ((4) in Figs 2a,b) and small ($<20\ \mu\text{m}$), euhedral apatite crystals. In none of the samples, a spatial correlation between presence/absence of such inclusions and kinks of any size were found. Several clasts show evidence for grain-scale cracking at high angles to muscovite (001) ((5) in Figs 2b,c).

Quartz

Quartz microstructures indicate recovery by subgrain rotation and grain boundary migration recrystallisation, with decreasing grain-size of the recrystallised quartz grains from the largely undeformed metapegmatite M1210 to the ultramylonite. The quartz grain-size decreases from a few hundred μm in M1210 to $<40\ \mu\text{m}$ in M1206 (Fig. 2). Assuming constant temperatures during the Cretaceous tectonometamorphic event, this is explained by substantially higher strain-rates in the ultramylonitic sample M1206, compared to M1210 (Stipp et al., 2002). Additionally, the mylonitic foliation, as expressed by the shape preferred orientation of the small muscovite generation, is also preserved in a weak shape preferred orientation of quartz.

Feldspar

Albite and K-feldspar have survived the intense Cretaceous mylonitisation as clasts that range in size from $>1\ \text{cm}$ in M1210 to $<500\ \mu\text{m}$ in M1206 (Fig. 2). Furthermore, both feldspars preserve evidence for extensive dissolution-precipitation, producing grain-sizes of $<50\ \mu\text{m}$, that tend to decrease from M1210 to M1206. Together with alternating layers of quartz, muscovite and fractured garnet ($<100\ \mu\text{m}$), these delineate a mylonitic foliation in the high-strain samples (e.g. Figs 2c-f).



Figure 2 Representative microstructures of (a) M1210, (b) M1217, (c) HM00305, (d) M1203, (e) M1201 and (f) M1206. Note the intense grain-size reduction of clasts and in the matrix with increasing deformation intensity from (a) to (f). Numbers in round brackets highlight specific microstructures discussed in the text.

4.2. *Muscovite generations and mineral assemblages*

Based on backscatter electron images and element mapping 3 distinct groups of white mica have been identified in all samples (Fig. 3). Core-domains of coarse-grained Permian magmatic muscovite clasts have unaltered primary major element composition (Wm I). These have compositionally altered rims (Wm II) which are separated from Wm I by clearly defined compositional fronts. Wm II is microstructurally not distinguishable from Wm I, but may also form alteration zones within the interior of

coarse-grained clasts. Wm II occurs immediately adjacent to (001) cleavage planes (Fig. 3b) and along fractures (Fig. 3c–h). The microstructurally characteristic fine-grained (<50 μm) third muscovite group (Wm III) constitutes the mylonitic rock matrix, forms overgrowths on Wm I (Figs 3a–b) and newly crystallised along kink axial planes. Wm II and Wm III are supposed to have formed during the Cretaceous tectonometamorphic event.

Qualitative EDX analysis in SEM in combination with BSE imaging showed that μm -sized inclusions of allanite, biotite and apatite are often related with the compositionally altered rims Wm II of the Permian muscovite clasts Wm I (Figs 3a,b). Furthermore, the syntectonic phase assemblage muscovite (Wm III), fine-grained K-feldspar, biotite, apatite, albite and quartz adjacent to the muscovite clasts has been identified in the mylonitic rock matrix and in strain shadows of Wm I clasts (Figs 3a,b).

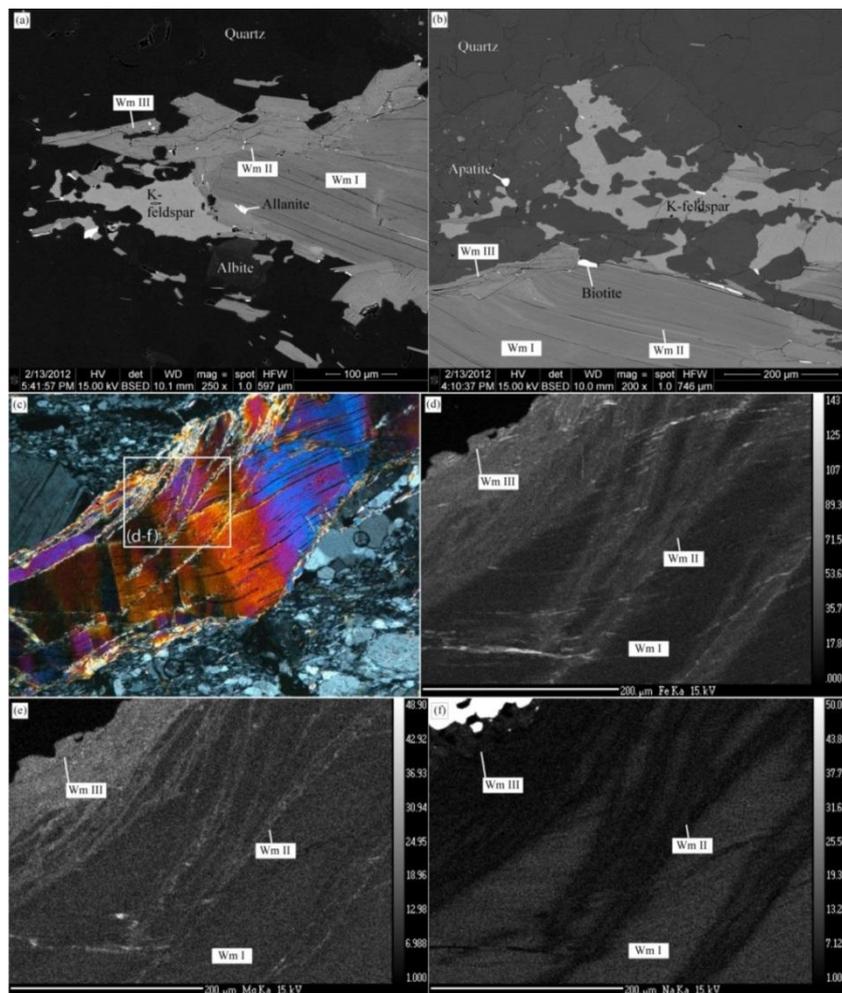


Figure 3 (a–b) BSE images of sample HM00305 showing the different muscovite groups (Wm I–III), their inclusions and the related syntectonic phase assemblage including Wm III. (c) Photomicrograph with crossed polarised light showing a kinked and fractured Ms-clast of sample M1203. (d–f) Quantitative element maps showing (d) Fe-, (e) Mg- and (f) Na-distribution in the area highlighted in Fig 3(c).

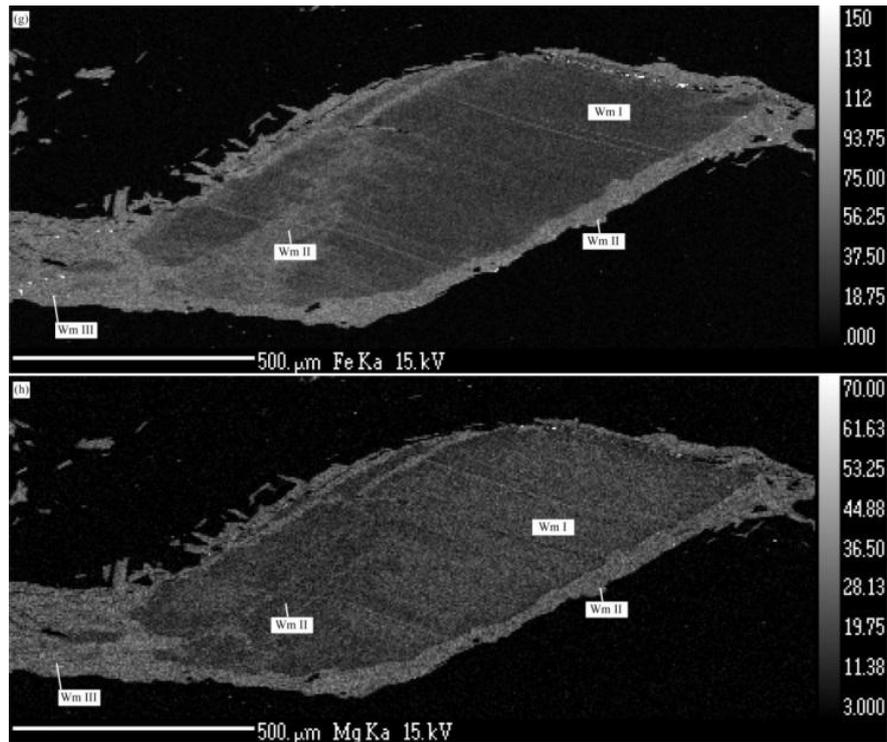


Figure 3 (g–h) Quantitative element maps of a mm-sized Permian muscovite clast from sample M1217 showing (g) Fe- and (h) Mg-distribution related to the different muscovite groups. Note, the weak compositional difference between Wm II associated with the clast-internal domain (crack) and the Wm II along the rims.

4.3. Mineral composition

4.3.1. Muscovite

Representative compositions of muscovite groups Wm I, Wm II and Wm III derived from EMPA are given in Table B1 in the appendix.

4.3.1.1. Wm I – Permian magmatic muscovite

The cm-sized Permian magmatic muscovite grains are compositionally close to the pure muscovite endmember with <3.1 Si c.p.f.u. (cations per formula unit), >2.7 Al c.p.f.u., and commonly less than 0.2 Fe²⁺ c.p.f.u. and <0.04 Mg²⁺ c.p.f.u. (Fig. 4, Table B1).

4.3.1.2. Wm II – Compositionally overprinted rims of Wm I

Wm II portions of coarse grained clasts are commonly richer in Fe with Fe²⁺ c.p.f.u. in the range 0.15 – 0.3 . Si typically ranges from 3.1 to 3.2 Si c.p.f.u. with some exceptions of Si c.p.f.u. >3.2 (Fig. 4, Table B1). Wm II and Wm III are compositionally identical (Fig. 4). However, small compositional fluctuations within Wm II may also exist. An example for this is displayed by one mm-sized muscovite clast in sample M1217. Here,

a grain-scale crack in that clast is associated with Wm II that is slightly poorer in Fe and Mg, compared to Wm II on the clasts rim (Figs 3g–h). Wm II shows sharp compositional fronts towards Wm I, while the thickness varies at 10 – 30 micrometers (Fig. 3). Similar sharp compositional fronts but with different compositional characteristics have been observed elsewhere in hydrothermally altered granites (e.g. Dempster et al., 1994; Gomes and Neiva, 2000). Dempster et al. (1994) found such secondary rims on primary magmatic muscovites from the Oughterard granite in western Ireland. They correlated increasing Si-contents (up to 3.4 c.p.f.u.) of these secondary muscovites with increasing degree of hydrothermal alteration. Gomes and Neiva (2000) presented a detailed compositional analysis of such rims from zoned muscovite in the Ervedosa granite in northern Portugal. According to their data, the overgrowth is richer in Fe+Mg and Rb but has less Al and Na, than the relic magmatic muscovite.

4.3.1.3. *Wm III – Matrix muscovite*

Matrix muscovite is often compositionally indistinguishable from Wm II (Figs 3–4, Table B1). In all medium- and low-strained samples, Wm II and Wm III have significantly higher Al-celadonite contents (elevated Fe and Si content) than Wm I allowing for a clear distinction between primary magmatic muscovite (Wm I) and muscovite-fractions formed during the metamorphic overprint (Wm II, Wm III). Contrastingly, the highly strained samples M1201 and M1206 display a wider scatter of the Wm II and Wm III compositions, causing an overlapping compositional range of the microstructurally different muscovite generations. (Fig. 4).

4.3.2. *Embedded muscovite separates*

Muscovite separates from samples M1210, M1217, M1203 and M1201 were embedded in epoxy resin and analysed by EMPA in order to detect a potential contribution of the metamorphic muscovite fractions (Fig. 5). The EMPA data from embedded separates showed that all different muscovite grain size and magnetic fractions consist exclusively of Wm I (Fig. 5). The embedded material is characterised by relatively low Si (<3.1 Si c.p.f.u.) and low Fe (< 0.15 Fe²⁺ c.p.f.u.). Only in the high-strain sample M1201, there is a compositional overlap with Wm II and Wm III as indicated by the grey areas that are shown to highlight the compositional range of these 2 groups which have been derived from grains during thin section analyses (Fig. 5). Contributions from other

phases and sub-microscopic mineral inclusions were not observed in the embedded muscovite separates, although a potential contribution of sub- μm sized feldspar, apatite or zoisite/allanite inclusions can never be explicitly excluded.

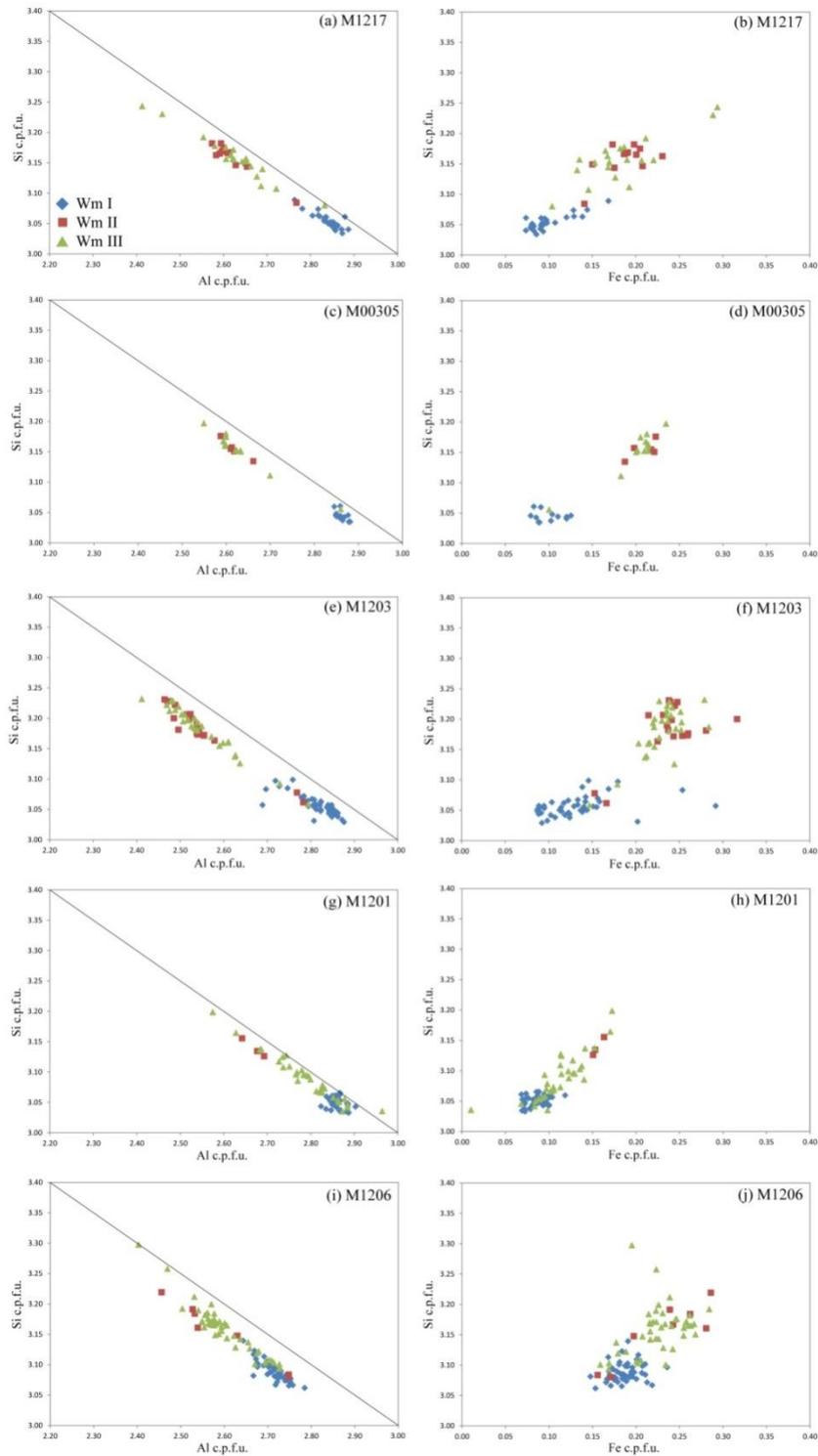


Figure 4 Muscovite compositional data by EMPA of Wm I (blue diamonds), Wm II (red squares), Wm III (green triangles) of (a–b) M1217, (c–d) M00305, (e–f) M1203, (g–h) M1201 and (i–j) M1206. Note the compositional overlap of different generations in the high-strain samples M1201 and M1206. For legend, see Fig. 4a.

The mean FeO concentrations of up to 50 single spot analysis of individual grains for each fraction are given in Table 2. The data show a correlation of FeO concentration with magnetic susceptibility, thus demonstrating the role of Fe in controlling the magnetic properties of the analysed material. Furthermore, TE-B3 seems to be slightly poorer in Al and Si and richer in Fe²⁺ compared to TE-B4 (Figs 5c–d). This might be due to an undetected larger Fe³⁺/Fe²⁺ ratio.

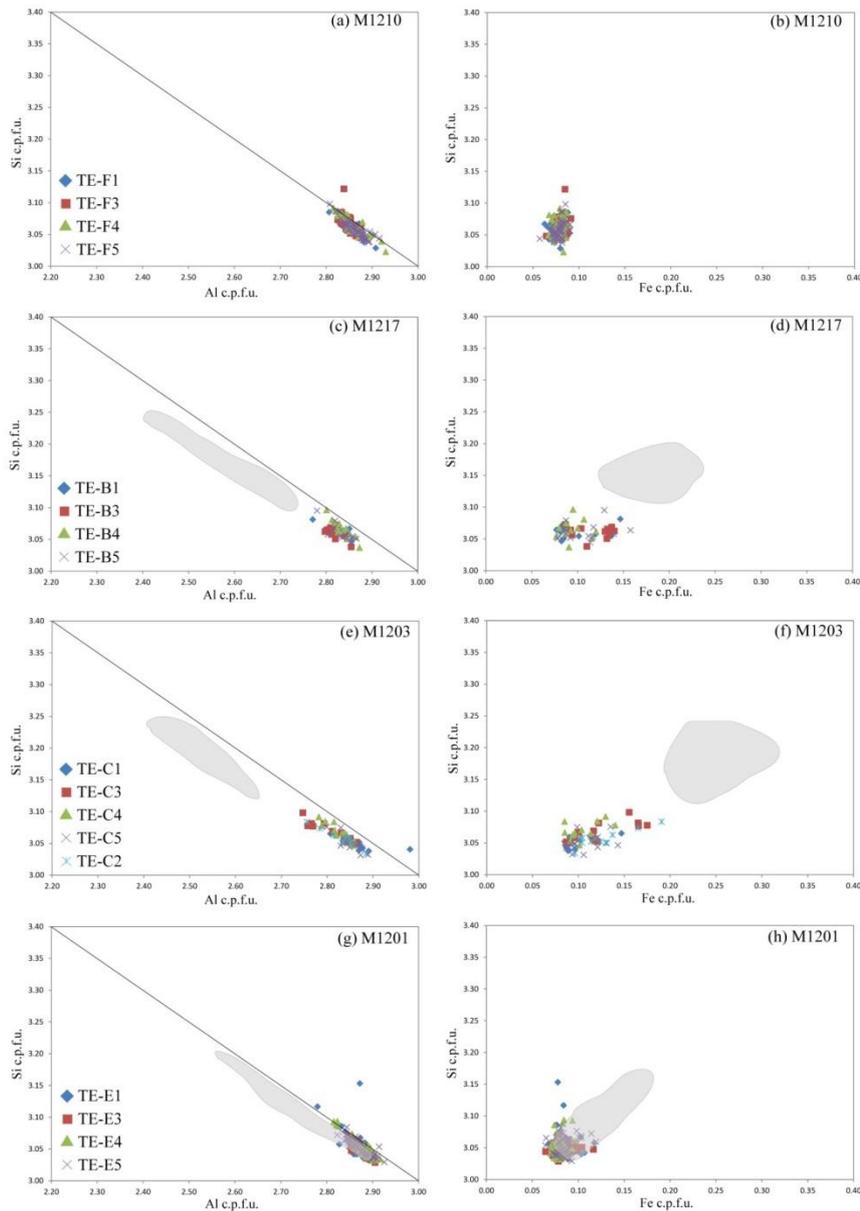


Figure 5 EMPA compositional data of embedded muscovite separates of Wm I used for Rb/Sr ID-TIMS analysis of (a–b) M1210, (c–d) M1217, (e–f) M1203 and (g–h) M1201. Grey areas limit the compositional range of Wm II and Wm III determined by EMPA from thin sections of rock chips. Note the overlap of this field with data from Wm I separates in M1201 (g–h) (cf. Fig. 4). See text for discussion.

4.3.3. *Apatite and feldspar*

Sample HM00305 contains fine-grained (<20 μm) euhedral apatite crystals, spatially related to the syntectonic phase assemblage (Figs 3a–b). Some of these supposedly Cretaceous apatite crystals are rich in fluorine (1.1–3.3 wt.% F), poorer in chlorine (<0.4 wt.% Cl) and contain small concentrations of Sr (~0.01 wt.% SrO). Albite grains, formed by dissolution–precipitation, in this sample also contain some Sr (~0.02–0.05 wt.% SrO). However, in both phases, no correlation between microstructural position and chemical composition was observed.

4.4. *Isotope, major and trace element data (ICP–MS and ID–TIMS)*

4.4.1. *Permian metapegmatite bulk compositions*

Permian metapegmatites are Si-rich rocks (>73 wt.% SiO_2) with moderate Al-concentrations (12.5–15 wt.% Al_2O_3). Their K/Rb ratios are 130–250, while Rb/Cs ratios range at 15–80. At Li-concentrations of 16–30 ppm their REE-contents are generally below 1–2 ppm. In M1203, M1201 and M1206, the concentrations of La, Ce and Nd are slightly elevated (up to 11.5 ppm, Table C1 in the appendix). Their chondrite-normalised REE-pattern show no significant fractionation ($\text{Ce}_n/\text{Yb}_n < 5$) except of the weakest deformed sample M1210 (TE–F0) in which $\text{Ce}_n/\text{Yb}_n = 32$ (Fig. 6a). The ultramylonite sample M1206 has REE-concentrations about one order of magnitude larger than the other samples. Apart from that, no relation between intensity of deformation and REE-contents in the bulk samples was observed. Some samples exhibit a weak negative Eu-anomaly (HM00305, M1210, M1206), while the other samples do not show significant anomalies (Fig. 6a).

Concerning the compositions of different muscovite fractions, their Li- and Cs-contents plot in the MSC- and MSCB-type pegmatite class fields after Černý and Burt (1984) (Figs 6b–c), while their Sr-concentrations are consistently <10 ppm (Table 2, Fig. 6d). Some fractionation is reflected by the lower Sr-concentrations of muscovite from sample M1210 (Fig. 6d). This is consistent with the significantly lower Sr-concentration of the corresponding whole rock (18.3 ppm in M1210, Table 2), which results in a higher $^{87}\text{Rb}/^{86}\text{Sr}$ ratio of 29.7 in sample M1210 compared to 4.8–12.8 in the other whole rock samples. Sample HM00305 shares similar compositional and isotopic features with M1210 (Table 2) having lower Sr-concentrations and consequently higher $^{87}\text{Rb}/^{86}\text{Sr}$ and $^{87}\text{Sr}/^{86}\text{Sr}$ ratios compared to the other samples. The $^{87}\text{Sr}/^{86}\text{Sr}$ ratios of

0.93838 (M1210) and 0.85 (HM00305) are significantly larger compared to the other samples, which range from 0.747920 to 0.776630 (Table 2). Calculating a Rb–Sr whole rock regression age using all samples from the current study with data from Haas (1985), results in a poorly defined age of 257 ± 130 Ma (Fig. 6e). Despite the common caveats, like isotopic inhomogeneity (e.g. Brooks et al., 1968) and the huge error, the result is still consistent with a pegmatite forming event in the Permo–Triassic (cf. Haas, 1985). Furthermore, the data point to a relatively unfractionated nature of the Permian pegmatites from the Matsch unit and to the absence of significant modification during the Cretaceous tectonometamorphic overprint.

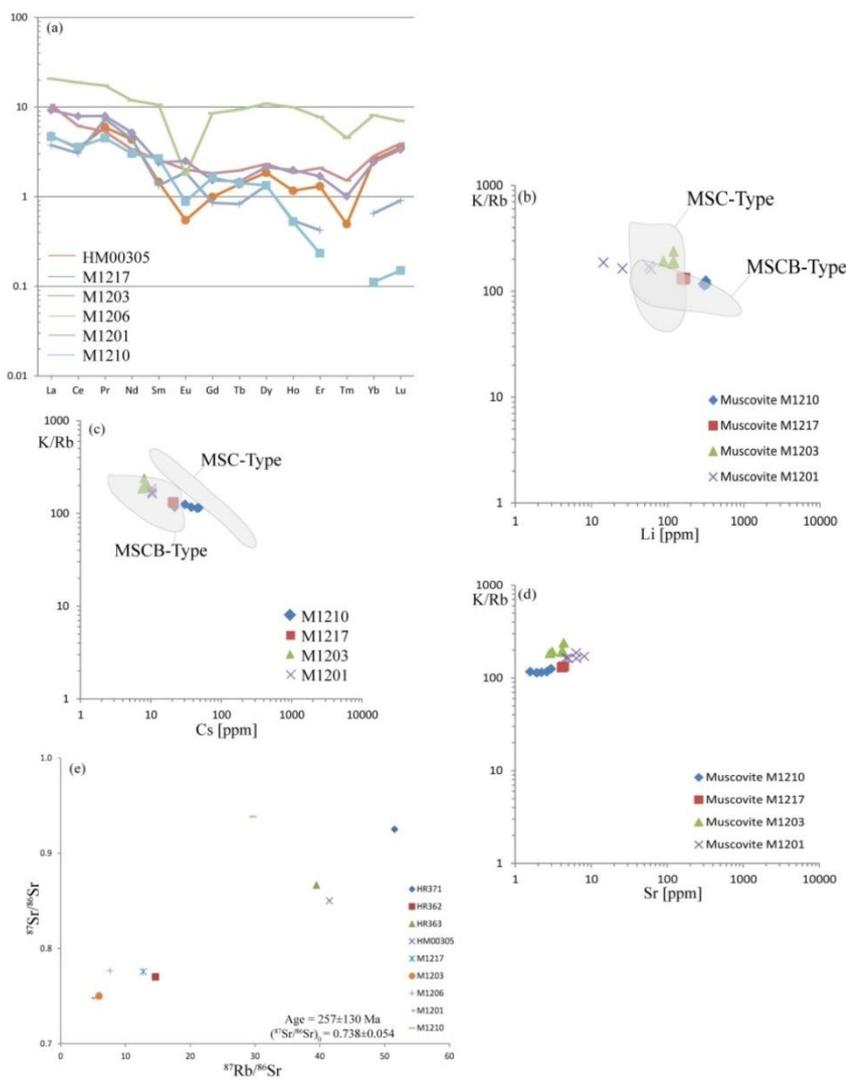


Figure 6 Compositional characteristics of Permian pegmatites and magmatic muscovites. (a) Chondrite–normalised REE pattern of the pegmatites (CI–values from Sun and McDonough, 1989), (b) K/Rb vs Li and (c) K/Rb vs Cs of the muscovites classify the pegmatites as MSC– and MSCB–types after Černý and Burt (1984), (d) K/Rb vs Sr of the muscovites and (e) Rb–Sr whole rock data of the pegmatites.

4.4.2. Muscovite

With the exception of Nd, all REE in muscovite generally have contents of <1 ppm (Table C1 in the appendix). Despite of the low concentrations, the chondrite-normalised REE-pattern of the different muscovite fractions share the following similarities (Fig. 7): (i) there is almost no REE-fractionation, (ii) positive Pr–Nd–(Eu–)Dy-anomalies are recognised in all samples and (iii) no correlation between deformation intensity and REE-pattern or –concentration exists (Fig. 7). Additionally, no correlation between REE-pattern and Rb–Sr muscovite-whole rock ages can be identified (Fig. 7 and Table 2).

Table 2 ID–TIMS Rb/Sr analytical results for the Permian metapegmatites and the well-defined grain size- and magnetic fractions of muscovite Wm I. FeO-concentrations are the mean of up to 50 EPMA-analyses from the embedded aliquotes. (n.m. = not measured; nm = non-magnetic at □Volts; m = magnetic at □Volts; Rb–Sr muscovite-whole rock ages have been calculated with a decay constant of $1.42 \cdot 10^{-11} \text{a}^{-1}$). From top to bottom, samples are ordered by deformation intensity.

Sample No.	Material	FeO [wt.%(n=50)]	Rb [ppm]	Sr [ppm]	⁸⁷ Rb/ ⁸⁶ Sr	1% error on ⁸⁷ Rb/ ⁸⁶ Sr	⁸⁷ Sr/ ⁸⁶ Sr	2σ error on ⁸⁷ Sr/ ⁸⁶ Sr	Wr-Ms age in Ma	2σ
Meta-pegmatite M1210										
TE-F0	whole-rock		183.611	18.303	29.686	0.297	0.938380	0.000007		
TE-F1	Ms 250-450µm; nm 28V	1.39	737.368	2.034	1525.002	15.250	5.343540	0.000034	207.2 ± 2.1	
TE-F2	Ms 250-450µm; m 28V	n.m.	747.002	2.545	1229.513	12.295	5.283590	0.000060	254.6 ± 2.6	
TE-F3	Ms >450µm; m 32V	1.42	739.227	1.678	1924.694	19.247	5.917890	0.000073	184.8 ± 1.8	
TE-F4	Ms >450µm; nm 42V	1.39	740.145	1.912	1652.256	16.523	5.560900	0.000089	200.3 ± 2.0	
TE-F5	Ms >450µm; m 42V	1.41	723.129	1.605	1954.416	19.544	5.807510	0.000040	177.9 ± 1.8	
Meta-pegmatite M1217										
TE-B0	whole-rock		143.280	32.670	12.777	0.128	0.775608	0.000004		
TE-B1	Ms 250-450µm; nm 28V	1.75	683.035	4.557	503.937	5.039	2.360024	0.000021	226.8 ± 2.3	
TE-B2	Ms 250-450µm; m 28V	n.m.	658.710	5.446	397.658	3.977	2.098390	0.000012	241.6 ± 2.4	
TE-B3	Ms >450µm; m 32V	2.13	687.763	4.511	514.235	5.142	2.399020	0.000033	227.6 ± 2.3	
TE-B4	Ms >450µm; nm 42V	1.69	699.345	4.238	562.426	5.624	2.524294	0.000033	223.7 ± 2.2	
TE-B5	Ms >450µm; m 42V	1.95	690.839	4.984	470.242	4.702	2.468850	0.000061	260.2 ± 2.6	
Meta-pegmatite HM00305										
TE-A0	whole-rock		114.536	8.101	41.487	0.415	0.850000	0.000024		
TE-A1	Ms >250µm (125-250); m 40V	n.m.	503.512	1.611	1315.536	13.155	5.358590	0.000040	248.8 ± 2.5	
TE-A2	Ms >250µm (100-125); nm 40V	n.m.	520.622	1.469	1528.300	15.283	5.720270	0.000066	230.3 ± 2.3	
TE-A3	Ms >250µm (125-250); nm 40V	n.m.	513.711	1.216	1913.250	19.132	6.484900	0.000132	211.7 ± 2.1	
Meta-pegmatite M1203										
TE-C0	whole-rock		104.092	50.880	5.945	0.059	0.750029	0.000003		
TE-C1	Ms 250-450µm; nm 28V	1.74	467.598	3.179	475.757	4.758	1.909100	0.000079	173.5 ± 1.7	
TE-C2	Ms 250-450µm; m 28V	2.25	463.459	4.211	352.149	3.521	1.787880	0.000014	210.8 ± 2.1	
TE-C3	Ms >450µm; m 32V	2.25	470.185	4.765	317.251	3.173	1.843320	0.000025	246.9 ± 2.5	
TE-C4	Ms >450µm; nm 42V	1.83	480.822	3.498	448.636	4.486	2.014660	0.000024	200.9 ± 2.0	
TE-C5	Ms >450µm; m 42V	1.93	472.759	3.576	427.628	4.276	1.910080	0.000056	193.5 ± 1.9	
Meta-pegmatite M1201										
TE-E0	whole-rock		90.562	54.114	4.862	0.049	0.747920	0.000005		
TE-E1	Ms 250-450µm; nm 28V	1.54	503.495	4.702	339.197	3.392	1.675110	0.000002	195.0 ± 1.9	
TE-E2	Ms 250-450µm; m 28V	n.m.	488.808	4.352	354.292	3.543	1.627210	0.000024	177.0 ± 1.8	
TE-E3	Ms >450µm; m 32V	1.51	519.020	3.317	507.537	5.075	1.944220	0.000026	167.4 ± 1.7	
TE-E4	Ms >450µm; nm 42V	1.45	525.991	3.610	473.937	4.739	1.975890	0.000004	184.1 ± 1.8	
TE-E5	Ms >450µm; m 42V	1.53	495.373	2.978	541.813	5.418	1.989970	0.000020	162.7 ± 1.6	
Meta-pegmatite M1206										
TE-D0	whole-rock		142.667	54.404	7.640	0.076	0.776630	0.000004		
TE-D1	Ms >250µm; nm 20V	n.m.	927.251	8.880	329.377	3.294	1.627490	0.000015	186.0 ± 1.9	

Rb-concentrations among the different muscovite fractions of single samples show only small fluctuations (Fig. 9d, Table 2), like in M1210, in which the difference in Rb-concentration between the fractions with highest and lowest Rb-concentrations is ~24 ppm, at total concentrations of >700 ppm. In comparison, Sr often varies by more than

20 % relative. For example, in M1210, the difference between the grain-size and magnetic fractions TE-F2 and TE-F5 is 0.94 ppm, which is, at these concentration levels, a deviation of 36% relative (Table 2). Consistent with the whole rock data (see section 4.4.1), muscovite from samples M1210 and HM00305 are slightly different than those from all other samples. Firstly, they have significantly lower Sr-concentrations of <2.5 ppm, compared to the other samples with Sr-concentrations of 3–8 ppm. Secondly, their $^{87}\text{Rb}/^{86}\text{Sr}$ ratios at 1200–2000 and $^{87}\text{Sr}/^{86}\text{Sr}$ ratios at 5.2–6.5 are correspondingly larger than those from muscovite fractions of the other samples (Table 2). Despite this fact, the distinct muscovite fractions of 5 samples with several muscovite grain size- and magnetic fractions share the following common features (Fig. 8; Table 2): (i) different muscovite fractions within single samples show a positive correlation of $^{87}\text{Rb}/^{86}\text{Sr}$ and $^{87}\text{Sr}/^{86}\text{Sr}$, with (ii) poorly defined muscovite-internal regression ages ranging from 62 ± 39 to 164 ± 170 Ma. (iii) All samples, except M1201 and M1206, have at least one muscovite fraction with a Permo-Triassic Rb-Sr mineral-whole rock age. (iv) The remaining muscovite fractions range at lower Sr-concentrations systematically related with higher $^{87}\text{Rb}/^{86}\text{Sr}$ ratios and therefore yield systematically decreasing calculated Rb-Sr mineral-whole rock ages within single samples, spanning an age difference of 32 Ma in sample M1201 and 76 Ma in sample M1210 at slightly increasing $^{87}\text{Sr}/^{86}\text{Sr}$ (Fig. 8, Table 2). In general, the mean Rb-Sr mineral-whole rock ages of up to 5 muscovite grain-size and magnetic fractions decrease from the weakly deformed sample M1217 (236 Ma) to the mylonitic sample M1201 (177 Ma), with the exception of M1210 in which the mean is 205 Ma (Fig. 8, Table 2).

A comparison of the FeO- and Sr- concentrations shows that the Sr variations do not correlate with the FeO-content and thus with the magnetic susceptibility of the respective fraction (Table 2). No other element is recognized to steadily decrease or increase with the calculated Rb-Sr muscovite-whole rock age or deformation intensity in all samples (Figs 7–9), suggesting that the variations in Sr are decoupled from the other elements as well. Be, Li, Cs and Rb are present in appreciable concentrations (Fig. 9). Although element concentration variations among the different muscovite fractions of single samples are very subtle, some correlation with the overall deformation intensity of the samples can be inferred. For example M1210 with the weakest deformational imprint shows the highest Li-, Be-, Cs- and Rb-contents, while they obviously decrease with progressive sample deformation intensity from M1217 to M1201 (Fig. 9).

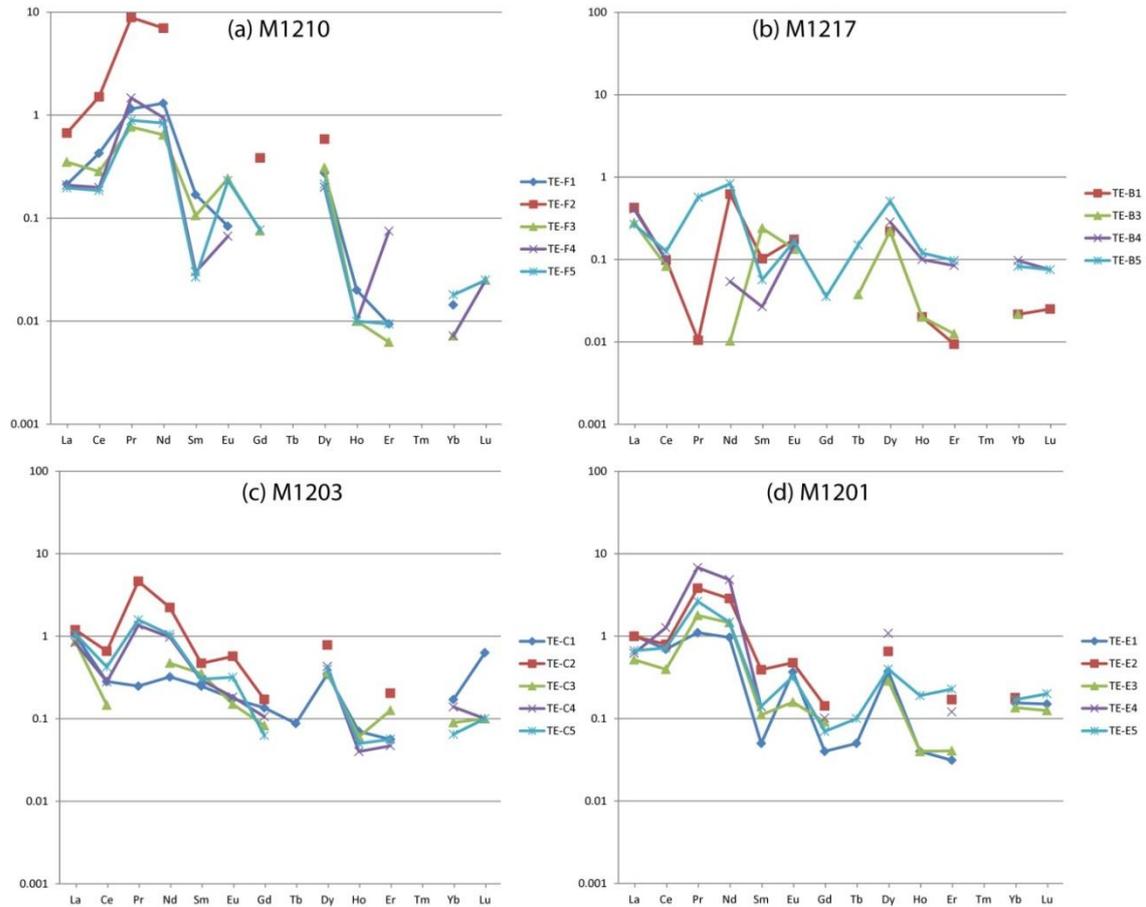


Figure 7 Chondrite-normalised REE-pattern of the different muscovite fractions.

5. Discussion

5.1. Permian magmatic stage

The formation of wide-spread pegmatites in the Austroalpine Unit of the European Eastern Alps has been attributed to a long-lasting HT/LP tectonometamorphic event during the Permian–Triassic (Schuster et al., 2001; Thöni et al., 2008). Sm–Nd garnet–whole rock data from Permian metapegmatites in the Upper–Austroalpine Matsch Unit point to pegmatite formation at 263–280 Ma (Habler et al., 2009). Despite potential isotopic inhomogeneity in granitic melts (e.g. Brooks et al., 1968) and the large associated error, the metapegmatite Rb–Sr whole rock regression age at 257 ± 130 Ma (Fig. 6e) is in agreement with pegmatite formation in the Permo–Triassic. The major and trace element data presented in this study indicate a rather unfractionated nature of the pegmatites. Only samples M1210 and HM00305 show some minor fractionation, as indicated by weak negative Eu–anomalies and low Sr–concentrations of the whole

rocks. M1210 is additionally characterised by some REE-fractionation and elevated Li-contents and high Cs-concentrations of the whole rock and of muscovite (Fig. 6, Table C1). The low Sr-concentrations and the Eu-anomalies are possibly caused by fractionation of primary apatite, zoisite and/or plagioclase in the pegmatitic melt. The low Sr-concentrations of these samples and corresponding muscovites lead to relatively high $^{87}\text{Rb}/^{86}\text{Sr}$ whole rock ratios of >30 (compared to <10 in the other samples) and >1200 in muscovite, respectively. In turn, also the $^{87}\text{Sr}/^{86}\text{Sr}$ ratios are significantly higher (Figs 6e and 8, Table 2). However, the systematics of the obtained muscovite-whole rock ages are unaffected by these 'extreme' isotope ratios, supporting the assumption that the event causing the higher $^{87}\text{Rb}/^{86}\text{Sr}$ and $^{87}\text{Sr}/^{86}\text{Sr}$ ratios of the bulk rock composition occurred earlier than the Sr-loss in the muscovite.

5.2. The effect of deformation on the major and trace element composition of muscovite

Muscovite clasts from the studied Permian metapegmatites preserve evidence for grain-internal brittle and crystal-plastic deformation as indicated by the presence of cracks, undulose extinction, (micro-)kinks and dynamic recrystallisation, especially along kink planes (Fig. 2). Despite of partly intense mylonitisation of the Permian pegmatites during the Cretaceous tectonometamorphism (Fig. 1c), primary magmatic muscovite persisted as cm- to sub-mm-sized clasts (Fig. 2). They largely retained their magmatic major element composition of nearly pure muscovite endmember, as reflected by their relatively homogeneous major element composition. According to combined microstructural and mineral compositional characteristics, fine-grained matrix muscovite (Wm III) formed by new muscovite crystallisation, mechanical dismembering, recrystallisation by dissolution-precipitation creep, and dynamic recrystallisation. Their formation is spatially clearly related with deformation microstructures: they represent the mylonitic foliation of the quartzo-feldspathic rock matrix; they crystallised in strain shadows of coarse-grained Ms-clasts and along cracks within Ms-clasts; crystallisation occurred at sites of high dislocation densities like kink planes of primary clasts (Fig. 2). Significant compositional changes of muscovite occurred in relation with dynamic recrystallisation producing Wm III, especially in the mylonitic matrix and along cracks and kink planes and chemical alteration producing Wm II on rims, along cracks and muscovite (001) cleavage planes (Figs 3c-h). The normalised REE-concentrations of the muscovite fractions indicate, that the REE characteristics of the differently strained samples are similar (Fig. 7).

Thus, it is concluded, that the REE characteristics of muscovite largely remain unaffected by deformation. The only element with systematic variations in all samples is Sr, which decreases with decreasing Rb–Sr muscovite–whole rock ages (Fig. 8). The major element characteristics of the almost pure muscovite endmember of Permian relic muscovite (Wm I) obviously remained unaffected by Cretaceous deformation in undeformed core domains (Fig. 3) and thus are interpreted to reflect the primary composition of the muscovite grains. However, the concentrations of Li, Be, Cs and Rb are obviously related to total finite strain of the pegmatite (Fig. 9). The concentrations of these elements in muscovite generally decrease from the undeformed metapegmatite M1210 to the mylonitic metapegmatite M1201 (Fig. 9). However, these concentration gradients are additionally affected by bulk rock compositional variations among the different pegmatite bodies, caused by magmatic fractionation (e.g. in M1210).

5.3. The effect of deformation on the Rb–Sr and Sm–Nd isotopic systems of muscovite

Microstructurally relic muscovite clasts have previously been shown to reflect incomplete isotopic resetting (e.g. Villa, 1998; Glodny et al., 2008), whereas dynamic recrystallisation and (neo–)crystallisation were supposed to lead to complete isotopic resetting (Yund and Tullis, 1991; Freeman et al., 1997; Villa, 1998; Glodny et al., 2002; Glodny et al., 2008). Permo–Triassic Rb–Sr muscovite–whole rock ages of the investigated samples confirm their relict character with respect to the Rb–Sr isotopic system.

Based on theoretical considerations, deformation is expected to have an effect on the Rb–Sr geochronometer, comparable with the effect on the Ar–retentivity of muscovite (e.g. Mulch et al., 2002; Kramar et al., 2003). Deformation may introduce dislocations, point defects, new grain boundaries and cracks, all of which reduce the effective diffusion domain size, which is then smaller as the initial primary grain size of the undeformed muscovite. Therefore, deformation at upper–greenschist facies P–T conditions ($T \leq 500^\circ\text{C}$) is supposed to be the predominant factor in affecting the Rb–Sr isotopic system of microstructurally relic muscovite (cf. Freeman et al., 1997; Villa, 1998; Glodny et al., 1998; Müller et al., 1999).

In contrast, the Sm–Nd system of muscovite from the investigated meta–pegmatite samples remained unaffected by deformation, as implied by the characteristics of the chondrite–normalised REE pattern and the absence of any correlation between

deformation intensity, Rb–Sr muscovite–whole rock age and Nd–concentrations (Fig. 7; Table C1). This is most likely due to the relatively low metamorphic temperatures, which were obviously below the (currently unknown) closure temperature for the Sm–Nd system in muscovite, causing Nd to be less mobile than Sr. Besides, Rb and Sm occupy different crystallographic sites in muscovite. Sr is located at the relatively large interlayer site, while Nd is expected to occupy an octahedral site.

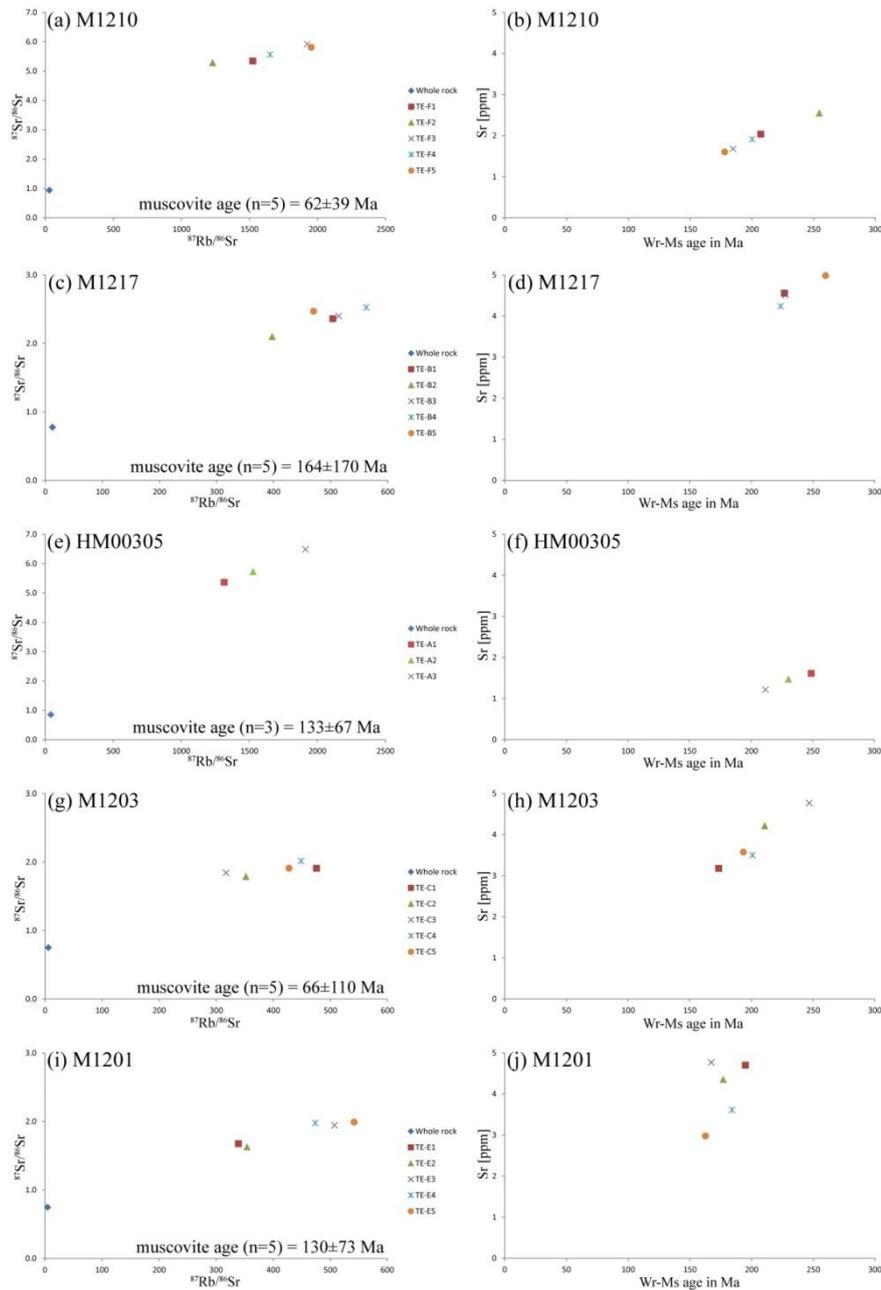


Figure 8 ID–TIMS Rb/Sr data plotted in $^{87}\text{Rb}/^{86}\text{Sr}$ vs $^{87}\text{Sr}/^{86}\text{Sr}$ space (left column) and Sr–concentrations vs Rb–Sr muscovite–whole rock age (right column) for (a–b) M1210, (c–d) M1217, (e–f) HM00305, (g–h) M1203 and (i–j) M1201. Age values in the left column refer to muscovite–internal regression ages. Note the scatter of these ages around the time of the Cretaceous event and the positive correlation of Sr in muscovite with the in muscovite–whole rock age.

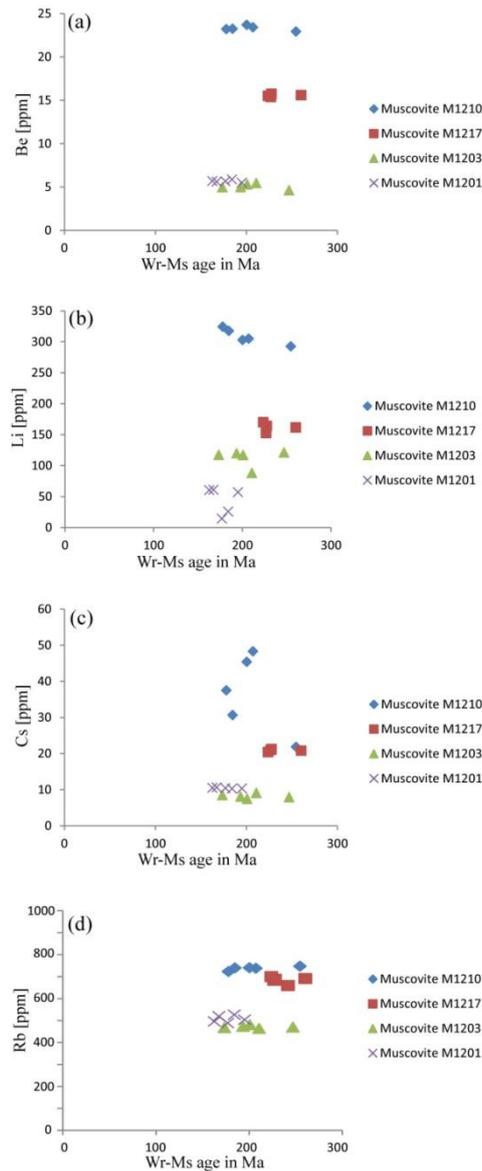


Figure 9 Plots of (a) Be-, (b) Li-, (c) Cs- and (d) Rb-concentrations vs Rb-Sr muscovite-whole rock age. Note, that none of these elements show a positive correlation with the mineral-whole rock age.

Even for single samples, analyses of multiple grain size- and magnetic fractions of Wm I yielded a range of different Rb-Sr muscovite-whole rock ages positively correlating with their Sr-concentration (Fig. 8, Table 2). Deformation-induced defects, such as dislocations, point defects, new grain boundaries and cracks have acted as high-diffusivity pathways, allowing the incompatible Sr to leave the crystal lattice more easily through multipath diffusion (Lee, 1995). Wm I grain size- and magnetic fractions with the lowest Sr-concentrations and the lowest Rb-Sr muscovite-whole rock ages most likely represent more strongly deformed parts of Wm I clasts. Additionally, the

absence of any correlation between grain size and Rb–Sr muscovite–whole rock age, points to the negligible effect of temperature–dependent volume diffusion (Dodson, 1973, Table 2). Furthermore, the theory implies that the loss of ^{87}Sr controls the Rb–Sr geochronometer. More precisely it is a loss of Sr_{total} as there is a positive correlation between the $^{87}\text{Rb}/^{86}\text{Sr}$ and the $^{87}\text{Sr}/^{86}\text{Sr}$ ratios (Fig. 8, Table 2). The proposed scenarios (Fig. 10) include 3 different possible situations of Sr_{total} loss at different stages during the meta–pegmatite evolution, which lead to a Cretaceous muscovite isochron age without establishing Cretaceous bulk rock isotopic rehomogenisation. Within these scenarios, the effect of a preferential loss of the radiogenic ^{87}Sr is likely to have only minor effects as the resulting muscovite–internal isochron ages would simply be lower than in the proposed models (Fig. 10).

Sr loss scenario I (Fig. 10a)

Primary magmatic muscovite is presumed to initially have a homogeneous $^{87}\text{Rb}/^{86}\text{Sr}$ and to be in isotopic equilibrium with the whole rock. Between the Permo–Triassic HT/LP event and the Cretaceous greenschist metamorphic overprint, Sr may have remained partly mobile, due to constantly elevated temperatures in the middle crust (Schuster and Stüwe, 2008). Thus, the primary muscovite is supposed to permanently lose Sr to varying degrees, while the isotope ratios consequently change along the different growth lines with slopes deviating from -1 (1). During the Cretaceous, different muscovite fractions with internally homogenised $^{87}\text{Sr}/^{86}\text{Sr}$ ratios may have formed (2). In the following time up to the present–day, the growth line (3) will approximately be half the length of (1) as the time span between the Cretaceous and the present–day is about half that between the Permo–Triassic and the Cretaceous. Today, the different muscovite fractions are muscovite–internally aligned, with a slope equalising an ‘age’ of c.90 Ma (4), which corresponds to the timing of the Eo–Alpine tectonometamorphic event with deformation at upper–greenschist facies conditions and hence the Sr_{total} –loss.

Scenario II (Fig. 10b)

An alternative scenario presumes muscovite with initial zoning in $^{87}\text{Rb}/^{86}\text{Sr}$ ratio (1) and isotopic equilibration with the whole rock. Their isotope ratios are supposed to develop along the growth lines (2). During the Cretaceous tectonometamorphic event, Sr–loss of muscovite is supposed to increase the $^{87}\text{Rb}/^{86}\text{Sr}$ ratios at constant $^{87}\text{Sr}/^{86}\text{Sr}$ but

without isotopic rehomogenisation. Muscovite with initially higher $^{87}\text{Rb}/^{86}\text{Sr}$ ratios may experience stronger Sr-loss effects, as they are supposed to represent rims and more strongly deformed domains of a muscovite clast (3). Consequently, the resulting muscovite–internal isochron today (4) is supposed to yield an age between the Permian and the Cretaceous (5). Undeformed, central parts of muscovite clasts with relatively lowest $^{87}\text{Rb}/^{86}\text{Sr}$ and $^{87}\text{Sr}/^{86}\text{Sr}$ ratios may thus have retained their originally Permo–Triassic formation/cooling ages.

Scenario III (Fig. 10c)

The third scenario is based on the presumption of muscovite with a homogeneous initial $^{87}\text{Rb}/^{86}\text{Sr}$ ratio and variable Sr-loss during the Cretaceous event (1–2). The evolving muscovite–internal isochron would, as in Scenario I, correspond to the Cretaceous age corresponding to the time of Sr-loss (4).

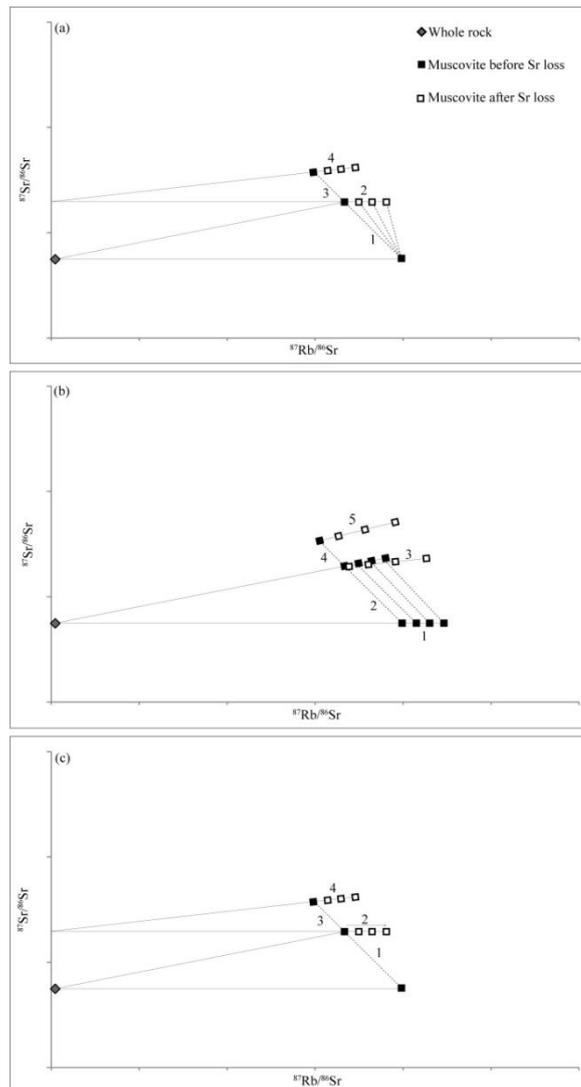


Figure 10 (previous page) Simplified sketch representing 3 different scenarios of how Sr-loss may affect the Rb–Sr geochronometer: (a) Permanent Sr loss of initially homogeneous muscovite between the Permo–Triassic and the Cretaceous; (b) Muscovite with initial $^{87}\text{Rb}/^{86}\text{Sr}$ zoning affected by Sr-loss during Cretaceous metamorphism; and (c) Single stage Cretaceous Sr-loss of initially homogeneous muscovite. See text for detailed discussion.

5.3.1. Discussion of the scenarios I–III

Poorly defined muscovite–internal regression ages in our samples range from 62 ± 39 to 164 ± 170 Ma (cf. Fig. 8) and support one or a combination of more of the above mentioned scenarios (Fig. 10). The effects related to scenario I (Fig. 10a) may be rather limited because based on the available literature date the pegmatite bearing units cooled below 500°C still in Triassic time (Schuster and Stüwe, 2008). Therefore partial Sr mobility might have been established only for some decades after the intrusion of the pegmatites at 263–280 Ma (Habler et al., 2009). Scenario II including zoned muscovite seems to be more relevant, as muscovite growing in a pegmatitic melt is subjected to changes of the $^{87}\text{Rb}/^{86}\text{Sr}$ ratio during growth, as contemporaneously growing (anorthitic) feldspar and apatite fractionate Sr from the pegmatitic melt. Additionally, zoisite as a Sr-bearing phase could theoretically fractionate Sr, but there is no direct evidence for the presence of primary zoisite in the pegmatites. However, it is rather arbitrary to assign muscovite with the highest $^{87}\text{Rb}/^{86}\text{Sr}$ to the rims as zoning is possibly more complex (cf. Roycroft, 1991; Viana et al., 2007). High $^{87}\text{Rb}/^{86}\text{Sr}$ ratios might as well correlate with more internal parts of large clasts. There Sr-loss may have preferentially occurred within kinked or cracked zones. The third scenario is based on one muscovite with homogeneous initial $^{87}\text{Rb}/^{86}\text{Sr}$ as scenario I. Different parts of the crystal lose variable amounts of Sr due to different deformation intensity, successively increasing the $^{87}\text{Rb}/^{86}\text{Sr}$ ratio ((2) in Fig. 10c). As the initial Rb/Sr zonation of muscovite remains unknown, this third scenario is supposed to be equally likely as scenario II. The present-day situation (Fig. 8) is consistent with either scenario II or III or a combination of both. In cases of variations in ^{87}Sr loss, the influence of deformation was supposedly related with alteration by a fluid phase. However, the presented models compared with the new data share one important characteristic: there is one muscovite fraction present in all samples, except M1201 and M1206, which does not significantly lose Sr and therefore preserved its initial Permo–Triassic formation/cooling age (Fig. 8, Table 2). At least, these are well in line with the Sm–Nd garnet–whole rock data,

pointing to pegmatite formation at 263–280 Ma (Habler et al., 2009) and subsequent cooling below *c.* 500–550°C at 240–260 Ma (Fig. 8; Table 2).

Sr, released from muscovite may have been either removed from the rock system via a fluid phase, or incorporated into one or more of the syntectonic phases apatite, clinozoisite/allanite or feldspar (Figs 3a–b), which at least bear some Sr (see section 4.3.2.). However, due to the small variations in the Sr-concentrations and the $^{87}\text{Sr}/^{86}\text{Sr}$ ratios in apatite and feldspar the determination of their Sr source remains an analytical challenge.

6. Conclusions

Muscovite clasts from Permian metapegmatites of the Upper–Austroalpine Matsch Unit in Southern Tyrol (Italy) provide information on the behaviour of Sr in muscovite and the associated effects on the Rb–Sr geochronometer during upper greenschist facies deformation:

1. New Rb/Sr data indicate significant effects of deformation–related Sr_{total} –loss on the Rb–Sr geochronometer. Kink planes, subgrain boundaries and cracks show major element compositional alteration and may provide short–circuit diffusion (fast–diffusion) pathways for incompatible Sr.
2. Based on BSE images, quantitative element mapping by EMPA and single spot analyses, 3 distinct muscovite groups were identified in Permian metapegmatite: (i) Wm I represents primary magmatic Permian muscovite with almost pure muscovite endmember composition; (ii) Wm II forms portions of Ms clasts, which were affected by alteration/dissolution–reprecipitation; and (iii) Wm III appears as fine–grained microstructurally distinct Ms generation, which is largely compositionally similar to Wm II, but results from (neo)crystallisation in the rock matrix and strain shadows, or from dynamic recrystallisation in highly strained portions of coarse grained clasts (Figs 2–3).
3. Two hypothetical scenarios of Rb–Sr isotopic evolution are consistent with the presented major, trace and Rb–Sr isotope dataset. Scenario II comprises initial muscovite zoning affected by Cretaceous Sr–loss without isotopic rehomogenisation, whereas scenario III presumes a homogeneous magmatic muscovite generation variably overprinted by Cretaceous Sr loss.

4. All samples show a positive internal correlation of $^{87}\text{Rb}/^{86}\text{Sr}$ and $^{87}\text{Sr}/^{86}\text{Sr}$ ratios of their muscovite irrespective of their finite strain magnitude.
5. All samples, except M1201 and M1206, comprise a primary magmatic muscovite fraction that has not been significantly affected by Sr_{total} -loss and hence preserves the original Permo–Triassic formation/cooling age.
6. A whole–rock Rb–Sr errorchron from Permian pegmatites is in line with a pegmatite formation during the Permo–Triassic HT/LP event, suggesting the whole rock systems have remained largely closed systems during Cretaceous tectonometamorphic overprinting.
7. Investigation of different grain size– and magnetic fractions from single samples provides a comprehensive dataset documenting significant systematic variations in the Rb–Sr system even at hand specimen scale. Mean ages of different muscovite grain–size and magnetic fractions decrease from the weakly deformed sample M1217 (236 Ma) to the mylonitic sample M1201 (177 Ma), hence documenting a significant effect of deformation on the muscovite Rb–Sr geochronometer at upper–greenschist facies conditions.

7. Acknowledgements

Funding was provided by the University of Vienna (Doctoral School IK052) and the Austrian Science Fund (FWF): I471–N19 as part of the International Research Group FOR 741 D–A–CH. The authors acknowledge access to the Electron Microprobe Laboratory and the Laboratory of Geochronology at the Faculty of Geosciences, Geography and Astronomy at the University of Vienna (Austria). S. Hrabe and C. Beybel are thanked for excellent thin section preparation, F. Biedermann for valuable help during the mineral separation, M. Horschinegg for assistance with the ID–TIMS analyses and T.Ntaflos and F. Kiraly for help with the EPMA analyses.

8. References

Armstrong, R.L., Jäger, E., Eberhardt, P., 1966. A comparison of K–Ar and Rb–Sr ages on Alpine biotites. *Earth and Planetary Science Letters* 1, 13–19.

- Baldwin, S.L., Lister, G.S., 1998. Thermochronology of the South Cyclades Shear Zone, Ios, Greece: Effects of ductile shear in the argon partial retention zone. *Journal of Geophysical Research* 103, 7315–7336.
- Bell, I.A., Wilson, C.J.L., McLaren, A.C., Etheridge, M.A., 1986. Kinks in mica: role of dislocations and (001) cleavage. *Tectonophysics* 127, 49–65.
- Beltrando, M., Di Vincenzo, G., Ferraris, C., 2013. Preservation of sub-microscopic structural relicts in micas from the Gran Paradiso Massif (Western Alps): Implications for $^{40}\text{Ar}/^{39}\text{Ar}$ geochronology. *Geochimica et Cosmochimica Acta* 119, 359–380.
- Blanckenburg, F.v., Villa, I., Baur, H., Morteani, G., Steiger, R.H., 1989. Time calibration of a PT-path from the Western Tauern Window, Eastern Alps: the problem of closure temperatures. *Contributions to Mineralogy and Petrology* 101, 1–11.
- Bröcker, M., Baldwin, S.L., Arkudas, R., 2013. The geological significance of $^{40}\text{Ar}/^{39}\text{Ar}$ and Rb–Sr white mica ages from Syros and Sifnos, Greece: a record of continuous (re)crystallization during exhumation?. *Journal of Metamorphic Geology* 31, 629–646.
- Brooks, C., Wendt, I., Harre, W., 1968. A two-error regression treatment and its application to Rb–Sr and initial $\text{Sr}^{87}/\text{Sr}^{86}$ ratios of younger variscan granitic rocks from the Schwarzwald Massif, southwest Germany. *Journal of Geophysical Research*, 73, 6071–6084.
- Černý, P., Burt, D.M., 1984. Paragenesis, crystallochemical characteristics and geochemical evolution of micas in granite pegmatites. In: *Micas* (ed Bailey, S.W.), Mineralogical Society of America, *Reviews in Mineralogy*, Volume 13, 257–297.
- Cosca, M., Stünitz, H., Bourgeix, A.L., Lee, J.P., 2011. $^{40}\text{Ar}^*$ loss in experimentally deformed muscovite and biotite with implications for $^{40}\text{Ar}/^{39}\text{Ar}$ geochronology of naturally deformed rocks. *Geochimica et Cosmochimica Acta* 75, 7759–7778.

- Dempster, T.J., Tanner, P.W.G., Ainsworth, P., 1994. Chemical zoning of white micas: A record of fluid infiltration in the Oughterard granite, western Ireland. *American Mineralogist* 79, 536–544.
- Dodson, M.H., 1973. Closure Temperature in Cooling Geochronological and Petrological Systems. *Contributions to Mineralogy and Petrology* 40, 259–274.
- Dunlap, W.J., Kronenberg A.K., 2001. Argon loss during deformation of micas: constraints from laboratory deformation experiments. *Contributions to Mineralogy and Petrology* 141, 174–185.
- Freeman, S.R., Inger, S., Butler, R.W.H., Cliff, R.A., 1997. Dating deformation using Rb–Sr in white mica: Greenschist facies deformation ages from the Entrelor shear zone, Italian Alps. *Tectonics* 16/1, 57–76.
- Ganguly, J., Ruiz, J., 1987. Time–temperature relation of mineral isochrons: A thermodynamic model, and illustrative examples for the Rb–Sr system. *Earth and Planetary Science Letters* 81, 338–348.
- George, M.T., Bartlett, J.M., 1996. Rejuvenation of Rb–Sr mica ages during shearing on the northwestern margin of the Nanga Parbat–Haramosh massif. *Tectonophysics* 260, 167–185.
- Glodny, J., Grauert, B., Fiala, J., Vejnar, Z., Krohe, A., 1998. Metapegmatites in the western Bohemian massif: ages of crystallization and metamorphic overprint, as constrained by U–Pb zircon, monazite, garnet, columbite and Rb–Sr muscovite data. *Geologische Rundschau* 87, 124–134.
- Glodny, J., Bingen, B., Austrheim, H., Molina, J., Rusin, A., 2002. Precise eclogitization ages deduced from Rb/Sr mineral systematics: The Maksyutov complex, Southern Urals, Russia. *Geochimica et Cosmochimica Acta* 66/7, 1221–1235.
- Glodny, J., Austrheim, H., Molina, J., Rusin, A., Seward, D., 2003. Rb/Sr record of fluid–rock interaction in eclogites: The Marun–Keu complex, Polar Urals, Russia. *Geochimica et Cosmochimica Acta* 67/22, 4353–4371.

- Glodny, J., Kühn, A., Austrheim, H., 2008. Diffusion versus recrystallization processes in Rb–Sr geochronology: Isotopic relics in eclogite facies rocks, Western Gneiss Region, Norway. *Geochimica et Cosmochimica Acta* 72, 506–525.
- Gomes, M.E.P., Neiva, A.M.R., 2000. Chemical zoning of muscovite from the Ervedosa granite, northern Portugal. *Mineralogical Magazine* 64, 347–358.
- Haas, R., 1985. Zur Metamorphose des südlichen Ötztalkristallins unter besonderer Berücksichtigung der Matscher Einheit (Vinschgau/Südtirol). PhD thesis, University of Innsbruck, 118 pages.
- Habler, G., Thöni, M., Sölva, H., 2006. Tracing the high pressure stage in the polymetamorphic Texel Complex (Austroalpine basement unit, Eastern Alps): P–T–d constraints. *Mineralogy and Petrology* 88, 269–296.
- Habler, G., Thöni, M., Grasemann, B., 2009. Cretaceous metamorphism in the Austroalpine Matsch Unit (Eastern Alps): The interrelation between deformation and chemical equilibration processes. *Mineralogy and Petrology* 97, 149–171.
- Hames, W.E., Cheney, J.T., 1997. On the loss of $^{40}\text{Ar}^*$ from muscovite during polymetamorphism. *Geochimica et Cosmochimica Acta* 61, 3863–3872 .
- Jäger, E., 1967. Die Bedeutung der Biotit–Alterswerte. In: Rb–Sr Altersbestimmungen an Glimmern der Zentralalpen. From E. Jäger, E. Niggli and E. Wenk (eds). *Beiträge zur Geologischen Karte der Schweiz, NF*, 134, 28–31.
- Jenkin, G.R.T., Rogers, G., Fallick, A.E., Farrow, C.M., 1995. Rb–Sr closure temperatures in bi–mineralic rocks: a mode effect and test for different diffusion models. *Chemical Geology* 122, 227–240.
- Jenkin, G.R.T., 1997. Do cooling paths derived from mica Rb–Sr data reflect true cooling paths?. *Geology* 25, 907–910.
- Jenkin, G.R.T., Ellam, R.M., Rogers, G., Stuart, F.M., 2001. An investigation of closure temperature of the biotite Rb–Sr system: The importance of cation exchange. *Geochimica et Cosmochimica Acta* 65, 1141–1160.
- Kühn, A., Glodny, J., Iden, K., Austrheim, H., 2000. Retention of Precambrian Rb/Sr phlogopite ages through Caledonian eclogite facies metamorphism, Bergen Arc Complex, W–Norway. *Lithos* 51, 305–330.

- Kramar, N., Cosca, M., Buffat, P.A., Baumgartner, L., 2003. Stacking fault–enhanced argon diffusion in naturally deformed muscovite. From Vance, D, Müller, W and Villa, I (eds) 2003, *Geochronology: Linking the Isotopic Record with Petrology and Textures*. Geological Society, London, Special Publications 220, 249–260.
- Lee, J.K.W., 1995. Multipath diffusion in geochronology. *Contributions to Mineralogy and Petrology* 120, 60–82.
- Mulch, A., Cosca, M., Handy, M., 2002. In–Situ UV–laser $^{40}\text{Ar}/^{39}\text{Ar}$ geochronology of a micaceous mylonite: an example of defect–enhanced argon loss. *Contributions to Mineralogy and Petrology* 142, 738–752.
- Müller, W., Dallmeyer, D., Neubauer, F., Thöni, M 1999. Deformation–induced resetting of Rb/Sr and $^{40}\text{Ar}/^3\text{Ar}$ mineral systems in a low–grade, polymetamorphic terrane (Eastern Alps, Austria). *Journal of the Geological Society, London* 156, 261–278.
- Müller, W., Mancktelow, N., Meier, M 2000. Rb–Sr microchrons of synkinematic mica in mylonites: an examples from the DAV fault of the Eastern Alps. *Earth and Planetary Science Letters* 180, 385–397.
- Pouchou, J.L., Pichoir, F., 1991. Quantitative analysis of homogeneous or stratified microvolumes applying the model “PAP”. In: *Electron Probe Quantitation*, (eds Heinrich, K.F.J., Newbury, D.E.), 31–75.
- Purdy J.W., Jäger, E., 1976. K–Ar Ages on Rock–forming minerals from the Central Alps. *Memorie degli Istituti di Geologia e Mineralogia dell’Università di Padova* 30, 1–31.
- Purtscheller, F., 1967. Mineralzonen im Ötztal–Stubaiier Altkristallin. *Akad. Wiss. Math. Naturwiss. Kl., Wien*, 2, 66–70.
- Putnis, A., 2002. Mineral replacement reactions: from macroscopic observations to microscopic mechanisms. *Mineralogical Magazine* 66, 689–708.
- Ratschiller, L.K., 1953. Beiträge zur regionalen Petrographie des Vintschgau–Gebietes (Südtirol). *Neues Jahrbuch Mineralogische Abhandlungen* 85, 247–302.

- Reddy, S.M., Kelley, S.P., Wheeler, J., 1996. A $^{40}\text{Ar}/^{39}\text{Ar}$ laser probe study of micas from the Sesia Zone, Italian Alps: implications for metamorphic and deformation histories. *Journal of Metamorphic Geology* 14, 493–508.
- Roycroft, P., 1991. Magmatically zoned muscovite from the peraluminous two–mica granites of the Leinster batholith, southeast Ireland. *Geology* 19, 437–440.
- Schmid, S.M., Haas, R., 1989. Transition from near–surface thrusting to intrabasement decollement, Schlinig thrust, Eastern Alps. *Tectonics* 8, 697–718.
- Schmid, S.M., Fügenschuh, B., Kissling, E., Schuster, R., 2004. Tectonic map and overall architecture of the Alpine orogen. *Eclogae Geologicae Helvetiae* 97, 93–117.
- Schuster, R., Scharbert, S., Abart, R., Frank, W., 2001. Permo–Triassic extension and related HT/LP metamorphism in the Austroalpine–Southalpine realm. *Mitteilungen der Gesellschaft der Geologie– und Bergbaustudenten in Österreich* 45, 111–141.
- Schuster, R., Stüwe, K., 2008. The Permian Metamorphic Event in the Alps. *Geology* 36/8, 303–306.
- Steiger, R.H., Jäger, E., 1977. Subcommittee on Geochronology: Convention on the use of decay constants in geo– and cosmochronology. *Earth and Planetary Science Letters* 36, 359–362.
- Stipp, M., Stünitz, H., Heilbronner, R., Schmid, S., 2002. Dynamic recrystallization of quartz: correlation between natural and experimental conditions. In: *Deformation Mechanisms, Rheology and Tectonics: Current Status and Future Perspectives* (eds De Meer, S., Drury, M.R., De Bresser, J.H.P., Pennock, G.M.), Geological Society, London, Special Publications 200, 171–190.
- Sun, S.S., McDonough, W.F., 1989. Chemical and isotopic systematics of oceanic basalts: implications for mantle composition and processes. In: *Magmatism in the Ocean Basins* (eds Saunders, A.D., Norry, M.J.), Geological Society Special Publications, 42, 313–345.
- Thöni, M., 1981. Degree and Evolution of the Alpine Metamorphism in the Austroalpine Unit W of the Hohe Tauern in the light of K/Ar and Rb/Sr Age

Determinations on Micas. Jahrbuch der Geologischen Bundesanstalt 124–1, 111–174, Wien.

Thöni, M., 1983. The thermal climax of the early alpine metamorphism in the Austroalpine thrust sheet. *Memorie di Scienze Geologiche*, 36, 211–238.

Thöni, M., 1986. The Rb–Sr thin slab isochron method – An unreliable geochronological method for dating geological events in polymetamorphic terrains? – Evidence from the Austroalpine basement Nappe, The Eastern Alps. *Memorie die Scienze Geologiche*, 38, 283–352.

Thöni, M., Miller, C., Zanetti, A., Habler, G., Goessler, W., 2008. Sm–Nd isotope systematics of high–REE accessory minerals and major phases: ID–TIMS, LA–ICP–MS and EPMA data constrain multiple Permian–Triassic pegmatite emplacement in the Koralpe, Eastern Alps. *Chemical Geology* 254, 216–237.

Viana, R.R., Evangelista, H.J., Stern, W.B., 2007. Chemical zoning of muscovite megacrystals from the Brazilian Pegmatite Province. *Anais da Academia Brasileira de Ciências* 79, 431–439.

Villa, I., 1998. Isotopic closure. *Terra Nova* 10, 42–47.

Yund, R.A., Tullis, J., 1991. Compositional changes of minerals associated with dynamic recrystallization. *Contributions to Mineralogy and Petrology* 108, 346–355.

Appendix

Table A1 Measured values for the standards of the ICP–OES and ICP–MS analysis. Major element concentrations (Na, K, Ti, P) are given in wt.%, trace element concentrations (Ba–Lu) are in ppm.

A1	AGV1	BIR1	GSR2	SDC1	SG1A	SG3	W2	RGM1	QLO1
Na2O	4.24	1.80	3.85	2.02	5.55	4.23	2.19	4.19	4.05
K2O	2.98	0.03	1.86	3.23	4.13	4.69	0.64	3.65	4.31
TiO2	1.08	0.97	0.51	1.00	0.06	0.25	1.07	0.62	0.27
P2O5	0.50	0.02	0.24	0.14	0.01	0.02	0.13	0.05	0.27
Ba	1216.73	7.48	976.55	618.24	3.34	55.58	161.03	756.02	1278.14
Be	2.40	0.26	1.32	3.59	11.40	4.76	0.90	2.51	2.08
Li	10.23	2.74	18.37	34.55	390.37	55.56	8.91	51.03	22.42
Pb	36.36	2.75	9.91	22.98	230.99	9.46	7.85	25.04	22.92
Cs	1.28	0.45	2.30	4.00	12.00	4.50	0.99	9.60	1.75
La	39.15	0.73	20.06	41.73	17.25	39.01	10.49	22.97	26.61
Ce	70.90	2.17	39.55	90.62	47.98	82.82	23.27	43.57	49.55
Pr	8.21	0.49	4.57	10.31	4.26	11.10	3.03	5.04	6.32
Nd	32.11	3.11	18.10	41.74	10.93	47.42	12.73	19.39	24.90
Sm	5.98	1.04	3.20	7.53	2.25	9.64	3.13	3.87	4.34
Eu	1.61	0.51	0.94	1.53	0.07	0.32	1.09	0.55	1.17
Gd	4.78	1.73	2.37	6.70	2.60	8.21	3.61	3.37	4.27
Tb	0.60	0.33	0.29	1.00	0.66	1.25	0.54	0.48	0.65
Dy	3.57	2.48	1.77	6.09	6.10	8.03	3.72	3.54	3.75
Ho	0.68	0.54	0.26	1.19	1.79	1.71	0.74	0.78	0.91
Er	1.79	1.45	0.73	3.35	6.91	5.20	2.15	1.78	2.23
Tm	0.13	0.12	0.05	0.24	0.68	0.38	0.15	0.33	0.36
Yb	1.67	1.75	0.73	3.35	11.42	6.53	2.15	2.28	2.32
Lu	0.25	0.23	0.09	0.49	1.76	0.97	0.30	0.39	0.42

Table A2 Target values for the standards of the ICP–OES and ICP–MS analysis. Major element concentrations (Na, K, Ti, P) are given in wt.%, trace element concentrations (Ba–Lu) are in ppm.

A2	AGV1	BIR1	GSR2	SDC1	SG1A	SG3	W2	RGM1	QLO1
Na2O	4.26	1.75	3.86	2.05	5.46	4.24	2.14	4.07	4.20
K2O	2.91	0.03	1.89	3.28	4.14	4.64	0.63	4.30	3.60
TiO2	1.05	0.96	0.52	1.01	0.07	0.26	1.06	0.27	0.62
P2O5	0.49	0.05	0.24	0.16	0.01	0.02	0.13	0.05	0.25
Ba	1226.00	7.70	1020.00	630.00	19.00	90.00	182.00	807.00	1370.00
Be	2.10	0.58	1.10	3.00	10.00	5.00	1.30	2.37	1.89
Li	12.00	3.40	18.30	34.00	390.00	52.00	9.30	57.00	25.00
Pb	36.00	3.20	11.30	25.00	230.00	10.00	9.30	24.00	20.40
Cs	1.28	0.45	2.30	4.00	12.00	4.50	0.99	9.60	1.75
La	38.00	0.88	21.80	42.00	32.00	45.00	11.40	24.00	27.00
Ce	67.00	2.50	40.00	93.00	62.00	90.00	24.00	47.00	54.60
Pr	7.60	0.50	4.90	9.80	5.00	-	5.90	4.70	6.00
Nd	33.00	2.50	19.00	40.00	18.00	50.00	14.00	19.00	26.00
Sm	5.90	1.08	3.40	8.20	5.00	10.00	3.25	4.30	4.88
Eu	1.64	0.54	1.02	1.71	0.10	0.40	1.10	0.66	1.43
Gd	5.00	1.90	2.70	7.20	7.00	-	3.60	3.70	4.70
Tb	0.70	0.41	0.41	1.18	0.80	1.70	0.63	0.66	0.71
Dy	3.60	2.40	1.80	6.70	6.00	10.00	3.80	4.08	3.80
Ho	0.67	0.50	0.34	1.50	1.50	-	0.76	0.95	0.86
Er	1.70	1.80	0.85	4.10	6.00	6.00	2.50	2.60	2.30
Tm	0.34	0.27	0.15	0.65	1.10	-	0.38	0.37	0.37
Yb	1.72	1.70	0.89	4.00	12.00	7.00	2.05	2.60	2.32
Lu	0.27	0.26	0.12	0.53	1.90	0.90	0.33	0.41	0.37

Papers and manuscripts

Table B1 Representative EPMA analyses of muscovite

Wm Group Generation Sample	I			II			III			I			II			III		
	Permian	Cretaceous	Cretaceous	Permian	Cretaceous	Cretaceous	Permian	Cretaceous	Cretaceous	Permian	Cretaceous	Cretaceous	Permian	Cretaceous	Cretaceous	Permian	Cretaceous	Cretaceous
Position	clast	clast rim	matrix	clast	clast rim	matrix	clast	clast rim	matrix	clast	clast rim	matrix	clast	clast rim	matrix	clast	clast rim	matrix
SiO ₂	45.93	47.24	46.38	45.62	46.71	48.18	45.52	46.76	47.36	45.87	47.00	46.13	47.01	47.25	46.76			
TiO ₂	0.09	0.08	0.08	0.05	0.04	0.02	0.08	0.18	0.08	0.01	0.11	0.10	1.35	0.43	0.01			
Al ₂ O ₃	35.68	32.43	34.47	36.25	32.29	32.60	35.37	31.13	30.98	36.95	34.35	35.14	34.52	31.75	32.67			
Cr ₂ O ₃	0.01	0.00	0.00	0.00	0.00	0.00	0.00	0.00	0.01	0.00	0.00	0.00	0.00	0.00	0.00			
FeO	2.48	3.52	2.60	2.16	3.92	4.23	2.17	4.94	4.44	1.29	2.71	2.51	3.44	4.23	4.25			
MnO	0.00	0.02	0.01	0.00	0.03	0.04	0.01	0.04	0.02	0.02	0.03	0.01	0.01	0.00	0.02			
MgO	0.42	1.01	0.67	0.30	0.67	1.02	0.35	1.07	1.12	0.38	0.75	0.50	0.47	0.65	0.48			
CaO	0.01	0.08	0.03	0.01	0.00	0.00	0.00	0.00	0.00	0.00	0.00	0.01	0.00	0.00	0.00			
Na ₂ O	0.25	0.17	0.34	0.40	0.20	0.17	0.38	0.25	0.12	0.59	0.49	0.53	0.35	0.35	0.45			
K ₂ O	10.83	10.48	10.73	10.69	10.56	10.19	10.80	10.77	11.10	10.70	10.38	10.26	10.64	10.57	10.23			
Total	95.69	95.02	95.30	95.48	94.42	96.46	94.69	95.14	95.22	95.81	95.18	95.18	97.79	95.24	94.88			
Oxygens	11.00	11.00	11.00	11.00	11.00	11.00	11.00	11.00	11.00	11.00	11.00	11.00	11.00	11.00	11.00			
Si	3.06	3.18	3.11	3.04	3.18	3.20	3.07	3.18	3.21	3.04	3.13	3.09	3.08	3.19	3.16			
Ti	0.00	0.00	0.00	0.00	0.00	0.00	0.00	0.01	0.00	0.00	0.01	0.00	0.07	0.02	0.00			
Al	2.80	2.57	2.72	2.85	2.59	2.55	2.81	2.50	2.48	2.88	2.69	2.77	2.67	2.53	2.61			
Cr	0.00	0.00	0.00	0.00	0.00	0.00	0.00	0.00	0.00	0.00	0.00	0.00	0.00	0.00	0.00			
Fe-II	0.14	0.20	0.15	0.12	0.22	0.23	0.12	0.28	0.25	0.07	0.15	0.14	0.19	0.24	0.24			
Mn	0.00	0.00	0.00	0.00	0.00	0.00	0.00	0.00	0.00	0.00	0.00	0.00	0.00	0.00	0.00			
Mg	0.04	0.10	0.07	0.03	0.07	0.10	0.04	0.11	0.11	0.04	0.07	0.05	0.05	0.07	0.05			
Ca	0.00	0.01	0.00	0.00	0.00	0.00	0.00	0.00	0.00	0.00	0.00	0.00	0.00	0.00	0.00			
Na	0.03	0.02	0.04	0.05	0.03	0.02	0.05	0.03	0.02	0.08	0.06	0.07	0.04	0.05	0.06			
K	0.92	0.90	0.92	0.91	0.92	0.86	0.93	0.93	0.96	0.90	0.88	0.88	0.89	0.91	0.88			
Total	7.01	6.99	7.01	7.01	7.00	6.97	7.01	7.05	7.03	7.01	6.99	7.00	6.99	7.00	7.00			

Table C1 Major and Trace element analyses of muscovite fractions and whole rocks

Sample	TE-A3	TE-B1	TE-B3	TE-B4	TE-B5	TE-C1	TE-C2	TE-C3	TE-C4	TE-C5	TE-D1	TE-E1	TE-E2	TE-E3	TE-E4	TE-E5	TE-F1	TE-F2	TE-F3	TE-F4	TE-F5	TE-A0	TE-B0	TE-C0	TE-D0	TE-E0	TE-F0	
Type	Ms	Ms	Ms	Ms	Ms	Ms	Ms	Ms	Ms	Ms	Ms	Ms	Ms	Ms	Ms	Ms	Ms	Ms	Ms	Ms	Ms	Wr	Wr	Wr	Wr	Wr	Wr	
CaO	0.03	0.03	0.03	0.03	0.03	0.04	0.04	0.03	0.03	0.08	0.14	0.06	0.04	0.07	0.05	0.03	0.04	0.07	0.04	0.04	0.51	0.38	0.48	0.65	0.54	0.18		
Na ₂ O	0.60	0.47	0.48	0.48	0.51	0.49	0.45	0.52	0.56	0.51	0.53	0.58	0.55	0.61	0.60	0.64	0.55	0.55	0.61	0.56	0.59	5.50	4.13	4.85	3.89	4.28	2.87	
K ₂ O	10.37	10.67	10.76	10.89	10.80	10.82	10.90	10.80	11.04	14.04	11.17	10.82	10.88	10.72	10.69	10.70	10.96	10.56	11.21	10.82	11.08	2.25	2.96	3.32	2.04	2.56	6.87	
P2O5	0.02	0.02	0.02	0.02	0.02	0.02	0.02	0.02	0.03	0.02	0.03	0.02	0.03	0.02	0.03	0.02	0.02	0.03	0.02	0.03	0.02	0.15	0.12	0.11	0.22	0.10	0.18	
Ba	9.56	78.70	75.45	75.32	76.96	28.09	24.20	26.44	27.35	25.87	55.02	55.07	57.00	44.21	40.14	45.82	56.51	57.50	55.70	59.52	56.42	5.95	65.22	31.31	69.83	53.03	114.51	
Li	67.17	152.60	163.80	169.99	161.38	117.42	88.27	121.34	117.15	119.85	121.47	57.05	14.37	61.03	25.54	60.47	305.11	292.63	317.33	302.88	324.21	16.65	30.05	24.72	24.04	15.88	27.74	
Co	6.33	29.99	21.23	20.39	20.79	8.51	9.08	7.90	7.46	8.07	17.94	10.32	10.41	10.62	10.26	10.49	48.28	21.82	30.64	45.38	37.50	3.28	6.80	2.28	1.73	1.72	26.79	
La	0.09	0.10	0.07	0.10	0.06	0.25	0.29	0.21	0.20	0.26	0.97	0.24	0.24	0.12	0.15	0.16	0.05	0.16	0.08	0.05	0.05	1.14	0.90	2.53	4.97	2.21	1.12	
Ce	0.03	0.06	0.05	0.06	0.08	0.17	0.40	0.09	0.17	0.26	1.84	0.42	0.48	0.24	0.77	0.44	0.26	0.92	0.17	0.12	0.11	2.11	1.86	3.76	11.48	4.83	2.18	
Pr	0.00	0.00	0.00	0.00	0.05	0.02	0.42	-0.02	0.12	0.14	0.41	0.10	0.34	0.16	0.61	0.24	0.10	0.80	0.07	0.13	0.08	0.54	0.66	0.48	1.56	0.71	0.41	
Nd	0.17	0.29	0.00	0.02	0.38	0.15	1.03	0.22	0.45	0.48	1.16	0.44	1.31	0.67	2.23	0.68	0.60	3.22	0.30	0.43	0.38	2.00	2.03	1.54	5.46	2.38	1.39	
Sm	0.02	0.02	0.04	0.00	0.01	0.04	0.07	0.05	0.04	0.05	0.20	0.01	0.06	0.02	0.02	0.03	0.00	0.02	0.00	0.00	0.00	0.22	0.20	0.39	1.59	0.36	0.40	
Eu	0.00	0.01	0.01	0.01	0.01	0.01	0.03	0.01	0.01	0.02	0.02	0.02	0.03	0.01	0.00	0.02	0.01	0.00	0.01	0.00	0.01	0.03	0.11	0.12	0.11	0.15	0.05	
Gd	0.02	0.00	0.00	0.01	0.03	0.03	0.02	0.02	0.01	0.25	0.01	0.03	0.02	0.02	0.01	0.00	0.08	0.02	0.00	0.02	0.20	0.17	0.36	1.70	0.30	0.33		
Tb	0.00	0.00	0.00	0.01	0.00	0.00	0.00	0.00	0.00	0.00	0.04	0.00	0.00	0.00	0.00	0.00	0.00	0.00	0.00	0.00	0.00	0.06	0.03	0.08	0.38	0.06	0.06	
Dy	0.06	0.05	0.06	0.07	0.13	0.09	0.20	0.09	0.11	0.10	0.34	0.09	0.16	0.07	0.27	0.10	0.07	0.15	0.08	0.05	0.05	0.46	0.33	0.58	2.73	0.53	0.53	
Ho	0.00	0.00	0.00	0.01	0.01	0.00	0.00	0.00	0.00	0.00	0.04	0.00	0.00	0.00	0.00	0.01	0.00	0.00	0.00	0.00	0.00	0.06	0.03	0.09	0.50	0.10	0.03	
Er	0.00	0.00	0.00	0.01	0.02	0.01	0.03	0.02	0.01	0.01	0.14	0.01	0.03	0.01	0.02	0.04	0.00	0.00	0.00	0.01	0.00	0.21	0.07	0.33	1.23	0.27	0.04	
Tm	0.00	0.00	0.00	0.00	0.00	0.00	0.00	0.00	0.00	0.00	0.00	0.00	0.00	0.00	0.00	0.00	0.00	0.00	0.00	0.00	0.00	0.00	0.01	0.00	0.03	0.09	0.02	0.00
Yb	0.00	0.00	0.00	0.02	0.01	0.03	0.00	0.01	0.02	0.01	0.08	0.02	0.03	0.02	0.00	0.03	0.00	0.00	0.00	0.00	0.00	0.41	0.10	0.45	1.30	0.39	0.02	
Lu	0.00	0.00	0.00	0.00	0.00	0.01	0.00	0.00	0.00	0.00	0.02	0.00	0.00	0.00	0.00	0.00	0.00	0.00	0.00	0.00	0.00	0.07	0.02	0.08	0.14	0.07	0.00	

Papers and manuscripts

2.3 Paper #3

A combined EBSD– and in–situ $^{40}\text{Ar}/^{39}\text{Ar}$ study of Permian magmatic relic muscovite deformed in upper–greenschist facies Cretaceous shear zones

Eberlei, T., Habler, G., Schneider, D., Grasemann, B.

(2014)

In preparation for submission

A combined EBSD– and in–situ $^{40}\text{Ar}/^{39}\text{Ar}$ study of Permian magmatic relic muscovite deformed in upper–greenschist facies Cretaceous shear zones

^{1,*}Eberlei, T., ¹Habler, G., ³Schneider, D., ²Grasemann, B.

¹Department of Lithospheric Research, University of Vienna, Althanstraße 14, A–1090 Vienna, Austria (* email: tobias.eberlei@univie.ac.at)

²Department of Geodynamics and Sedimentology, University of Vienna, Althanstraße 14, A–1090 Vienna

³Department of Earth Sciences, University of Ottawa, Ottawa, K1N 6N5, Canada

Abstract

Electron Backscatter Diffraction and in–situ $^{40}\text{Ar}/^{39}\text{Ar}$ analyses were performed on Permian magmatic relic muscovite, which were deformed during upper–greenschist facies Cretaceous deformation at 500°C and 5 kbar. The EBSD data imply that the deformation behaviour of muscovite is not only controlled by the relative orientation of crystallographic anisotropies with respect to the kinematic frame, but the Y–axis of shear flow is recognised as the rotation axis for crystal plastic lattice rotation, irrespective of the initial clast orientation. In one grain, the muscovite $[\bar{3}10]$ direction is parallel to the Y–axis, suggesting that the active slip system is (001)[110]. In other grains, deformation is accommodated by dislocations with different burgers vectors. Quartz grain sizes and microstructures and textures from the same samples as the muscovite clasts indicate strain rate differences between protomylonitic and ultramylonitic samples of about 2 orders of magnitude. In–situ $^{40}\text{Ar}/^{39}\text{Ar}$ muscovite ages of a weakly deformed sample range between 160 and 105 Ma yielding a weighted mean age of 126 ± 1 Ma, whereas a mylonite yielded 94 ± 2 Ma with a significantly lower age spread of the single data. The latter is interpreted to reflect the timing of Cretaceous deformation. The data imply, that deformation at 500°C is required for complete resetting of $^{40}\text{Ar}/^{39}\text{Ar}$ ages from large muscovite clasts.

1. Introduction

Muscovite in mylonites commonly forms clasts with specific geometric arrangement (so–called ‘mica–fish’, Lister and Snoke, 1984; ten Grotenhuis et al., 2003). Due to

their strong crystallographic anisotropy, crystal-plastic deformation is typically accommodated by dislocation glide in the (001) plane with burgers vectors $[100]$, $\frac{1}{2}[110]$ and $\frac{1}{2}[\bar{1}\bar{1}0]$ (Meike, 1989; Mares and Kronenberg, 1993). Kinks at large angles to the (001) plane are common related features (Bell et al., 1986). Mares and Kronenberg (1993) experimentally showed, that kinks with kink planes at high angles to (001) form in crystals shortened parallel to (001). In torsion experiments, Misra and Burg (2012) documented kink-formation under conditions of 300–800°C at >50 MPa confining pressures. Another important deformation structure in muscovite are stacking-faults, which may form during growth and deformation of muscovite (Kramar et al., 2003). They are not visible in the optical microscope but have been reported to lower Ar-retentivity of micas (e.g. Kramar et al., 2003). Moreover, the presence of a mantle phase between the clast and the matrix can potentially influence the deformation within a clast by rheological decoupling of the clast from the matrix and thus introducing pressure perturbations and variable shear stresses within the mantled clast (Schmid and Podladchikov, 2005).

Early studies used transmission electron microscopy (TEM) to study sub- μm microstructures and the nature of dislocations and stacking-faults in micas (Bell and Wilson, 1981; Behrmann, 1984; Bell et al., 1986; Meike, 1989; Mares and Kronenberg, 1993). This method, however, is time-consuming, requires complex sample preparation and is either restricted to investigation of very small sample sizes of a few μm (FIB), or does not allow site specific sample preparation. In contrast, electron backscatter diffraction analysis (EBSD) can cover several hundreds of μm sized sample areas at high spatial resolution (50-80 nm), and allows for the combined microstructural and textural analysis of any crystalline material (e.g. Prior et al., 1999). Unfortunately, EBSD analysis of micas has long been considered as problematic, due to difficulties in sample preparation and indexing (e.g. Dempsey et al., 2009; Prior et al., 2009). Bestmann et al. (2011) were able to conduct EBSD analysis of a muscovite crystal in a muscovite-bearing quartzite. These data indicate lattice rotation of a kinked muscovite around the $[\bar{3}10]$ direction, which, in turn, nearly coincided with the Y-axis of shear flow (i.e. the vorticity axis; Bestmann et al., 2011).

Understanding the deformation behaviour of muscovite in strained rocks is crucial for the correct interpretation of $^{40}\text{Ar}/^{39}\text{Ar}$ ages obtained from deformed clasts (e.g. Hames and Cheney, 1997). $^{40}\text{Ar}/^{39}\text{Ar}$ step-heating analysis using multiple grain fractions have

been used to date experimentally and/or naturally recrystallized and deformed micas and constrain the effects of brittle and crystal plastic deformation on the Ar-retentivity of strained sheet silicates (Dunlap and Kronenberg, 2001; Markley et al., 2002; Beltrando et al., 2009; Kula et al., 2010; Cosca et al., 2011; Rosenbaum et al., 2012). However, this approach often results in complex age spectra with significant apparent age variations within a single sample (e.g. Bröcker et al., 2013). Explanations for such data include excess argon or mixing of different mica populations, leading to degassing of multiple Ar reservoirs in a single heating step (Foster and Lister, 2004; Kula et al., 2010). Microstructurally controlled in-situ $^{40}\text{Ar}/^{39}\text{Ar}$ analyses can be applied to better resolve the effects of brittle and crystal plastic deformation on the Ar-retentivity of micas (Reddy et al., 1996; Reddy and Potts, 1999; Kramar et al., 2001; Mulch et al., 2002, 2005; Beltrando et al., 2013).

The aims of this study are: (i) to characterise intragranular deformation-related microstructures and textures of Permian magmatic relic muscovite clasts using EBSD and to discuss their formation; (ii) to present quartz microstructures and textures and to use these for estimating relative strain rate differences between protomylonitic and ultramylonitic Permian meta-pegmatites; and (iii) to present and discuss in-situ $^{40}\text{Ar}/^{39}\text{Ar}$ ages of muscovite clasts from weakly and strongly deformed Permian meta-pegmatites in order to constrain the effects of deformation on $^{40}\text{Ar}/^{39}\text{Ar}$ ages.

1.1. Geological setting and sample material

Permian pegmatites in the Upper-Austroalpine Matsch Unit in Southern Tyrol (Italy) formed during a HT/LP event at c. 263–280 Ma (Habler et al., 2009). The pegmatites and their host rocks were then overprinted by upper-greenschist facies tectonometamorphism in localized zones of high-strain with mainly top-to-west shear kinematics, culminating in P–T conditions of c. 500°C and 5 kbar (Habler et al., 2009). Thöni (1986) dated the Cretaceous deformation in the area at 83 ± 1 Ma by the Rb–Sr thin slab method. The primary magmatic mineral assemblage of the Permian pegmatites is quartz + albite + muscovite \pm garnet \pm K-feldspar \pm apatite and accessory zircon and monazite. The syn-tectonic Cretaceous mineral assemblage contains albite + quartz + muscovite \pm K-feldspar \pm apatite \pm biotite \pm garnet and clinozoisite/allanite. Despite intense deformation, muscovite grains of the primary mineral assemblage were preserved as microstructural relics (Fig. 1).

Two samples of Permian meta-pegmatites from the Upper-Austroalpine Matsch Unit were selected for detailed EBSD analyses of relic muscovite clasts and the surrounding quartz matrix. Sample HM00305 is a protomylonitic Permian meta-pegmatite (North/East: 5170494m/641263m, Altitude: 2596m, UTM Zone 32T, WGS84) with a north-dipping mylonitic foliation (003/80) and an E-W mineral stretching lineation (277/23) that is characterised by mm-sized clasts of albite, muscovite and quartz (Fig. 1a). Sample M1206 is an ultramylonitic Permian meta-pegmatite (North/East: 5170310m/640963m, Altitude: 2620m, UTM Zone 32T, WGS84) with a north-dipping mylonitic foliation (007/36) and an E-W mineral stretching lineation. This sample is characterised by smaller grain-sizes of relic muscovite and albite clasts of <math><500\ \mu\text{m}</math> and the quartzo-feldspathic matrix (Figs 1c and e).

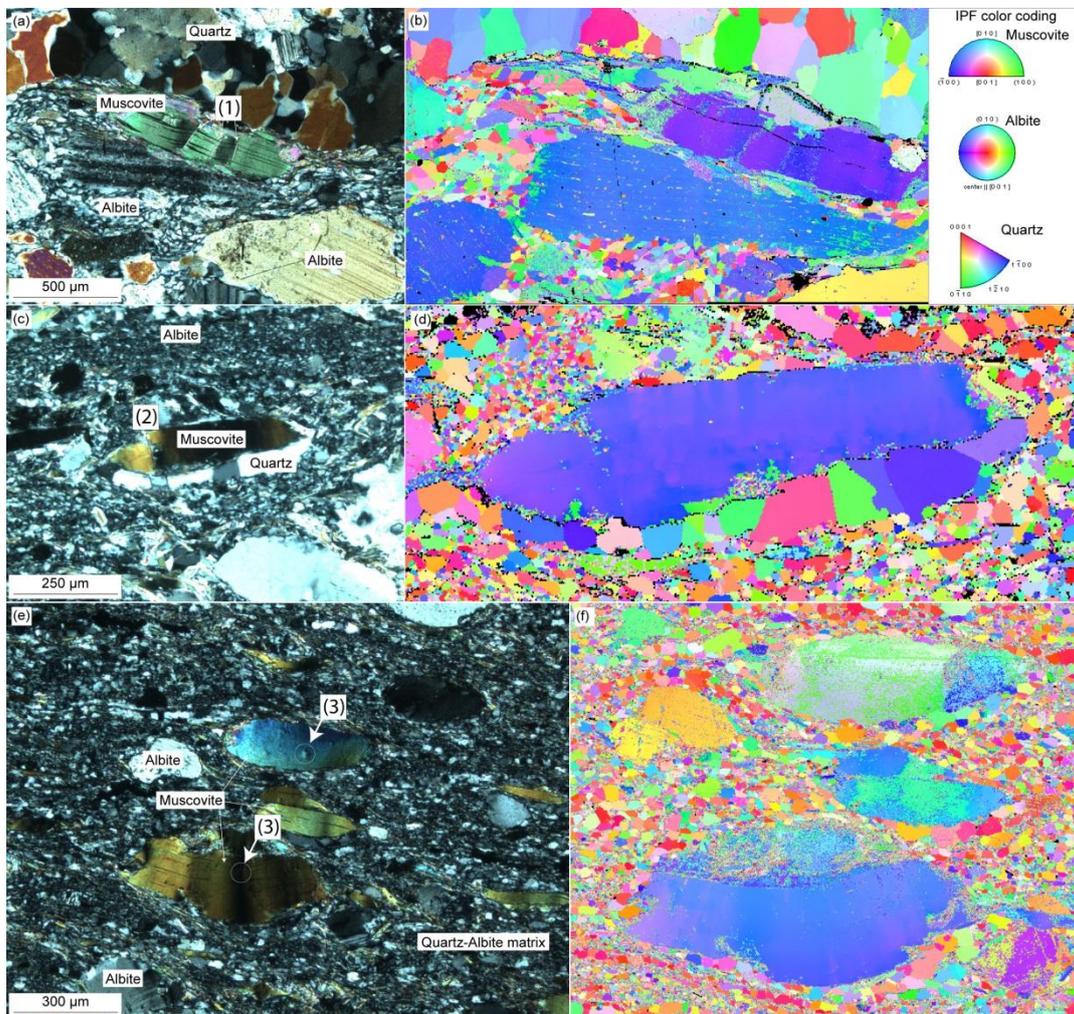


Figure 1 Thin section microphotographs of the relic muscovite clasts in (a–b) the protomylonitic sample HM00305 and (c–f) the ultramylonitic sample M1206. Inverse pole figure maps (IPF) in (b, d, f) correspond to the microphotographs on the left side and use the thin section plane normal as reference direction for the IPF map.

Two separate samples were selected for in-situ $^{40}\text{Ar}/^{39}\text{Ar}$ dating: (i) the weakly deformed Permian meta-pegmatite sample M1217 (North/East: 5170206m/640396m, UTM Zone 32T, WGS84), and (ii) the mylonitic Permian meta-pegmatite sample M1201 (North/East: 5170319m/640984m, UTM Zone 32T, WGS84). These samples were deformed under the same P-T conditions during the Cretaceous with the same kinematics. A short microscope-based description for both samples is given in section 2. For comparison with the Ar-Ar data, a biotite fraction from an undeformed Grt-St-And-two mica schist with presumably Alpine staurolite and chlorite (Sample HM07903; Fig. 2), was analysed by Rb-Sr ID-TIMS.

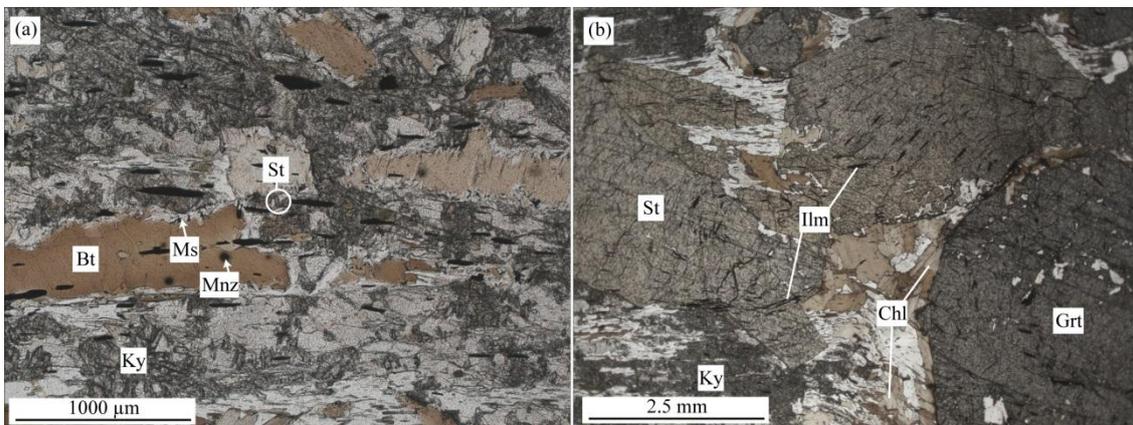


Figure 2 (a-b) Representative microstructures of the Grt-St-And-two mica schist used for dating of biotite as discussed in the text (HM07903).

HM07903 is a coarse grained mica schist (Fig. 2) from the Mastaun Joch area in the OSC, just north of the border to the Matsch Unit. This sample lacks clear evidence for Upper-greenschist facies Cretaceous deformation. However, Variscan garnet grew syn- to post-deformative with respect to D_{n+1} . A foliation in the matrix, defined by aligned ilmite (Ilm), is deflected around the garnet porphyroclasts (D_{n+2} ; Fig. 2b). Large staurolite porphyroblasts (St) grew post-deformative with respect to D_{n+2} . Andalusite porphyroblast that grew post-deformative with respect to D_{n+2} , are almost completely replaced by numerous fine grained kyanite crystals (Ky, Fig. 2a). Biotite porphyroblasts (Bt) commonly have inclusions of monazite (Mnz, Fig. 2a). In contact with the Al_2SiO_5 -phase, biotite broke down to form muscovite (Ms) and occasionally ilmite (Fig. 2a). In this Al-rich environment, small euhedral, presumably Cretaceous, staurolite crystals with lengths of $<50\ \mu\text{m}$ formed (St; Fig. 2a). Presumably Cretaceous chlorite and sometimes tourmaline are found in the matrix (Fig. 2b). The mineralogical observations in this metapelitic schist are in line with published P-T estimates for the Cretaceous event in the Matsch Unit at 500°C and 5 kbar (Habler et al., 2009).

2. Microstructures and Textures

Thin sections used for EBSD analyses were cut parallel to the mylonitic lineation and perpendicular to the foliation. Thus, the Y-axis of shear flow is perpendicular to the sample surface and hence in the centre of the pole figures presented in Figs 4–5 and 7. Quartz microstructures and textures from matrix domains hosting the Ms clasts are presented within each corresponding subsection. Additionally, short descriptions of the samples M1217 and M1201, used for in-situ $^{40}\text{Ar}/^{39}\text{Ar}$ analysis, are given below.

Electron backscatter diffraction (EBSD)

EBSD analyses were performed on a FEITM Quanta 3D FEG instrument at the Faculty of Geosciences, Geography and Astronomy at the University of Vienna. The system is equipped with a field-emission electron source and an EDAXTM Digiview IV EBSD camera. Polished thin sections were prepared by first mechanical and then mechano-chemical polishing using a colloidal silica suspension with a pH of 9.2–10 for the final preparation step. Electrical conductivity of the samples was established by very thin carbon coating under high vacuum conditions ($<10^{-5}$ mbar) using a single carbon thread. For the EBSD analyses, the samples were tilted to 70° at a working distance of 12 mm for sample HM00305 and 14 mm for sample M1206. Beam settings were at an acceleration voltage of 15 KeV and a beam current of 4 nA in analytical mode. The OIMTM software v5.3.1 for HM00305 and v6.2 for M1206 were used for data collection and processing. EBSD crystallographic orientation mapping was performed by beam scanning with step sizes varying from 1 to 1.5 μm . A 4x4 binning of the EBSD camera resolution was used. General parameters of the Hough settings for indexing 3–14 Hough peaks were a Theta step sizes of 1° , a binned pattern size of 160, a minimum peak distance of 10 pixels in Hough space and applying 9x9 convolution mask. The datasets were cleaned using the “Grain CI (=confidence index) Standardization” and “Neighbour Orientation Correlation (NOC)” (NOC clean-up level 2) cleanup routines of the OIMTM Analysis software. EBSD data provide microstructural information on spatial arrangement of grains, quantitative grain-size and -distribution, the 2D geometry of grain boundaries and the full crystallographic orientation of crystalline material. Crystallographic orientation data are primarily presented as pole figures, whereas microstructures are shown as greyscale EBSD pattern quality maps (IQ) containing additional information on misorientation angles between grains and subgrains. Inverse

pole figure maps (IPF) plotting crystal directions with respect to the thin section normal direction are shown in Figs 1b,d,f.

2.1. Microstructures of sample M1217

Sample M1217 is a macroscopically weakly deformed Permian meta-pegmatite. However, mm-sized muscovite clasts in this are strongly folded and show kinks with kink band widths of several 100 μm (Fig. 3a). Microkinks with small lattice misorientations and sizes of <20–30 μm are also present, as displayed by undulose extinction ((1) in Fig. 3a). Additionally, a fine grained (<50 μm) muscovite generation ((2) in Fig. 3b) is associated with strong lattice deformation along kink axial planes. Furthermore, muscovite clasts also show evidence for grain-scale cracking at high angles to muscovite (001) ((3) in Fig. 3b) and numerous, μm -sized acicular inclusions of Fe-oxides and -sulphides with a clear shape preferred orientation parallel to muscovite (001) ((4) in Fig. 3b).

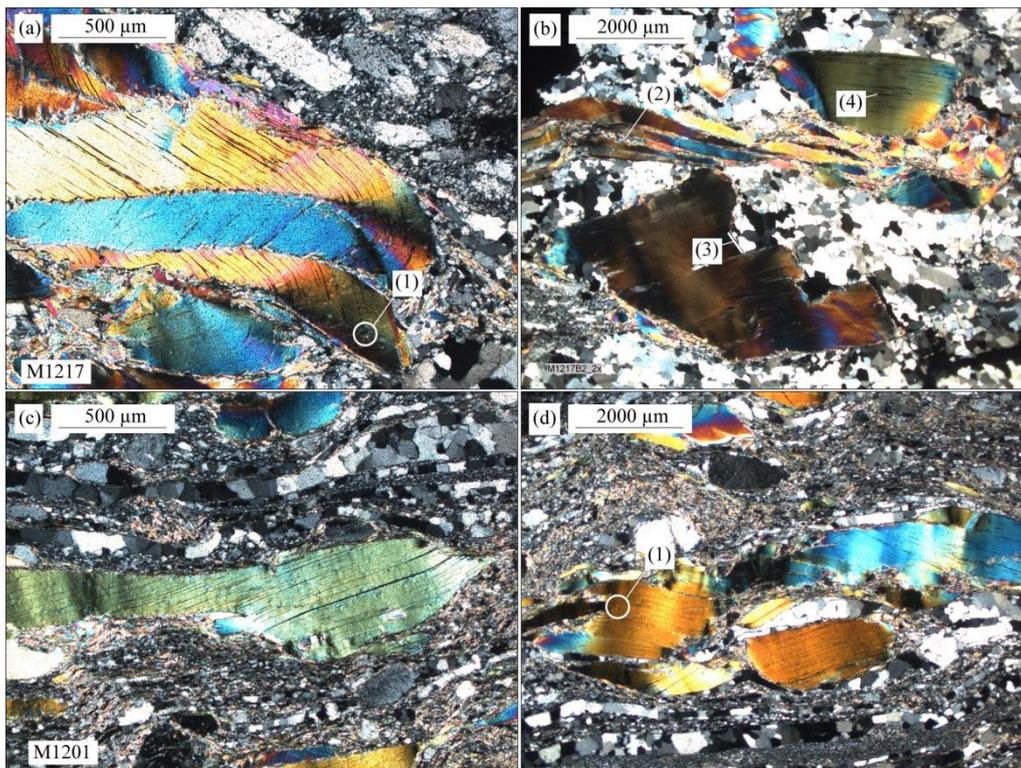


Figure 3 (a–b) Representative microstructures of the macroscopically weakly deformed Permian meta-pegmatite M1217 and (c–d) the mylonitic sample M1201, used for in-situ $^{40}\text{Ar}/^{39}\text{Ar}$ analysis.

2.2. Microstructures and textures of protomylonite HM00305

The muscovite clast in mylonite sample HM00305 is about 700 μm in length with an aspect ratio of ~ 4 , kinked with kink bands tracing at large angles relative to traces of

muscovite (001) ((1) in Fig. 1a and Fig. 4a) and surrounded by a rim of fine-grained (<100 μm sized) muscovite. The muscovite clast is located between an albite layer consisting of a coarse grained and a fine grained fraction below and a monomineralic quartz layer above (Figs 1a and 4a). A misorientation profile from point A to point B parallel to the traces of the muscovite (001) planes over a length of *c.* 600 μm shows lattice misorientation of up to 30° associated with the kinks (Fig. 4). Additionally, several peaks in the vicinity of the kink bands are caused by misindexing, which is typically concentrated at these sites (Figs 1b and 4c). Associated with kinks, the muscovite lattice rotates around the Y-axis of shear flow, which is the direction perpendicular to the sample surface (Fig. 4b; cf. Bestmann et al., 2011).

The monomineralic quartz layer above the relic muscovite clast is characterised by grain sizes of >100 μm and subgrains at 70–100 μm size (Fig. 4e). Quartz shows twinning according to the dauphiné law. Only a few fine grained quartz grains (<40 μm) occur in the recrystallised albite matrix below the muscovite clast.

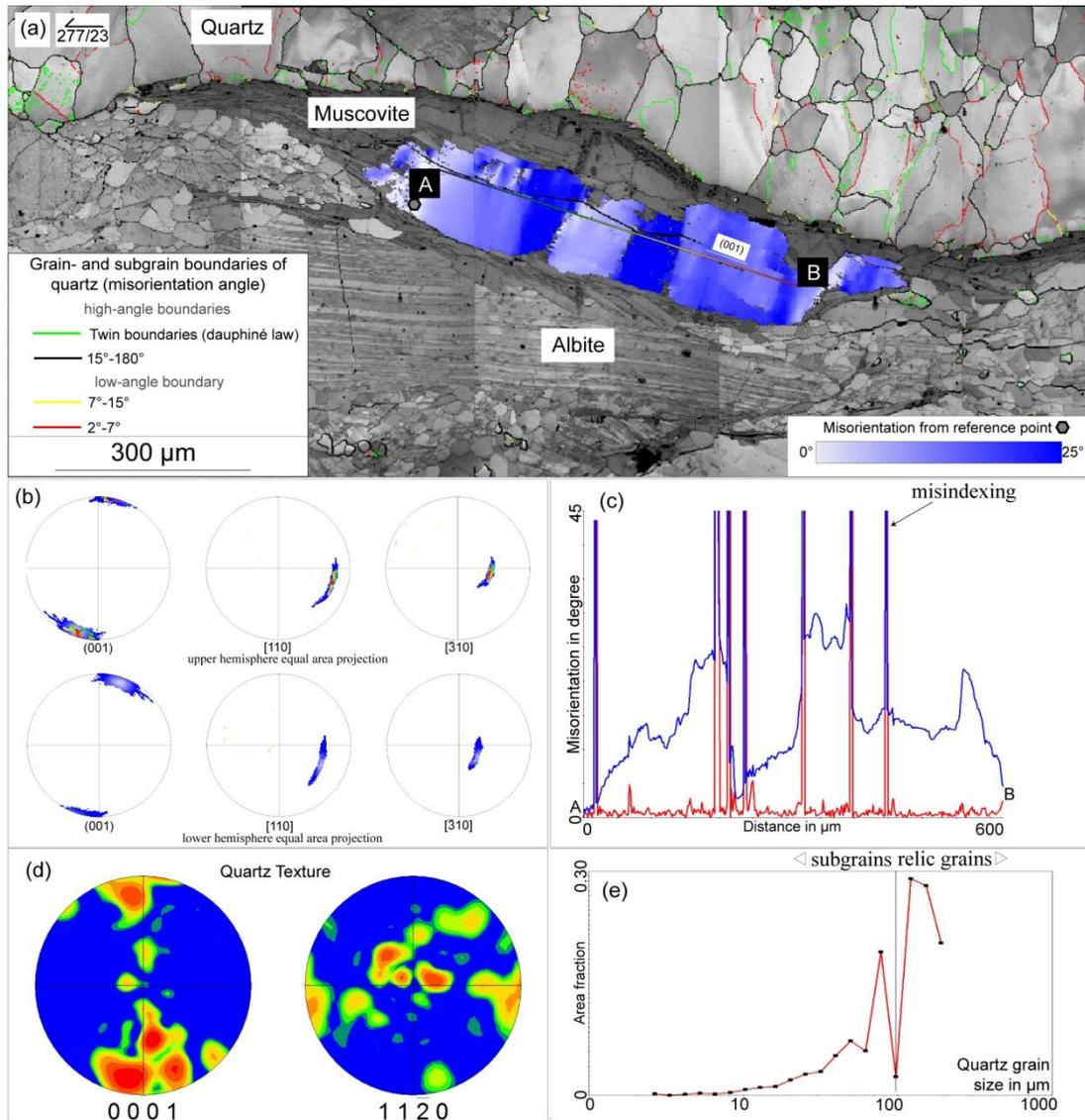


Figure 4 (a) IQ map of the kinked relic muscovite clast and hosting Qtz-Ab-matrix from sample HM00305. (Sub)grain boundary traces of Qtz are color-coded according to misorientation angles across the boundaries. Blue–white gradient highlighting muscovite gives misorientation relative to the reference point. (b) Lattice rotation of the muscovite grain along the misorientation profile A-B with rainbow color highlighting in upper and lower hemisphere equal area projections. Blue–white highlighting as in Fig a). (c) Misorientation profile of muscovite along line A-B in Fig. (a). (d–e) Quartz textures and grain size distribution within the monomineralic quartz layer. Note the difference in the quartz texture compared to sample M1206 (Figs 5 and 7).

2.3. Microstructures and textures of mylonitic and ultramylonitic samples

2.3.1. Mylonitic sample M1201

Sample M1201 is characterised by an intense north–dipping mylonitic foliation (359/42) and an E–W trending mineral stretching lineation. Relic muscovite clasts are smaller, compared to the weakly deformed sample M1217 (Figs 3a–b). They show undulose extinction, folds and cracks (Figs 3c–d). Small microkinks with sizes of <20–30 μm and small lattice misorientations are present ((1) in Fig. 3d). Small muscovite grains (<50 μm) are associated with strong lattice deformation of large clasts and,

together with alternating layers of quartz and feldspar, they define the pronounced mylonitic foliation in this sample.

2.3.2. Ultramylonitic sample M1206

2.3.2.1. Clast I

Muscovite clasts in sample M1206 occur as weakly bent clasts with several 100 μm in length (Figs 1,5,7). The clast shown in Fig. 5a is characterised by several small-scale microkinks ((3) in Fig. 1e and (1) in Fig. 5a) with traces of kink planes perpendicular to the traces of the muscovite (001) plane. These small intragranular kinks are characterised by a paired occurrence of parallel kink planes, with kink lengths of $<30 \mu\text{m}$ and small misorientations of $<6^\circ$ (Figs 5b and d). The kinks are associated with (001)-parallel cracks or void space, filled with secondary phases, such as ultra fine-grained muscovite (Fig. 6). The misorientation profile A-B is associated with a rather continuous crystal lattice rotation up to 20° with maximum point to point misorientations of less than 0.5° (Figs 5a and d). Furthermore, the data indicate a crystal lattice rotation by the muscovite $[\bar{3}10]$ direction (Fig. 5c), which is in this case perpendicular to the sample surface and thus parallel to the Y-axis of shear flow.

Quartz in the matrix of the ultramylonitic sample M1206 has a smaller grain size ($\sim 50\text{--}60 \mu\text{m}$, Fig. 5f) than recrystallised grains in the protomylonitic sample HM00305 (cf. Fig. 4e). However, the Qtz grain size in M1206 is still significantly larger than the grain size of matrix feldspar (Fig. 5a). Quartz grains show straight grain boundary segments and 120° dihedral angles (e.g. (2) in Fig. 5a), suggesting microstructural equilibrium. Differences in the quartz textures between sample HM00305 and M1206 (cf. Figs. 4d and 5e) point to the activity of different slip systems.

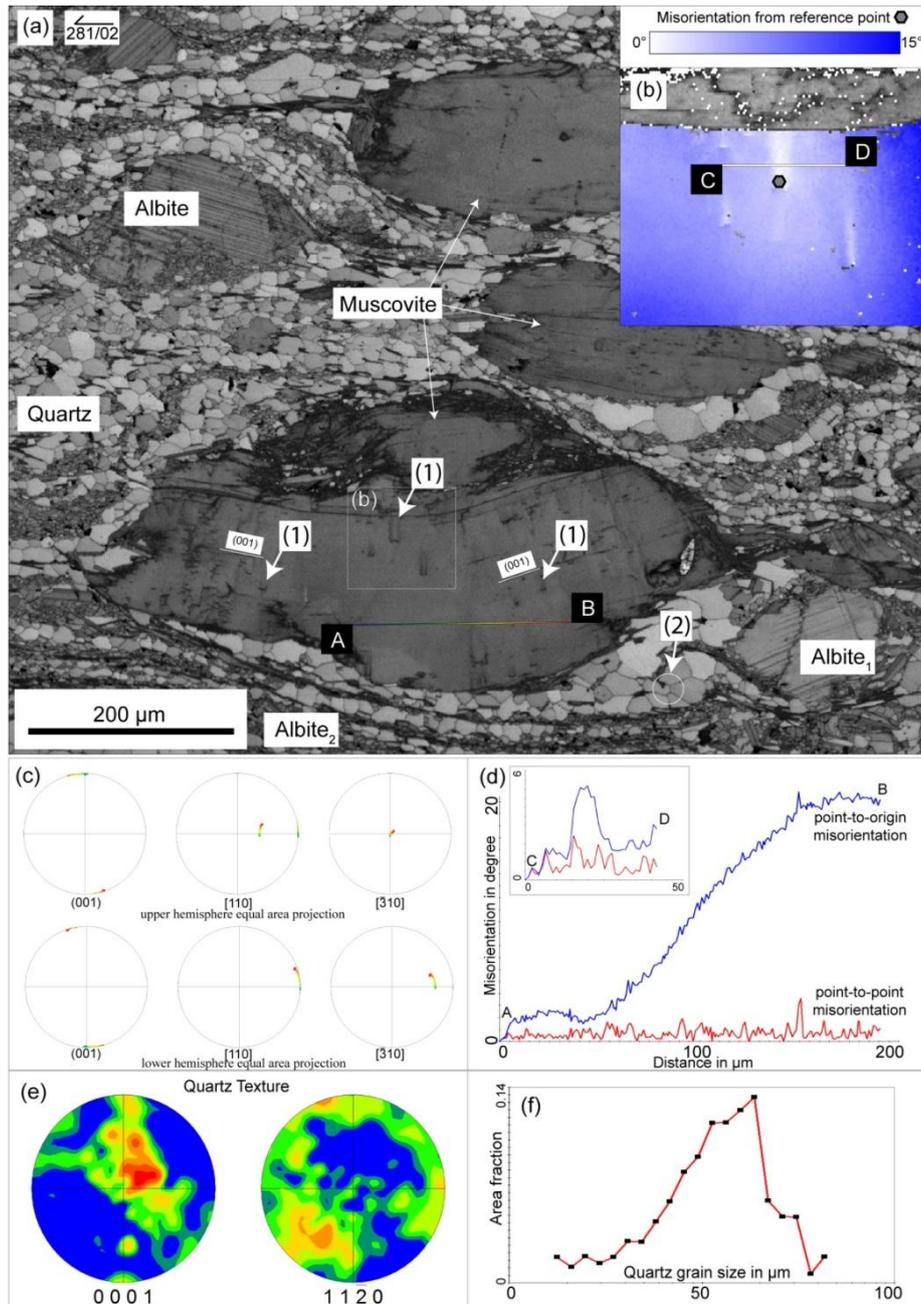


Figure 5 (a) IQ map of muscovite clasts in the quartz–feldspathic matrix of the ultramylonitic sample M1206. Numbers in round brackets highlight microstructural features discussed in the text. (b) Detail of (a) highlighting the lattice rotation associated with small kinks. (c) Muscovite lattice rotation along profile A–B shown in (a). (d) Misorientation profile A–B shown in (a) and C–D shown in (b). (e) Quartz texture and (f) quartz grain size distribution.

2.3.2.2. Clast II

Another muscovite clast of sample M1206 shown in Figs 1c and 7a shows a crack at a large angle relative to the (001) plane ((2) in Fig. 1c). The misorientation profile A–B shows intragrain lattice misorientation of up to 20° (Fig. 7c). The lattice rotation within this clast seems to focus around an axis perpendicular to the sample surface and hence parallel to the Y–axis of shear flow (Fig. 7b).

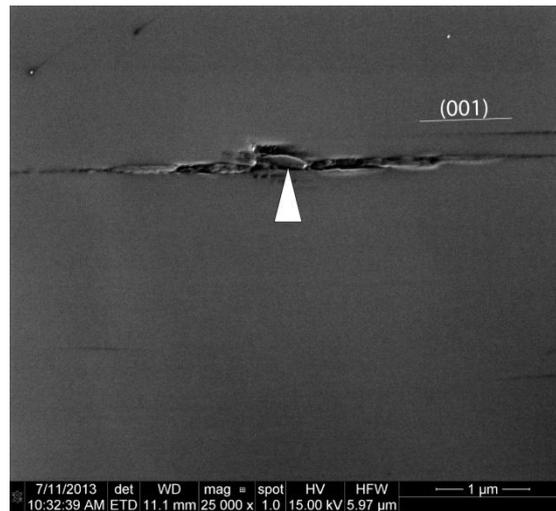


Figure 6 SE image of a (001)-parallel void associated with a small kink in a relic muscovite clast (cf. (1) in Fig. 5a) with secondary ultra fine grained muscovite (head of white arrow).

Quartz textures are largely similar to those presented in Fig. 5e. Grain sizes are at ~ 50 μm (Fig. 7e) whereas Qtz grains in the mylonitic Qtz–Ab–matrix, intercalated with very fine grained feldspar aggregates and fine grained muscovite (Fig. 7a), are smaller than in monomineralic layers. Still straight grain boundary segments and nearly 120° dihedral angles are characteristic for Qtz in this sample ((1) in Fig. 7a).

3. Geochronology

3.1. In-situ $^{40}\text{Ar}/^{39}\text{Ar}$ data

Rock slabs from sample M1217 and M1201 were prepared by adhesion to a glass slide with cyanoacrylate glue (“superglue”), and ground to 80 μm thickness before polishing. After imaging, the polished slabs were removed from the glass slides by soaking in acetone, then cut into 5 mm squares to isolate the micas of interest, and washed in acetone, methanol and water before packing into foil packets for irradiation. Samples were irradiated at the McMaster University Nuclear Reactor (Hamilton, Canada) for 120 hours. Cadmium shielding was used and the samples were held in position 8D. Neutron flux was monitored using biotite mineral standard GA1550 which has an age of 98.79 ± 0.54 Ma (Renne et al., 1998).

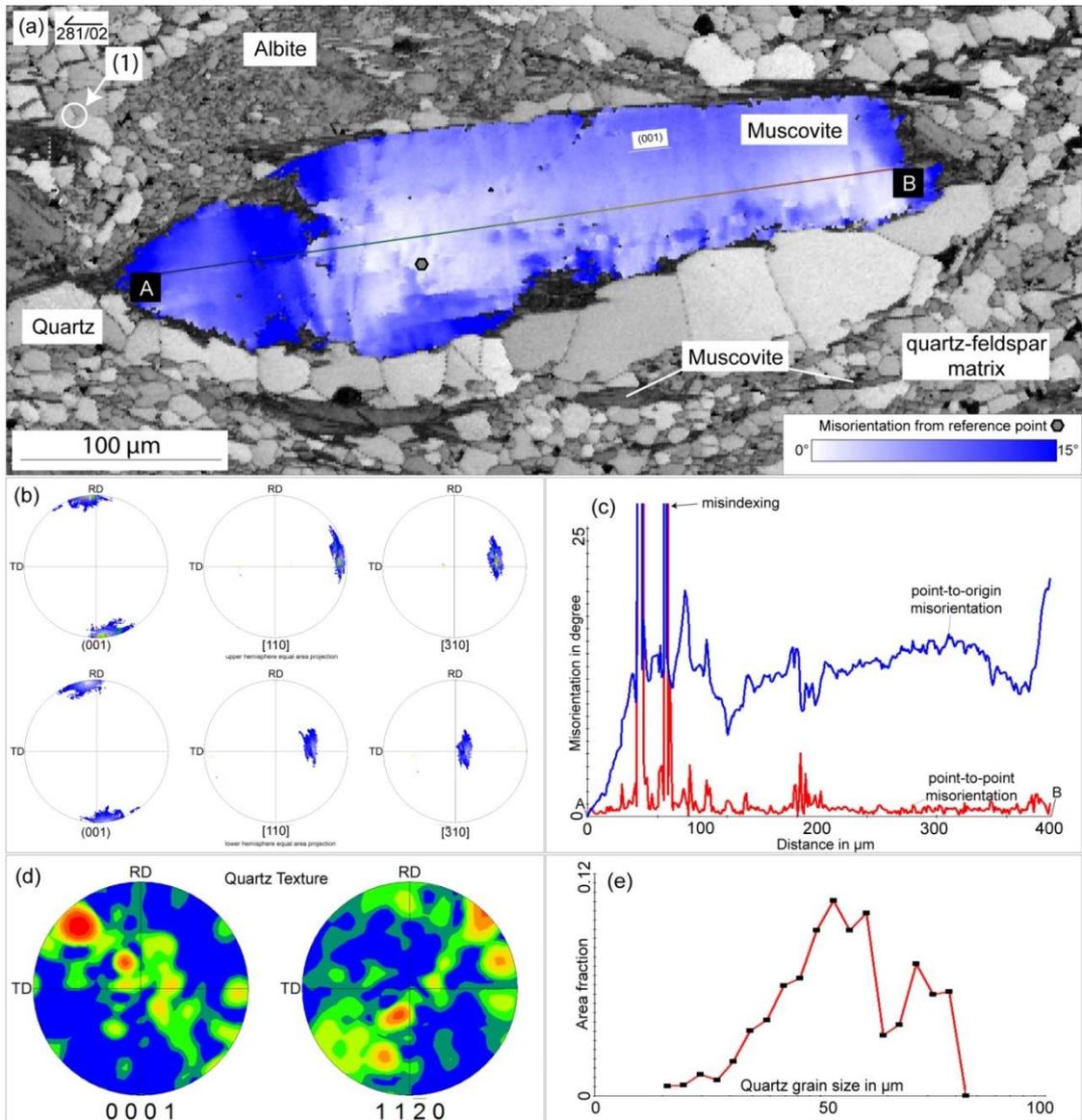


Figure 7 (a) IQ map of a muscovite clast in ultramylonite sample M1206 Number in round bracket highlights microstructural feature discussed in the text. (b) Crystallographic orientations of muscovite plotted as equal area projections and highlighted as in (a). (c) Misorientation profile A-B. (d) Quartz texture and (e) quartz grain size distribution.

Standards were packed for irradiation, either side of the unknown samples, and analysed using the single grain fusion method via a 1059 nm CSI fibre laser and a MAP215–50 mass spectrometer at The Open University $^{40}\text{Ar}/^{39}\text{Ar}$ Laboratory (Milton Keynes, UK). The J-values were then calculated by linear extrapolation between the two measured J-values. Results were corrected for ^{37}Ar decay, and neutron-induced interference reactions using the correction factors: $(^{40}\text{Ar}/^{39}\text{Ar})_{\text{K}} = 0.0085 \pm 0.0000425$, $(^{39}\text{Ar}/^{37}\text{Ar})_{\text{Ca}} = 0.00065 \pm 0.00000325$, and $(^{36}\text{Ar}/^{37}\text{Ar})_{\text{Ca}} = 0.000265 \pm 0.000001325$, based on analyses of Ca and K salts. The irradiated samples were loaded into an ultra-high vacuum system and mounted on a New Wave Research UP-213 stage.

The CSI fibre laser was focused into the sample chamber and was used to spot date the crystals in the polished section. After passing through a liquid nitrogen trap, extracted gases were cleaned for five minutes using two SAES AP–10 getters running at 450°C and room temperature, following which the gasses were let into a MAP 215–50 mass spectrometer for measurement, the mass discrimination value was measured at 283 for $^{40}\text{Ar}/^{36}\text{Ar}$. System blanks were measured before and after every one or two sample analyses. Gas clean-up and inlet is fully automated, with measurements of ^{40}Ar , ^{39}Ar , ^{38}Ar , ^{37}Ar and ^{36}Ar , each for ten scans, and the final measurements are extrapolations back to the inlet time.

The system blanks measured before and after every one or two sample analysis were subtracted from the raw sample data. All data corrections were carried out, and plotted, using an Excel macro and ages were calculated using Isoplot (Ludwig, 2003). $^{40}\text{Ar}/^{39}\text{Ar}$ data are reported with 1σ errors and the ages with 2σ errors.

Table 1 In-situ UV–laser $^{40}\text{Ar}/^{39}\text{Ar}$ data of white micas from the Upper–Austroalpine Matsch Unit, Southern Tyrol

Sample	J-value	$^{40}\text{Ar} \pm 1\sigma$	$^{39}\text{Ar} \pm 1\sigma$	$^{38}\text{Ar} \pm 1\sigma$	$^{37}\text{Ar} \pm 1\sigma$	$^{36}\text{Ar} \pm 1\sigma$	$^{40}\text{Ar}/^{39}\text{Ar} \pm 1\sigma$	$^{40}\text{Ar}/^{39}\text{Ar}$ age (Ma) $\pm 2\sigma$
Sample M1201 nylonitic Permian meta-pegmatite								
Spot 1	$J = 0.006811567 \pm 0.0000340578$	11.48738 0.01292	1.17696 0.00485	0.01371 0.00036	0.02778 0.00091	0.00060 0.00005	9.60965 0.04307	114.38 0.74
Spot 2		3.27333 0.00511	0.33579 0.00249	0.00405 0.00009	0.00069 0.00091	0.00011 0.00003	9.65398 0.07852	114.90 1.06
Spot 3		3.89155 0.01137	0.41637 0.00223	0.00534 0.00021	0.00521 0.00091	0.00019 0.00003	9.21467 0.06091	109.82 0.88
Spot 4		2.58167 0.00458	0.31254 0.00116	0.00395 0.00017	0.03196 0.00091	0.00026 0.00002	8.01565 0.03965	95.91 0.66
Spot 5		2.39540 0.00442	0.29650 0.00185	0.00366 0.00011	0.01973 0.00091	0.00014 0.00003	7.93750 0.06085	95.00 0.85
Spot 6		3.79149 0.00418	0.48314 0.00241	0.00636 0.00017	0.05726 0.00091	0.00021 0.00003	7.71796 0.04408	92.43 0.68
Spot 7		1.04509 0.00263	0.13629 0.00103	0.00169 0.00011	0.02635 0.00091	0.00006 0.00002	7.53787 0.07798	90.33 1.01
Spot 8		0.84859 0.00123	0.10062 0.00080	0.00115 0.00012	0.01221 0.00091	0.00014 0.00002	8.01130 0.07856	95.86 1.03
Spot 9		3.41268 0.00485	0.41739 0.00239	0.00560 0.00013	0.01939 0.00091	0.00047 0.00003	7.84209 0.05164	93.88 0.76
Spot 10		3.22400 0.00520	0.41744 0.00174	0.00522 0.00019	0.00957 0.00091	0.00016 0.00003	7.60680 0.04092	91.14 0.65
Spot 11		2.08590 0.00238	0.25977 0.00190	0.00293 0.00015	0.01707 0.00134	0.00015 0.00003	7.85854 0.07023	94.07 0.94
Spot 12		1.40925 0.00201	0.18453 0.00172	0.00228 0.00007	0.00384 0.00135	0.00005 0.00003	7.55044 0.08253	90.48 1.06
Spot 13		2.32727 0.00882	0.28529 0.00172	0.00284 0.00015	0.00000 0.00135	0.00005 0.00003	8.11070 0.03091	97.01 0.59
Spot 14		2.51839 0.00321	0.31269 0.00252	0.00368 0.00017	0.01249 0.00135	0.00007 0.00003	7.98602 0.06979	95.56 0.94
Spot 15		1.24378 0.00445	0.14482 0.00113	0.00179 0.00011	0.00577 0.00135	0.00002 0.00003	8.54011 0.09064	102.01 1.16
Sample M1217 weakly deformed Permian meta-pegmatite								
Spot 1	$J = 0.00693821 \pm 0.000345191$	4.88423 0.01158	0.36395 0.00242	0.00422 0.00017	0.00022 0.00035	0.00007 0.00005	13.36368 0.10131	159.21 1.38
Spot 2		5.41476 0.00415	0.42529 0.00112	0.00497 0.00017	-0.00195 0.00035	0.00075 0.00005	12.21102 0.05047	146.02 0.91
Spot 3		4.66910 0.00929	0.42130 0.00254	0.00499 0.00025	-0.00012 0.00099	0.00025 0.00003	10.90949 0.07302	131.00 1.06
Spot 4		0.31224 0.00102	0.02667 0.00053	0.00031 0.00008	0.00010 0.00099	0.00008 0.00001	10.85917 0.27423	130.42 3.24
Spot 6		1.12763 0.00245	0.07799 0.00036	0.00118 0.00013	0.00054 0.00099	0.00103 0.00004	10.56939 0.16740	127.06 2.04
Spot 7		0.54600 0.00218	0.02741 0.00053	0.00046 0.00006	0.00120 0.00099	0.00070 0.00003	12.41176 0.42733	148.32 4.95
Spot 8		0.21372 0.00127	0.02003 0.00045	0.00015 0.00006	-0.00034 0.00099	0.00010 0.00002	9.24313 0.40017	111.60 4.72
Spot 9		6.90920 0.00623	0.65234 0.00244	0.00743 0.00016	0.00010 0.00099	0.00051 0.00006	10.36194 0.04856	124.65 0.83
Spot 10		3.37139 0.00283	0.26758 0.00172	0.00314 0.00008	-0.00256 0.00099	0.00003 0.00002	12.56926 0.08519	150.13 1.21
Spot 11		5.62741 0.00922	0.47898 0.00297	0.00556 0.00012	-0.00034 0.00099	0.00007 0.00003	11.70743 0.07762	140.22 1.12
Spot 12		1.28940 0.00241	0.10333 0.00071	0.00147 0.00010	0.00187 0.00099	0.00002 0.00002	12.43261 0.10960	148.56 1.45
Spot 13		0.72022 0.00283	0.06065 0.00046	0.00059 0.00010	-0.00034 0.00099	0.00001 0.00003	11.85947 0.18585	141.97 2.25
Spot 14		5.61636 0.00513	0.52765 0.00288	0.00633 0.00020	0.00049 0.00065	0.00059 0.00004	10.31534 0.06151	124.11 0.93
Spot 15		1.78072 0.00390	0.16719 0.00123	0.00188 0.00010	0.00094 0.00065	0.00003 0.00002	10.60363 0.09032	127.46 1.22
Spot 16		2.88622 0.00432	0.25536 0.00163	0.00280 0.00012	-0.00064 0.00065	0.00043 0.00003	10.80812 0.07994	129.83 1.12
Spot 17		2.81104 0.00951	0.08594 0.00068	0.00102 0.00010	0.00071 0.00066	0.00024 0.00005	31.89603 0.32722	359.04 3.72
Spot 18		4.40887 0.00750	0.41626 0.00203	0.00474 0.00023	-0.00041 0.00066	0.00016 0.00004	10.47998 0.06148	126.02 0.94
Spot 19		0.30719 0.00182	0.01310 0.00032	0.00011 0.00005	-0.00064 0.00066	0.00002 0.00003	23.05448 0.91661	266.46 9.93
Spot 20		0.43651 0.00144	0.04954 0.00077	0.00063 0.00008	0.00094 0.00066	0.00000 0.00002	8.83041 0.19177	106.76 2.31
Spot 21		3.75082 0.00889	0.40532 0.00246	0.00497 0.00017	0.00071 0.00066	0.00010 0.00002	9.18337 0.06205	110.90 0.90
Spot 22		3.47603 0.00781	0.36763 0.00290	0.00439 0.00021	-0.00041 0.00066	0.00006 0.00002	9.40927 0.07912	113.54 1.08
Spot 23		3.06430 0.00438	0.29676 0.00259	0.00306 0.00012	0.00004 0.00066	0.00001 0.00003	10.31875 0.09633	124.15 1.27
Spot 24		4.65722 0.00569	0.40393 0.00403	0.00496 0.00016	0.00049 0.00066	0.00004 0.00002	11.50294 0.11685	137.86 1.50

Each sample yielded a range of ages (Table 1). Isotopes ^{38}Ar produced from Cl and ^{37}Ar from Ca can both be useful monitors of intergrowths of biotite and intergrowths of chlorite and contamination with calcite, respectively. Measured concentrations of ^{38}Ar and ^{37}Ar were very low and generally showed no correlation with age within a sample (Figure A.1 in the Appendix), but M1201, the younger sample, yielded a larger range of $^{37}\text{Ar}/^{39}\text{Ar}$ (Ca/K) values.

Sample M1201 yielded single spot ages between 114.9 ± 1.1 Ma and 90.3 ± 1.0 Ma with no discernable correlation between structural position and age. The weighted average $^{40}\text{Ar}/^{39}\text{Ar}$ age for the eleven youngest spot analyses is 94 ± 2 Ma (MSWD: 9.0). Of that population, there is a noticeable smaller population (Fig. 8) within error at 91 ± 3 Ma (MSWD: 0.3). Although there is some scatter of $^{37}\text{Ar}/^{39}\text{Ar}$ values, used as a proxy for Ca contamination, ages of the spots with higher ^{37}Ar were indistinguishable from those with negligible ^{37}Ar . Notably, the older population at c. 115 Ma overlaps with the youngest population of sample M1217.

Sample M1217 yielded single spot ages older than M1201, between 106.8 ± 2.3 Ma and 359 ± 3.7 Ma. The weighted average $^{40}\text{Ar}/^{39}\text{Ar}$ age for the sixteen analyses that make up the bulk of the data is 133 ± 5 Ma (MSWD: 62; Fig. 8). The dominant age population, however, is 126 ± 1 Ma (MSWD: 3.7). The four youngest ages not included in the c. 133 Ma age population, which define the youngest population in both diagrams, yields a weighted average age of 112 ± 1 Ma (MSWD: 2.7).

3.2. Biotite–Whole rock Rb/Sr ID–TIMS analysis

Biotite with a primary grain size of 160–450 μm , from an undeformed Grt–St–And–two mica schist (Sample HM07903) with local growth of presumably Cretaceous staurolite, chlorite, ilmenite, muscovite and kyanite, was separated applying standard procedures including a jaw crusher, a rolling mill, sieving in ethanol and magnetic purification on a Frantz isodynamic magnet separator. For isotope dilution analysis, c. 100 mg of the separate was weighed into a Savillex® screw top beaker, mixed with a ^{87}Rb – ^{84}Sr spike and dissolved in a 4:1 HF/HNO₃ mixture on a hot plate at 110°C for 2 weeks. Rb and Sr were extracted applying standard cation exchange techniques. Sr and Rb isotope ratios were measured in different faraday cups on a FINNIGAN® Triton multicollector thermal ionisation mass spectrometer at the University of Vienna. Within–run mass–dependent Sr isotope fractionation was corrected for with $^{86}\text{Sr}/^{88}\text{Sr}=0.1194$. The $^{87}\text{Sr}/^{86}\text{Sr}$ value of the NBS standard SRM 987 was 0.710269 ± 4 (2σ , $n = 17$). Total procedural blanks of Rb and Sr were consistently below 0.03 ng. By default, a 1% relative error is assigned to the $^{87}\text{Rb}/^{86}\text{Sr}$ ratio. All other errors are quoted on the 2σ level (95% confidence). The age was calculated using a decay constant of $1.42 \cdot 10^{-11} \text{ a}^{-1}$ (Steiger and Jäger, 1977). The results are shown in Table 2. The undeformed biotite from HM07903 is characterised by high Rb and low Sr contents and a $^{87}\text{Sr}/^{86}\text{Sr}$ ratio of 1.57 (Table 2). The corresponding biotite–whole rock Rb–Sr age is 126.6 ± 1.3 Ma. This

is in line with Lower Cretaceous ages obtained for samples from the study area by Haas (1985).

Table 2 Rb/Sr analytical data for biotite (TE-G1) and the corresponding Grt–St–And–two mica schist whole rock (TE-G0)

Sample No.	Material	Rb [ppm]	Sr [ppm]	$^{87}\text{Rb}/^{86}\text{Sr}$	1% error on $^{87}\text{Rb}/^{86}\text{Sr}$	$^{87}\text{Sr}/^{86}\text{Sr}$ with 2 σ error	Age (wr-Ms) with 2 σ error
Metapelite							
HM07903							
TE-G0	whole-rock	164.348	99.101	4.816	0.048	0.743630 \pm 4	
TE-G1	Bt 160-450 μm	595.926	4.033	463.678	4.637	1.569538 \pm 10	126.6 \pm 1.3

4. Discussion

4.1. Crystal plastic deformation of muscovite

Due to the anisotropic crystal structure and the weak K–O interlayer bonding in mica, there is only one major slip plane (001). Differences in the deformation behaviour between different micas arise from the slight distortion of the hexagonal rings in dioctahedral micas compared to the relatively undistorted nature of these rings in trioctahedral micas (Bailey, 1984). The distorted nature of the sheets in dioctahedral muscovite favors screw dislocations with dislocation lines and Burgers vectors oriented parallel to [110] (Meike, 1989). The dominant slip system in 1M₁ muscovite is (001)[110]. Due to alternate layering and 30° rotation of the layers in 2M₁ muscovite, the direction of [110] in one layer is equivalent to the [100] direction in the next layer (Meike, 1989).

On the other hand, assuming dislocations of the (001)[110] slip system having been active in our samples associated with a rotation axis parallel to muscovite $[\bar{3}10]$ (Fig. 5c) lying in the slip plane (001) perpendicular to [110] would be consistent with an edge character of these dislocations. However, the $[\bar{3}10]$ in this case is also parallel to the Y–axis of shear flow, which represents the rotation axis in clasts with a different $[\bar{3}10]$ orientation (Figs 4 and 7). For the latter grains, dislocations with one or more burgers vectors different from the one mentioned above are required to accommodate deformation. Except for the orientation of the (001) plane, intracrystalline crystal plastic deformation of muscovite is not controlled by the relative orientation of the crystallographic anisotropies with respect to the kinematic frame. Instead, the Y–axis of flow seems to be the rotation axis for intracrystalline crystal plastic deformation, irrespective of the initial clast orientation with respect to the kinematic frame (Bestmann et al., 2011).

Schmid and Podladchikov (2005) have modeled the effect of a mantle phase on the intracrystalline pressure perturbations and shear stresses within the mantled clast. In the case of the more strongly deformed clast in Fig. 4a, the mantle around this clast is represented by clast-enveloping fine grained muscovite (<100 μm). However, in this case, the intensity of intragrain deformation could also be related to the presence of a neighboring albite clast, which is supposed to be relatively rigid compared to the Qtz layer on the other side of the muscovite clast (Figs 1a and 4a).

4.2. Microkink formation

The small kinks, termed 'microkinks', typically occur as pairs with kink plane traces oriented perpendicular to the traces of the muscovite (001) plane. Microkinks are associated with small lattice rotations of less than 6° (e.g. (1) in Fig. 5a and Figs 5b and 6). The nucleation site of the microkinks may show a void space filled with secondary phases (Fig. 6). One or a combination of the following two scenarios for the formation of these microkinks are possible: (i) (Ultra)fine-grained mineral phases grew within the cleavages of muscovite, leading to local stress concentrations during intracrystalline (001)-parallel slip and the nucleation of kinks at inclusion sites; or (ii) the microkinks and associated slip parallel to (001) cleavage planes generated void space that was subsequently filled by secondary phases. As both, void space with and without secondary phases is observed, a combination of these two scenarios is preferred.

4.3. Quartz microstructures and textures

The presence of low-angle boundaries with $2-7^\circ$ misorientation in relic quartz grains of the monomineralic quartz layer in the protomylonitic sample HM00305 separating subgrains with grain sizes of 70–100 μm point to subgrain rotation recrystallisation (Fig. 4a). Contrastingly, grain sizes of recrystallised quartz grains in nearly pure quartz layers in the ultramylonitic sample M1206 are significantly smaller (25–65 μm , Figs 5 and 7). Compared with the monomineralic Qtz layers, grain sizes of isolated quartz grains within fine grained albite aggregates are significantly smaller (<40 μm) in both samples. However, the presence of straight grain boundary segments and 120° dihedral angles of quartz grain boundary intersections in the ultramylonitic sample M1206 (Figs 5 and 7) suggest post-deformational static recrystallisation and grain boundary area reduction (Passchier and Trouw, 2005), potentially related with some grain growth

post-dating deformation. Therefore, grain-sizes in this sample most likely represent maximum estimates.

Dynamic recrystallisation of quartz is accommodated by a combination of basal, rhomb and prism $\langle a \rangle$ slip, as indicated by the textures of the quartz c -axes (cf. Passchier and Trouw, 2005). Basal and rhomb $\langle a \rangle$ slip dominate in the protomylonitic sample HM00305, while prism $\langle a \rangle$ slip predominated in the ultramylonitic sample M1206 (Figs 4–5 and 7). Assuming the same Upper-greenschist facies Cretaceous metamorphic temperatures of $c.500^{\circ}\text{C}$ (Habler et al., 2009) in both samples, the different proportions of active slip systems relate to differences in strain rates ($\dot{\epsilon}$). Based on the grain sizes of quartz, and applying the piezometer of Twiss (1980) and the flow law of Gleason and Tullis (1995; see also Stipp et al., 2002), the minimum relative difference in strain rate between HM00305 and M1206 is at about 1–2 orders of magnitude at strain rates of $\sim 10^{-13}\text{s}^{-1}$ and $\sim 10^{-11}\text{s}^{-1}$, respectively.

4.4. Implications from geochronology

Regional metamorphic zonation in the Ötztal–Stubai crystalline basement (OSC) largely has been inferred from the systematic distribution of K–Ar and Rb–Sr biotite ages and the regional distribution of Cretaceous mineral assemblages (Thöni, 1981). The Cretaceous metamorphic overprint in the OSC, which had been affected by predominant Variscan age regional metamorphism, increases from NW to SE as indicated by the appearance of the following metamorphic minerals associated with the corresponding radiometric mineral ages: (i) a zone without Cretaceous metamorphic mineral content, corresponding to Carboniferous K–Ar biotite cooling ages; (ii) a stilpnomelane and a chloritoid zone, both characterised by incomplete resetting of the K–Ar isotopic system or excess ^{40}Ar in biotite (Thöni, 1981); and (iii) the Eo–Alpine staurolite zone, which correlates with Late Cretaceous K–Ar and Rb–Sr biotite cooling ages.

According to this zonation the study area is located in zone ii) reflecting Cretaceous Ctd formation in metapelitic rocks. A new biotite–whole rock Rb–Sr age from an undeformed metapelitic schist in the Upper–Austroalpine Matsch Unit neither dates Permo–Triassic metamorphism related with pegmatite emplacement, nor Cretaceous cooling/resetting. Although the closure temperature for the Rb–Sr system in biotite is supposed to range at $350\text{--}400^{\circ}\text{C}$ (Jäger, 1967), far below the Cretaceous metamorphic temperatures of 500°C in the study area (Habler et al., 2009), Bt–WR Rb–Sr ages

ranging at 125–143 Ma (Haas, 1985; this study) suggest incomplete Rb–Sr isotopic resetting. This could either be related to: (i) rather dry conditions during Cretaceous metamorphism (e.g. Kühn et al., 2000); (ii) the undeformed nature of the sample used for Rb–Sr dating of biotite; or (iii) severe overestimation of Cretaceous metamorphic temperatures. Point (i) seems unlikely, as sample HM07903 contains Cretaceous chlorite. The last point (iii) also seems unlikely, as sample HM07903 contains fine-grained staurolite of presumably Cretaceous age, which crystallized at the expense of Permian–Triassic andalusite, and requires more than 500° C to form even in Al-rich local bulk systems with high Fe/Mg ratio. Therefore, the presence and/or absence of deformation-induced defects (dislocations, cracks, stacking faults), which could have reduced the diffusion domain size, seem to significantly affect the Rb–Sr system of biotite at 500°C.

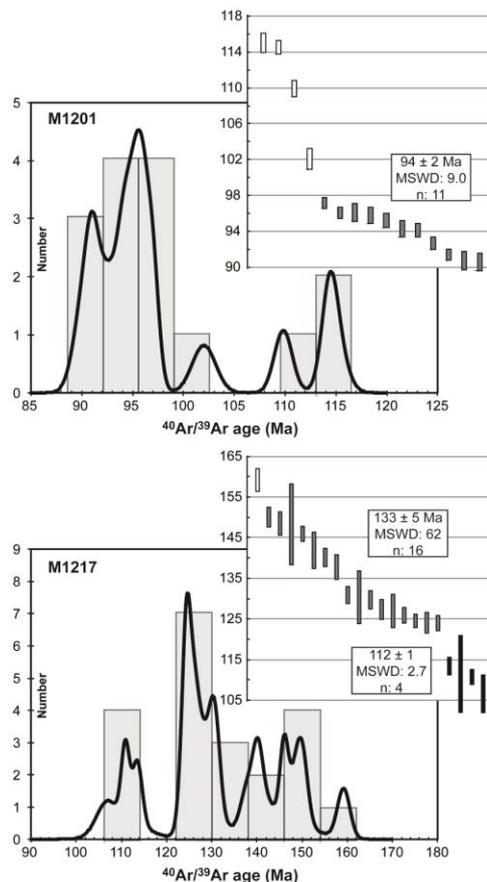


Figure 8 Relative probability and histogram of $^{40}\text{Ar}/^{39}\text{Ar}$ single spot ages from samples M1201 and M1217. Insets are weighted distribution of the same data giving 2σ errors.

The weakly deformed protomylonite sample M1217 has generally higher in-situ $^{40}\text{Ar}/^{39}\text{Ar}$ ages compared to those of the mylonitic sample M1201 (Table 1; Fig. 8), with one exception of an overlapping age group at *c.*115 Ma. Considering similar closure temperatures for Ar-diffusion in muscovite and Sr-diffusion in biotite (350–400°C), $^{40}\text{Ar}/^{39}\text{Ar}$ ages of muscovite should be similar to Rb–Sr ages of biotites from spatially associated rocks. Following this, $^{40}\text{Ar}/^{39}\text{Ar}$ ages of deformed muscovite should be younger than Rb–Sr ages from undeformed biotite. Actually in-situ $^{40}\text{Ar}/^{39}\text{Ar}$ ages from large muscovite clasts in the weakly deformed sample M1217 coincide with Rb–Sr biotite ages from an undeformed metapelitic schist. Considering the generally younger $^{40}\text{Ar}/^{39}\text{Ar}$ ages in the ultramylonitic Permian meta-pegmatite and the significantly smaller age variation of the single spot data, it is inferred, that deformation at 500°C is required for complete resetting of $^{40}\text{Ar}/^{39}\text{Ar}$ ages of coarse-grained muscovite clasts. Consequently, the mean 94 ± 2 Ma $^{40}\text{Ar}/^{39}\text{Ar}$ age from the mylonitic sample M1201 is interpreted to reflect the timing of Cretaceous upper-greenschist facies deformation.

The geological significance of the Lower Cretaceous in-situ $^{40}\text{Ar}/^{39}\text{Ar}$ muscovite and Bt–WR Rb–Sr ages from weakly deformed and undeformed minerals remains enigmatic. However, the similar blocking temperatures for Ar-diffusion in muscovite and Sr-diffusion in biotite and the consistent age results point to a similar effect of Cretaceous metamorphism on the isotopic systems. The degree of isotopic alteration may depend on heating rate, duration of elevated Cretaceous temperatures and the presence/absence of grain boundary fluids and deformation. However, the wide range of $^{40}\text{Ar}/^{39}\text{Ar}$ muscovite single spot ages obtained from the weakly deformed sample on the one hand and the availability of a single Rb–Sr Bt–WR age for comparison on the other hand demand for caution in interpreting the average $^{40}\text{Ar}/^{39}\text{Ar}$ muscovite age as a separate geological event.

Although statistically meaningless, two in-situ $^{40}\text{Ar}/^{39}\text{Ar}$ spot ages in the weakly deformed Permian meta-pegmatite sample M1217 at 359 Ma and 266 Ma are significantly older than the other data obtained from this sample (Table 1). However, the Permian age of 266.5 Ma coincides with available Sm–Nd garnet–whole rock ages of 263–280 Ma, which were interpreted to constrain the time of Permian pegmatite emplacement (Habler et al., 2009).

5. Conclusions

1. Different muscovite clasts from protomylonitic, mylonitic and ultramylonitic Permian meta-pegmatite form mica-fish and display significant grain-internal deformation, as indicated by the presence of intracrystalline lattice bending, (micro-)kinks and dynamic recrystallisation along zones of high defect densities and cracks
2. Electron Backscatter Diffraction analysis showed that (001) planes of muscovite are commonly oriented at a small angle ($<25^\circ$) relative to the mylonitic foliation. In one grain the $[\bar{3}10]$ direction of muscovite is roughly oriented parallel to the Y-axis of shear flow, and represents the axis of muscovite lattice rotation related with kinks. In all other grains/samples, the $[\bar{3}10]$ direction of muscovite differs from the rotation axis. The latter always lies within the (001) plane and is parallel to the Y-direction of shear flow. Therefrom we infer that, except for the orientation of the (001) plane, the intracrystalline deformation is not controlled by the relative orientation of crystallographic anisotropies with respect to the kinematic frame, but the Y-axis rather seems to be the lattice rotation axis, irrespective of the clast orientation with respect to shear flow
3. Muscovite rotation axes parallel to muscovite $[\bar{3}10]$ is consistent with intracrystalline deformation accommodated by the (001)[110] slip system assuming an edge character of the dislocations. In the other cases, dislocations with different burgers vectors are required to accommodate crystal plastic lattice deformation
4. Quartz microstructures and textures suggest the activity of basal, rhomb and prism $\langle a \rangle$ slip during subgrain rotation recrystallization. Assuming a strain-rate dependence of the different slip systems points to strain rate differences between the protomylonitic sample HM00305 and the ultramylonitic sample M1206 by about 2 orders of magnitude ($\sim 10^{-13} \text{ s}^{-1} - 10^{-11} \text{ s}^{-1}$)
5. Deformation at 500°C is obviously required for a complete resetting of Rb-Sr biotite and $^{40}\text{Ar}/^{39}\text{Ar}$ muscovite ages. Consequently, the mean $94 \pm 2 \text{ Ma}$ $^{40}\text{Ar}/^{39}\text{Ar}$ muscovite age from the mylonitic sample M1201 is interpreted to reflect the timing of upper-greenschist facies Cretaceous deformation in the Upper-Austroalpine Matsch Unit.

6. Appendix – Supplementary Argon data

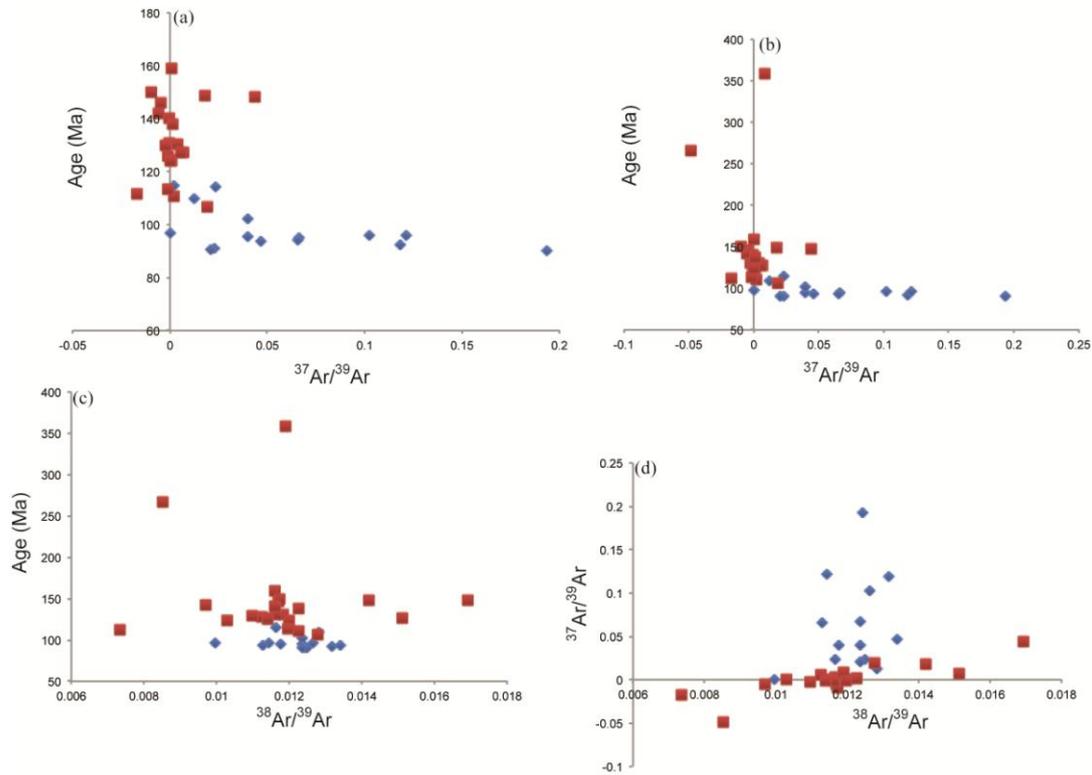


Figure A.1 (a–b) $^{37}\text{Ar}/^{39}\text{Ar}$ vs. age in Ma binary plots for muscovite from the Upper–Austroalpine Matsch Unit in Southern Tyrol. Red symbols represent sample M1217 and blue symbols sample M1201. High values (extraneous) of ^{37}Ar may be produced from intergrown calcite or chlorite. (a) is plotted excluding the two oldest ages and with a y-axis scale different from (b). (c) $^{38}\text{Ar}/^{39}\text{Ar}$ vs age in Ma binary plots using the same color coding as in (a) and (b). High ^{38}Ar values may be indicative of elevated Cl content, possibly due to intergrown biotite. (d) $^{38}\text{Ar}/^{39}\text{Ar}$ vs $^{37}\text{Ar}/^{39}\text{Ar}$ graph using the same color code.

Acknowledgements

Funding was provided by the University of Vienna (Doctoral School IK052) and the Austrian Science Fund (FWF): I471–N19 as part of the International Research Group FOR 741 D–A–CH. The authors acknowledge access to the Laboratory for scanning electron microscopy and focused ion beam applications of the Faculty of Geosciences, Geography and Astronomy at the University of Vienna (Austria). M. Horschneegg and W. Wegner are thanked for assistance during ID–TIMS analyses and discussion.

References

- Bailey, S.W., 1984. Crystal chemistry of the true micas. Bailey, S.W. (ed) 1984, *Reviews in Mineralogy –Volume 13 Micas*. Mineralogical Society of America, 13–60.

- Behrmann, J.H., 1984. A study of white mica microstructure and microchemistry in a low grade mylonite. *Journal of Structural Geology*, 6, 283–292.
- Bell, I.A., Wilson, C.J.L., 1981. Deformation of biotite and muscovite. TEM microstructure and deformation model. *Tectonophysics*, 78, 201–228.
- Bell, I.A., Wilson, C.J.L., McLaren, A.C., Etheridge, M.A., 1986. Kinks in Mica: Role of Dislocations and (001) Cleavage. *Tectonophysics*, 127, 49–65.
- Beltrando, M., Lister, G.S., Forster, M., Dunlap, W.J., Fraser, G., Hermann, J., 2009. Dating microstructures by the $^{40}\text{Ar}/^{39}\text{Ar}$ step-heating technique: Deformation-pressure-temperature-time history of the Penninic Units of the Western Alps. *Lithos*, 113, 801-819.
- Beltrando, M., Di Vincenzo, G., Ferraris, C., 2013. Preservation of sub-microscopic structural relicts in micas from the Gran Paradiso Massif (Western Alps): Implications for $^{40}\text{Ar}/^{39}\text{Ar}$ geochronology. *Geochimica et Cosmochimica Acta*, 119, 359-380.
- Bestmann, M., Pennacchioni, G., Frank, G., Göken, M., de Wall, H., 2011. Pseudotachylyte in muscovite-bearing quartzite: Coseismic friction-induced melting and plastic deformation of quartz. *Journal of Structural Geology*, 33, 169–186.
- Bröcker, M., Baldwin, S., Arkudas, R., 2013. The geological significance of $^{40}\text{Ar}/^{39}\text{Ar}$ and Rb–Sr white mica ages from Syros and Sifnoy, Greece: a record of continuous (re)crystallization during exhumation? *Journal of Metamorphic Geology*, 31, 629–646.
- Cosca, M., Stünitz, H., Bourgeix, A.L., Lee, J.P., 2011. $^{40}\text{Ar}^*$ loss in experimentally deformed muscovite and biotite with implications for $^{40}\text{Ar}/^{39}\text{Ar}$ geochronology of naturally deformed rocks. *Geochimica et Cosmochimica Acta*, 75, 7759-7778.
- Dempsey, E.D., Prior, D.J., Mariani, E., Toy, V.G., Tatham, D.J., 2009. Mica-controlled anisotropy within mid-to-upper crustal mylonites: an EBSD study of mica fabrics in the Alpine Fault Zone, New Zealand. From Prior, D.J., Rutter, E.H., Tatham, D.J. (eds) 2009, *Deformation Mechanisms, Rheology and*

- Tectonics: Microstructures, Mechanics and Anisotropy. Geological Society, London, Special Publications, 360, 33–47.
- Dunlap, W.J., Kronenberg, A.K., 2001. Argon loss during deformation of micas: constraints from laboratory deformation experiments. *Contributions to Mineralogy and Petrology*, 141, 174-185.
- Foster, M.A., Lister, G.S., 2004. The interpretation of $^{40}\text{Ar}/^{39}\text{Ar}$ apparent age spectra produced by mixing: application of the method of asymptotes and limits. *Journal of Structural Geology*, 26, 287–305.
- Gleason, G.C., Tullis, J., 1995. A flow law for dislocation creep of quartz aggregates determined with the molten salt cell. *Tectonophysics*, 247, 1–23.
- Grotenhuis, S.M.t., Trouw, R.A.J., Passchier, C.W., 2003. Evolution of mica fish in mylonitic rocks. *Tectonophysics*, 372, 1–21.
- Haas, R., 1985. Zur Metamorphose des südlichen Ötztalkristallins unter besonderer Berücksichtigung der Matscher Einheit (Vinschgau/Südtirol). Unpublished PhD–Thesis, Innsbruck, 118 pp.
- Habler, G., Thöni, M., Grasemann, B., 2009. Cretaceous metamorphism in the Austroalpine Matsch Unit (Eastern Alps): The interrelation between deformation and chemical equilibration processes. *Mineralogy and Petrology*, 97, 149-171.
- Hames, W.E., Cheney, J.T., 1997. On the loss of $^{40}\text{Ar}^*$ from muscovite during polymetamorphism. *Geochimica et Cosmochimica Acta*, 61, 3863–3872.
- Jäger, E., 1967. Die Bedeutung der Biotit–Alterswerte. In: Rb–Sr Altersbestimmungen an Glimmern der Zentralalpen. From E. Jäger, E. Niggli and E. Wenk (eds). *Beiträge zur Geologischen Karte der Schweiz*, NF, 134, 28–31.
- Kramar, N., Cosca, M., Buffat, P.A., Baumgartner, L., 2003. Stacking fault-enhanced argon diffusion in naturally deformed muscovite. From Vance, D., Müller, W., Villa, I. (eds) 2003, *Geochronology: Linking the Isotopic Record with Petrology and Textures*. Geological Society, London, Special Publications, 220, 249-260.
- Kramar, N., Cosca, M., Hunziker, J., 2001. Heterogeneous $^{40}\text{Ar}^*$ distribution in naturally deformed muscovite: in situ UV-laser ablation evidence for

microstructurally controlled intragrain diffusion. *Earth and Planetary Science Letters*, 192, 377-388.

Kühn, A., Glodny, J., Iden, K., Austrheim, H., 2000. Retention of Precambrian Rb/Sr phlogopite ages through Caledonian eclogite facies metamorphism, Bergen Arc Complex, W-Norway. *Lithos* 51, 305–330.

Kula, J., Spell, T.L., Zanetti, A., 2010. $^{40}\text{Ar}/^{39}\text{Ar}$ analyses of artificially mixed micas and the treatment of complex age spectra from samples with multiple mica populations. *Chemical Geology*, 275, 67–77.

Lister, G.S., Snoke, A.W., 1984. S–C Mylonites. *Journal of Structural Geology*, 6, 617–638.

Ludwig, K.R., 2003. Users manual for Isoplot/Ex version 3.0: a geochronological toolkit for Microsoft Excel. Berkley Geochronology Center Special Publication, 4, 70 pp., Berkley, California.

Mares, V.M., Kronenberg, A.K., 1993. Experimental deformation of muscovite. *Journal of Structural Geology*, 15, 1061–1075.

Markley, M.J., Teyssier, C., Cosca, M., 2002. The relation between grain size and $^{40}\text{Ar}/^{39}\text{Ar}$ date for Alpine white mica from the Siviez–Mischabel Nappe, Switzerland. *Journal of Structural Geology*, 24, 1937–1955.

Meike, A., 1989. In situ deformation of micas: A high-voltage electron-microscope study. *American Mineralogist*, 74, 780–796.

Misra, S., Burg, J.P., 2012. Mechanics of kink-bands during torsion deformation of muscovite aggregate. *Tectonophysics*, 548–549, 22–33.

Mulch, A., Cosca, M., Handy, M., 2002. In-Situ UV-laser $^{40}\text{Ar}/^{39}\text{Ar}$ geochronology of a micaceous mylonite: an example of defect-enhanced argon loss. *Contributions to Mineralogy and Petrology*, 142, 738-752.

Mulch, A., Cosca, M., Andresen, A., Fiebig, J., 2005. Time scales of deformation and exhumation in extensional detachment systems determined by high-spatial resolution in situ UV-laser $^{40}\text{Ar}/^{39}\text{Ar}$ dating. *Earth and Planetary Science Letters*, 233, 375-390.

- Passchier, C.W., Trouw, R.A.J., 2005. *Microtectonics*. Springer–Verlag, Berlin Heidelberg, New York, 366p.
- Prior, D.J., Boyle, A.P., Brenker, F., Cheadle, M.C., Day, A., Lopez, G., Peruzzo, L., Potts, G.J., Reddy, S., Spiess, R., Timms, N.E., Trimby, P., Wheeler, J., Zetterström, L., 1999. The application of electron backscatter diffraction and orientation contrast imaging in the SEM to textural problems in rocks. *American Mineralogist* 84, 1741–1759.
- Prior, D.J., Mariani, E., Wheeler, J., 2009. EBSD in the Earth Sciences: Applications, Common Practice, and Challenges. From Schwartz, A., Kumar, M., Adams, B.L., Field, D.P. (eds) 2009, *Electron Backscatter Diffraction in Materials Science*. Springer, 2nd edition, 345–360.
- Reddy, S.M., Kelley, S.P., Wheeler, J., 1996. A $^{40}\text{Ar}/^{39}\text{Ar}$ laser probe study of micas from the Sesia Zone, Italian Alps: implications for metamorphic and deformation histories. *Journal of Metamorphic Geology*, 14, 493–508.
- Rosenbaum, G., Menegon, L., Glodny, J., Vasconcelos, P., Ring, U., Massironi, M., Thiede, D., Nasipuri, P., 2012. Dating deformation in the Gran Paradiso Massif (NW Italian Alps): Implications for the exhumation of high-pressure rocks in a collisional belt. *Lithos*, 144-145, 130-144.
- Reddy, S.M., and Potts, G.J., 1999. Constraining absolute deformation ages: the relationship between deformation mechanisms and isotope systematics. *Journal of Structural Geology*, 21, 1255-1265.
- Renne, P.R., Swisher, C.C., Deino, A.L., Karner, D.B., Owens, T.K., DePaolo, D.J., 1998. Intercalibration of standards, absolute ages and uncertainties in $^{40}\text{Ar}/^{39}\text{Ar}$ dating. *Chemical Geology*, 145, 117–152.
- Schmid, D.W., Podladchikov, Y.Y., 2005. Mantled porphyroblast gauges. *Journal of Structural Geology*, 27, 571–585.
- Steiger, R.H., Jäger, E., 1977. Subcommittee on Geochronology: Convention on the use of decay constants in geo- and cosmochronology. *Earth and Planetary Science Letters* 36, 359–362.

- Stipp, M., Stünitz, H., Heilbronner, R., Schmid, S., 2002. Dynamic recrystallization of quartz: correlation between natural and experimental conditions. From De Meer, S., Drury, M.R., De Bresser, J.H.P., Pennock, G.M. (eds) 2002, *Deformation Mechanisms, Rheology and Tectonics: Current Status and Future Perspectives*. Geological Society, London, Special Publications, 200, 171–190.
- Thöni, M., 1981. Degree and Evolution of the Alpine Metamorphism in the Austroalpine Unit W of the Hohe Tauern in the light of K/Ar and Rb/Sr Age Determinations on Micas. *Jahrbuch der Geologischen Bundesanstalt* 124–1, 111–174, Wien.
- Thöni, M., 1986. The Rb-Sr thin slab isochron method – An unreliable geochronological method for dating geological events in polymetamorphic terrains? – Evidence from the Austroalpine basement Nappe, The Eastern Alps. *Memorie di Scienze Geologiche*, 38, 283-352.
- Twiss, R.J., 1980. Static theory of size variation with stress for subgrains and dynamically recrystallized grains. In: USGS (ed) *Proceedings of the IX. Conference, Magnitude of Deviatoric Stresses in the Earth's Crust and Upper Mantle*. Open File Report, 80–625, Menlo Park, California, 665–683.

3 Supplementary data

Table 3.1 gives an overview of all samples and methods applied to these, which are part of this thesis. Samples and methods in bold letters are not part of the 3 paper manuscripts, and hence are presented in this chapter. These include observations made with the optical microscope (OM) and the scanning electron microscope (SEM) and results from electron probe microanalyses (EPMA) from 5 metapelitic rocks and 1 Permian meta-pegmatite. Additionally, electron backscatter diffraction analyses (EBSD) of albite, muscovite and quartz from the Permian meta-pegmatite samples HM00305, M1201 and M1206, which are not presented in the paper manuscripts, are introduced further below. Analytical settings for mineral compositional analyses (EPMA) and microstructural and textural analyses (EBSD) are the same as described in the paper manuscripts.

Table 3.1 Samples and methods of this thesis. Horizontal lines separate samples from different outcrops. Coordinates are based on UTM Zone 32T, WGS84, and given with an accuracy of ± 10 m.

Sample	Rock type	Coordinates (N/E, UTM 32T, WGS84, ± 10 m)	OM	SEM	EPMA	EBSD	ID-TIMS (Ms/Bt)	ICP-OES/MS
M1201	mylonitic metapegmatite	5170319m, 640984m	x	x	x	x	x	x
M1202	mylonitic metapegmatite	"	x	x				
M1203	mylonitic metapegmatite	"	x	x			x	x
M1204	mylonitic metapelite	"	x					
M1205	mylonitic metapelite	"	x					
M1206	ultramylonitic metapegmatite	"	x	x	x	x	x	
M1209	weakly deformed metapegmatite	5170589m, 640300m	x	x				
M1210	weakly deformed metapegmatite	"	x	x			x	x
M1217	weakly deformed metapegmatite	5170206m, 640396m	x	x	x		x	x
M1218	weakly deformed metapegmatite	"	x	x				
M1222	metapelitic schist	5170391m, 641100m	x					
HM00205	mylonitic metapegmatite	5170494m, 641263m	x	x	x			
HM00305	mylonitic metapegmatite	"	x	x	x	x	x	x
HM07903	metapelitic schist	boulder, collected near the Mastaun Joch	x	x			x	
HM27603	metapelitic schist	boulder, collected NW of Wiegenspitze	x	x	x			
HM15104	undeformed metapegmatite	5168383m, 624302m	x		x			
HM22204	metapelitic schist	5169080m, 626553m	x	x	x			

3.1 OM and SEM

Samples M1204 and M1205 are mylonitic metapelites (Fig. 3.1), which were collected in the same outcrop as some of the Permian meta-pegmatite samples (Table 3.1; see also Fig. 1d of paper #1). Samples M1222, HM27603 and HM22204 are metapelitic schist from 3 different outcrops and sample HM15104 is a macroscopically undeformed Permian meta-pegmatite (Figs 3.1 and 3.2).

Cretaceous deformation in the metapelitic rocks is expressed by a strong mylonitic foliation and a S-C' type fabric (Figs 3.1a–b). Relic garnet porphyroclasts often exhibit an internal fabric (F_{n+1}), indicating syn- to post-deformational growth with respect to a deformation event D_{n+1} (Figs 3.1a and 3.2c–d). The growth of large staurolite post-

Supplementary data

dates a deformation event D_{n+2} , which, in turn, post-dates the formation of the garnet crystals. This is shown in sample HM07903, which is presented in paper #3. Then, garnet and staurolite broke down during rising temperatures within the stability field of sillimanite to form biotite and sillimanite according to the reaction $\text{Grt} + \text{St} + \text{Ky} \rightarrow \text{Bt} + \text{Sill} + \text{Pl}$ (Figs 3.1a and 3.2). During the Cretaceous, a second garnet generation formed, either as small, euhedral grains within microlithons (Fig. 3.1b), or as thin rims (Grt_C) on pre-existing, Variscan relic garnet (Grt_V , Figs 3.2a–b). Another characteristic Cretaceous mineral is chloritoid. In sample M1222, this mineral was found in an Al-rich domain, mainly composed of fine-grained muscovite (Fig. 3.1c). Additionally, chloritoid may occur within C' -planes of the Cretaceous fabric, illustrating the syn-deformational growth.

Despite the macroscopically undeformed nature, the Permian meta-pegmatite sample HM15104 from the western part of the Upper-Austroalpine Matsch Unit, shows prominent evidence for deformation (Fig. 3.1d). Feldspar is characterized by weak undulose extinction and cracks, muscovite shows undulose extinction, cracks and recrystallization and quartz is characterized by intracrystalline deformation and bulging recrystallization, especially along grain boundaries (Fig. 3.1d).

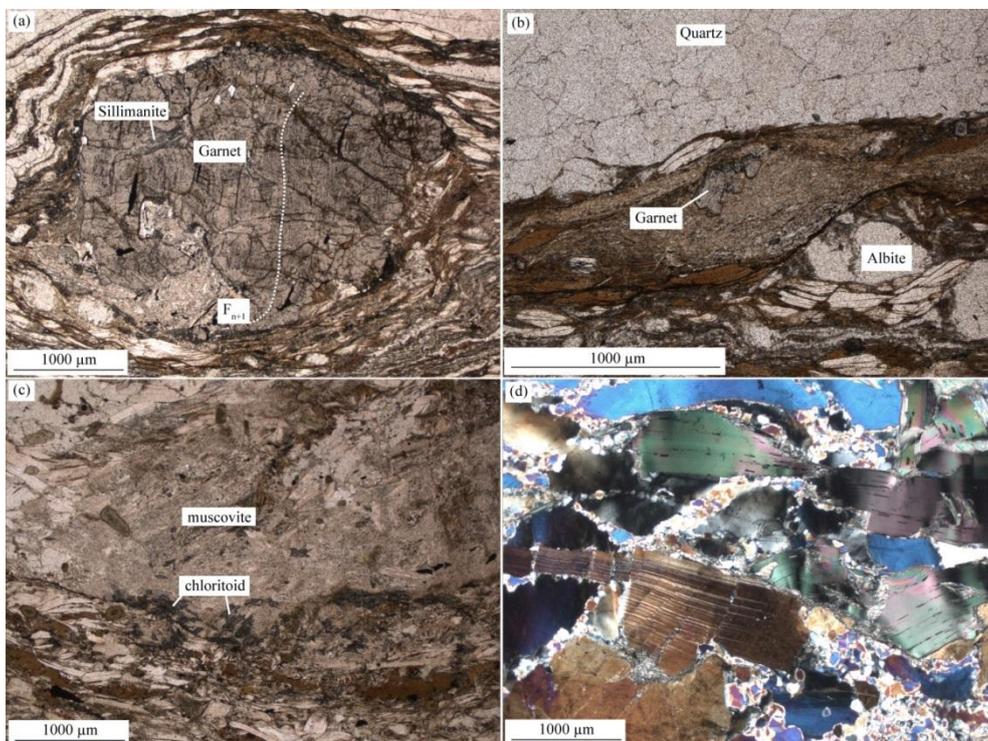


Figure 3.1 Representative microstructures of (a) the mylonitic metapelite M1204, (b) the mylonitic metapelite M1205, (c) the metapelitic schist M1222, and (d) the Permian meta-pegmatite sample HM15104.

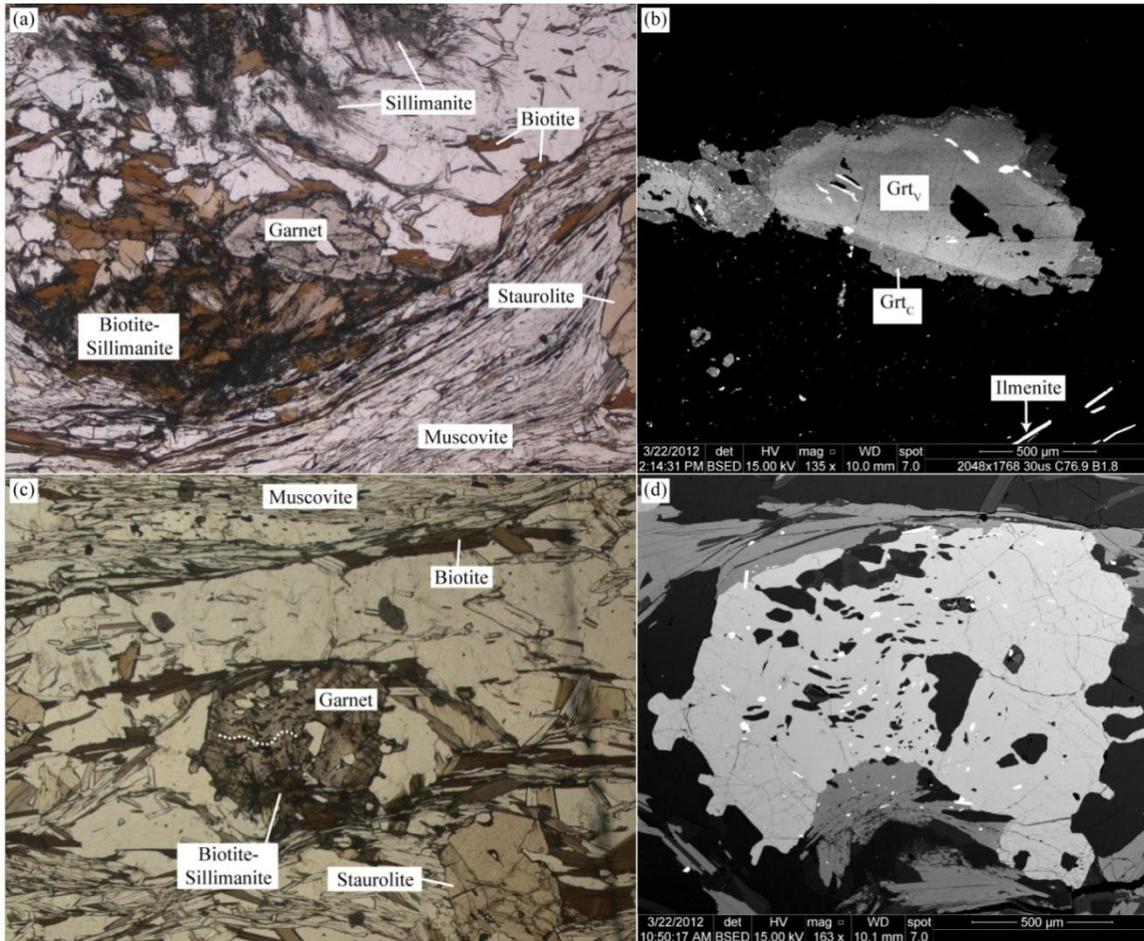


Figure 3.2 Representative microstructures of (a–b) sample HM27603, and (c–d) HM22204. (b) and (d) are BSE images of the garnets shown in the microphotographs in (a) and (c), that were taken with the scanning electron microscope.

3.2 EPMA

Tables 3.2–4 summarize one representative mineral compositional analysis for each of the rock-forming mineral phases in the samples HM27603, HM22204 and HM15104. Aligned biotite and muscovite form the D_{n+2} foliation (Figs 3.2a and 3.2c). Biotite typically has 2.69 cations per formula unit (c.p.f.u.) Si, ~ 1.8 c.p.f.u. Al and >0.9 c.p.f.u. Mg (based on 11O). Associated muscovite is characterised by <3.1 c.p.f.u. Si, >2.8 c.p.f.u. Al, and some paragonite-component with ~ 0.18 c.p.f.u. Na and ~ 0.76 c.p.f.u. K (based on 11O; Tables 3.2–3). Ilmenite, additionally defining the D_{n+2} foliation in HM27603 and HM22204 has ~ 2 c.p.f.u. Ti and 1.9 c.p.f.u. Fe, with negligible concentrations of other measured elements (based on 6O; Tables 3.2–3). Albite feldspar typically has 0.15 c.p.f.u. Ca or less at >0.86 c.p.f.u. Na and low K-concentrations (based on 8O). Variscan garnet (Grt_v , Fig. 3.2b, Table 3.2) is typically richer in Fe with >2.3 c.p.f.u. Fe_{total} , compared to Cretaceous garnet rims (Grt_c , Fig. 3.2b, Table 3.2) with ~ 2.2 c.p.f.u. Fe or less. Cretaceous garnet is also significantly richer in Ca with ~ 0.4

Supplementary data

c.p.f.u. Ca (based on 12O). However, sample HM22204 does not contain the Ca-rich, Cretaceous garnet generation.

Table 3.2 Representative compositional mineral analyses for each rock-forming mineral in the metapelitic sample HM27603. (Abbreviations for Generation: P = Permian; C = Cretaceous; V = Variscan; pC = presumably pre-Cretaceous).

Phase	Biotite	Chloritoid	Garnet		Muscovite	Ilmenite	Albite	Staurolite
Generation	P	C	V	C	pC	pC	pC	V
Sample	HM27603	HM27603	HM27603	HM27603	HM27603	HM27603	HM27603	HM27603
Position	core	core	core	rim	core	core	core	core
SiO ₂	35.21	24.19	36.81	37.01	46.06	0.07	64.57	28.14
TiO ₂	1.35	0.03	0.00	0.13	0.27	52.70	0.00	0.44
Al ₂ O ₃	19.60	40.73	21.09	21.23	36.77	0.04	22.18	53.19
Cr ₂ O ₃	0.03	0.00	0.00	0.00	0.02	0.00	0.00	0.00
Fe ₂ O ₃	18.96	23.47	35.96	33.18	0.78	44.75	0.02	14.20
MnO	0.05	0.29	2.11	2.42	0.04	0.70	0.02	0.14
MgO	10.17	2.76	2.42	1.99	0.55	0.34	0.00	1.68
CaO	0.00	0.00	1.60	4.50	0.00	0.02	3.14	0.00
Na ₂ O	0.22	0.00	0.02	0.01	1.44	0.00	10.01	0.03
K ₂ O	8.71	0.01	0.00	0.00	9.16	0.00	0.07	0.00
Total	94.29	91.47	100.00	100.47	95.11	98.61	100.01	97.82
Oxygens	11	6	12	12	11	6	8	23
Si	2.69	1.00	2.98	2.97	3.05	0.00	2.85	3.91
Ti	0.08	0.00	0.00	0.01	0.01	2.02	0.00	0.05
Al	1.77	1.99	2.01	2.01	2.87	0.00	1.15	8.71
Cr	0.00	0.00	0.00	0.00	0.00	0.00	0.00	0.00
Fe	1.21	0.82	2.43	2.23	0.04	1.90	0.00	1.65
Mn	0.00	0.01	0.14	0.16	0.00	0.03	0.00	0.02
Mg	1.16	0.17	0.29	0.24	0.05	0.03	0.00	0.35
Ca	0.00	0.00	0.14	0.39	0.00	0.00	0.15	0.00
Na	0.03	0.00	0.00	0.00	0.18	0.00	0.86	0.01
K	0.85	0.00	0.00	0.00	0.77	0.00	0.00	0.00
Total	7.79	4.00	8.00	8.00	6.98	3.98	5.01	14.69

Instead, a secondary, fine-grained generation of staurolite was found in this sample. Compared to the mm-sized staurolite crystals, one small grain is richer in Al, with ~9 c.p.f.u. Al, contrasting <8.9 c.p.f.u. Al in the large grains (based on 23O). Additionally, the small grain is slightly poorer in Fe, compared to the large clasts and has less Mg (Table 3.3). Cretaceous chloritoid is typically rich in Al (up to 2 c.p.f.u., based on 6O) and Fe (up to 1.24 c.p.f.u.). Si is typically close to 1 c.p.f.u. Si (based on 6O; Tables 3.2–3).

Representative mineral compositional analyses for albite and muscovite Wm I and Wm III from the Permian meta-pegmatite HM15104 (see paper #2 for definition of Wm I and Wm III) are given in Table 3.4. In this sample, Albite is typically rich in Na (~0.9 c.p.f.u. Na) and poorer in Ca (~0.1 c.p.f.u. Ca) at low K-contents (based on 8O). Cores of large muscovite grains typically have close to 3 c.p.f.u. Si and elevated Al-contents (up to 2.9 c.p.f.u. Al). Fine-grained, presumably Cretaceous, muscovite (<50 μm) is significantly richer in Si (up to 3.2 c.p.f.u. Si), Fe (with 0.14 c.p.f.u.) and Mg (with 0.13

Supplementary data

c.p.f.u.), and poorer in Al (with <2.6 c.p.f.u.), generally supporting the results from analyses of Wm II and Wm III presented in paper #2.

Table 3.3 Representative compositional mineral analyses for each rock-forming mineral in the metapelitic sample HM22204. (Abbreviations for Generation: P = Permian; C = Cretaceous; V = Variscan; pC = presumably pre-Cretaceous).

Phase Generation	Biotite	Chloritoid	Garnet	Muscovite	Ilmenite	Albite	Staurolite	
	P	C	V	pC	pC	pC	V	C
Sample	HM22204	HM22204	HM22204	HM22204	HM22204	HM22204	HM22204	HM22204
Position	core	core	core	core	core	core	core	core
SiO ₂	35.01	19.43	36.72	46.56	0.03	66.40	28.03	27.79
TiO ₂	1.61	0.15	0.00	0.37	52.61	0.00	0.58	0.08
Al ₂ O ₃	19.92	29.44	21.16	36.21	0.02	21.13	54.82	55.03
Cr ₂ O ₃	0.00	0.00	0.03	0.00	0.01	0.00	0.03	0.01
Fe ₂ O ₃	20.51	31.60	34.94	0.88	44.70	0.04	13.74	12.89
MnO	0.05	0.15	4.60	0.00	1.13	0.00	0.25	0.25
MgO	8.50	6.62	2.06	0.59	0.13	0.00	1.27	0.88
CaO	0.01	0.02	0.59	0.03	0.01	1.67	0.01	0.02
Na ₂ O	0.31	0.03	0.00	1.46	0.15	10.71	0.00	0.00
K ₂ O	8.46	0.02	0.01	8.94	0.01	0.05	0.01	0.01
Total	94.37	87.47	100.11	95.05	98.80	100.02	98.77	96.99
Oxygens	11	6	12	11	6	8	23	23
Si	2.69	0.91	2.98	3.08	0.00	2.91	3.85	3.87
Ti	0.09	0.01	0.00	0.02	2.01	0.00	0.06	0.01
Al	1.80	1.63	2.03	2.82	0.00	1.09	8.87	9.02
Cr	0.00	0.00	0.00	0.00	0.00	0.00	0.00	0.00
Fe	1.32	1.24	2.37	0.05	1.90	0.00	1.58	1.50
Mn	0.00	0.01	0.32	0.00	0.05	0.00	0.03	0.03
Mg	0.97	0.46	0.25	0.06	0.01	0.00	0.26	0.18
Ca	0.00	0.00	0.05	0.00	0.00	0.08	0.00	0.00
Na	0.05	0.00	0.00	0.19	0.01	0.91	0.00	0.00
K	0.83	0.00	0.00	0.75	0.00	0.00	0.00	0.00
Total	7.75	4.27	8.00	6.97	3.99	5.00	14.65	14.61

Summary

Evidence for at least 3 distinct deformation events are recorded within the metapelitic rocks. D_{n+1} is recorded as an internal fabric in Variscan garnet (F_{n+1} in Fig. 3.1a). The second (D_{n+2}) post-dates garnet growth and pre-dates staurolite formation. The third event (D_{n+3}) overprinted the rocks during the Cretaceous, producing a S-C' fabric. This last deformation event can be recognised in both, the metapelitic rocks and the Permian meta-pegmatites. The first deformation event most likely occurred contemporaneously with prograde Variscan regional metamorphism, while D_{n+2} occurred during the retrograde path, before the rocks reached the stability field of staurolite. The rocks were then subjected to increasing temperatures within the stability field of sillimanite, most likely without deformation, as evidenced by the formation of biotite and sillimanite on the expense of Variscan garnet and staurolite. Additionally, the pegmatites lack clear evidence for a pre-Cretaceous high-temperature deformation event.

Supplementary data

Table 3.4 Representative compositional mineral analyses for the Permian meta-pegmatite sample HM15104 (Abbreviations for Generation: P = Permian; C = Cretaceous; see paper #2 for definition of Wm I and Wm III)

Phase	Albite	Muscovite	
	P	P (Wm I)	C (Wm III)
Generation	P	P (Wm I)	C (Wm III)
Sample	HM15104	HM15104	HM15104
Position	core	core	core
SiO ₂	66.35	45.25	47.73
TiO ₂	0.02	0.05	0.08
Al ₂ O ₃	21.26	36.71	32.17
Cr ₂ O ₃	0.00	0.00	0.00
Fe ₂ O ₃	0.00	1.36	2.49
MnO	0.00	0.04	0.08
MgO	0.00	0.34	1.32
CaO	1.68	0.00	0.00
Na ₂ O	10.73	0.62	0.31
K ₂ O	0.05	9.92	10.70
Total	100.13	94.27	94.89
Oxygens	8	11	11
Si	2.91	3.03	3.21
Ti	0.00	0.00	0.00
Al	1.10	2.90	2.55
Cr	0.00	0.00	0.00
Fe	0.00	0.08	0.14
Mn	0.00	0.00	0.00
Mg	0.00	0.03	0.13
Ca	0.08	0.00	0.00
Na	0.91	0.08	0.04
K	0.00	0.85	0.92
Total	5.00	6.98	6.99

Furthermore, mineral compositional analyses of various rock-forming minerals in both, the metapelitic rocks and the Permian meta-pegmatites are in line with a polyphase P–T history and upper-greenschist facies P–T conditions during Cretaceous deformation.

However, unravelling the complete pre-Cretaceous tectonometamorphic history of these rocks is difficult, although necessary for a wider understanding of the regional geology, and thus open for further investigations.

3.3 EBSD data

The following sub-chapter presents additional EBSD analyses, that are not part of either paper #1 or #3. The reasons for this are different, but in generally related to poor quality of sample preparation and problems with misindexing. However, some of the feldspar data presented below, confirm results that were obtained with the datasets presented in paper #1. Analytical settings for feldspar and muscovite are similar to those presented in papers #1 and #3, respectively.

Supplementary data

Protomylonitic sample HM00305 – Albite clast II

The presented scan shows the lower portion of the albite clast II discussed in paper #1 (cf. Fig. 2c of paper #1). The clast shows strong intracrystalline deformation with deformation bands at high angles relative to the traces of feldspar (010) and with misorientations of up to 20° as indicated by the blue scale highlighting relative to the reference point (Figs 3.3a–b). The pressure shadow on the lower left part of the image is characterised by layers of quartz and feldspar with 2 different grain size populations of the latter. Larger feldspar fragments ((1) in Fig. 3.3a; $>100\ \mu\text{m}$) are assumed to represent fragments that broke off the clast during deformation. This corresponds well with the observed crystallographic orientation data presented in the upper and lower hemisphere equal area projections in Figs 3.3c–d. The large data cluster there correspond to the orientation of the blue highlighted clast, and several smaller data clusters are representing the larger fragments in the pressure shadows. Several grains of the smaller feldspar grain size population obviously have an orientation similar to that of the blue highlighted clast, as indicated by the red–yellow color gradient highlighting (Figs 3.3e and g–h). Additionally, these smaller grains often do show some weak internal deformation, as indicated by internal misorientations of up to 18° (Fig. 3.3f). However, the bulk of the grains of the smaller feldspar grain size population have a rather random crystallographic orientation, coupled with no significant intracrystalline deformation (Figs 3.3e–h).

The observed feldspar microstructures and textures support the conclusions of paper #1 and highlight the role of fluid–assisted dissolution–precipitation of albite as the dominant deformation mechanism at upper–greenschist facies conditions, which is intimately related with grain–internal crystal–plastic and brittle deformation of the clast. Dissolution–precipitation in this sample led to precipitation of fine–grained albite grains and aggregates in the extensional quadrants of the studied clast. As observed in the kinked feldspar sample (clast I) discussed in paper #1, fine–grained albite grains related to dissolution–precipitation in this sample, often lack a crystallographic preferred orientation and consist mainly of strain–free grains (Fig. 3.3).

Supplementary data

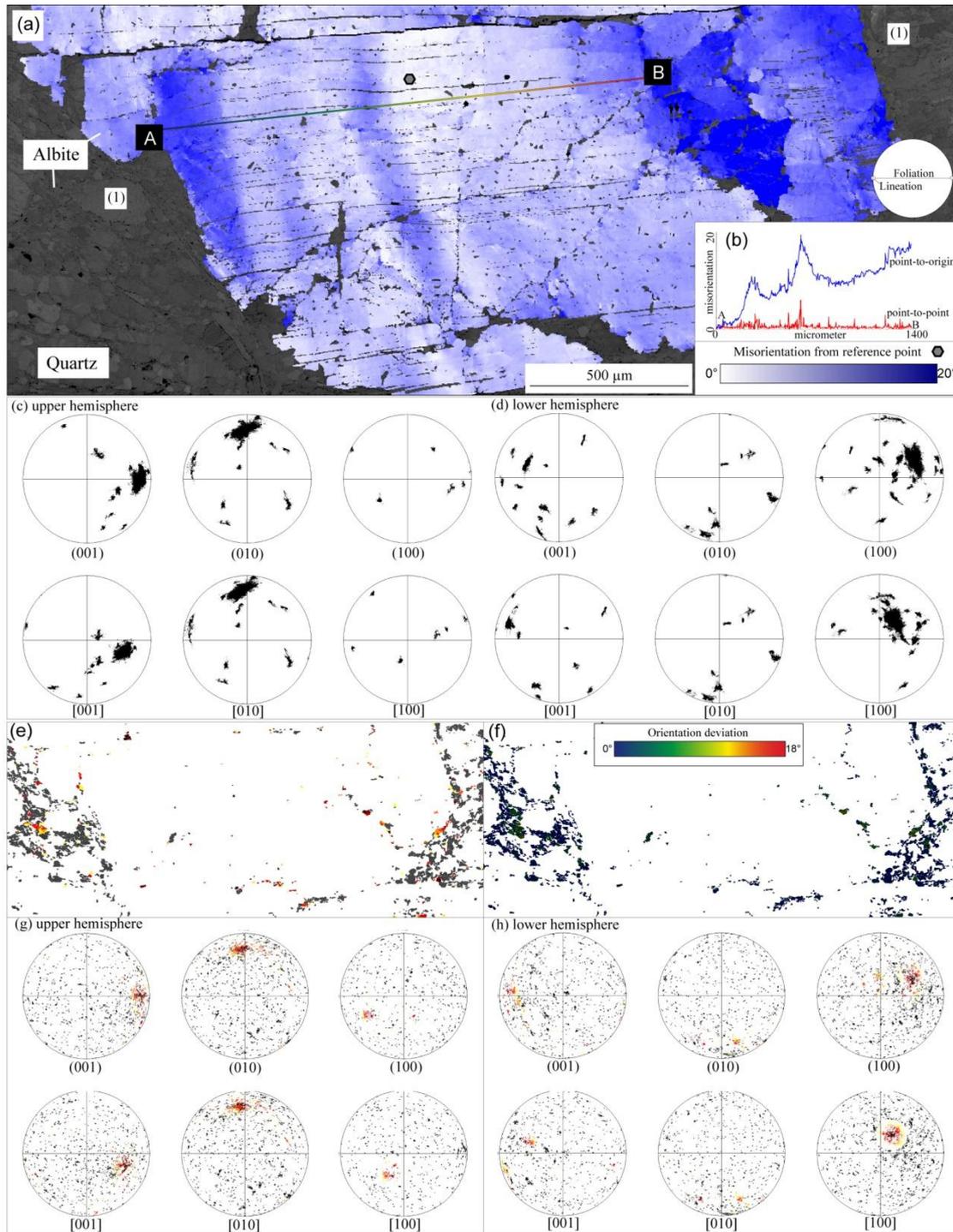
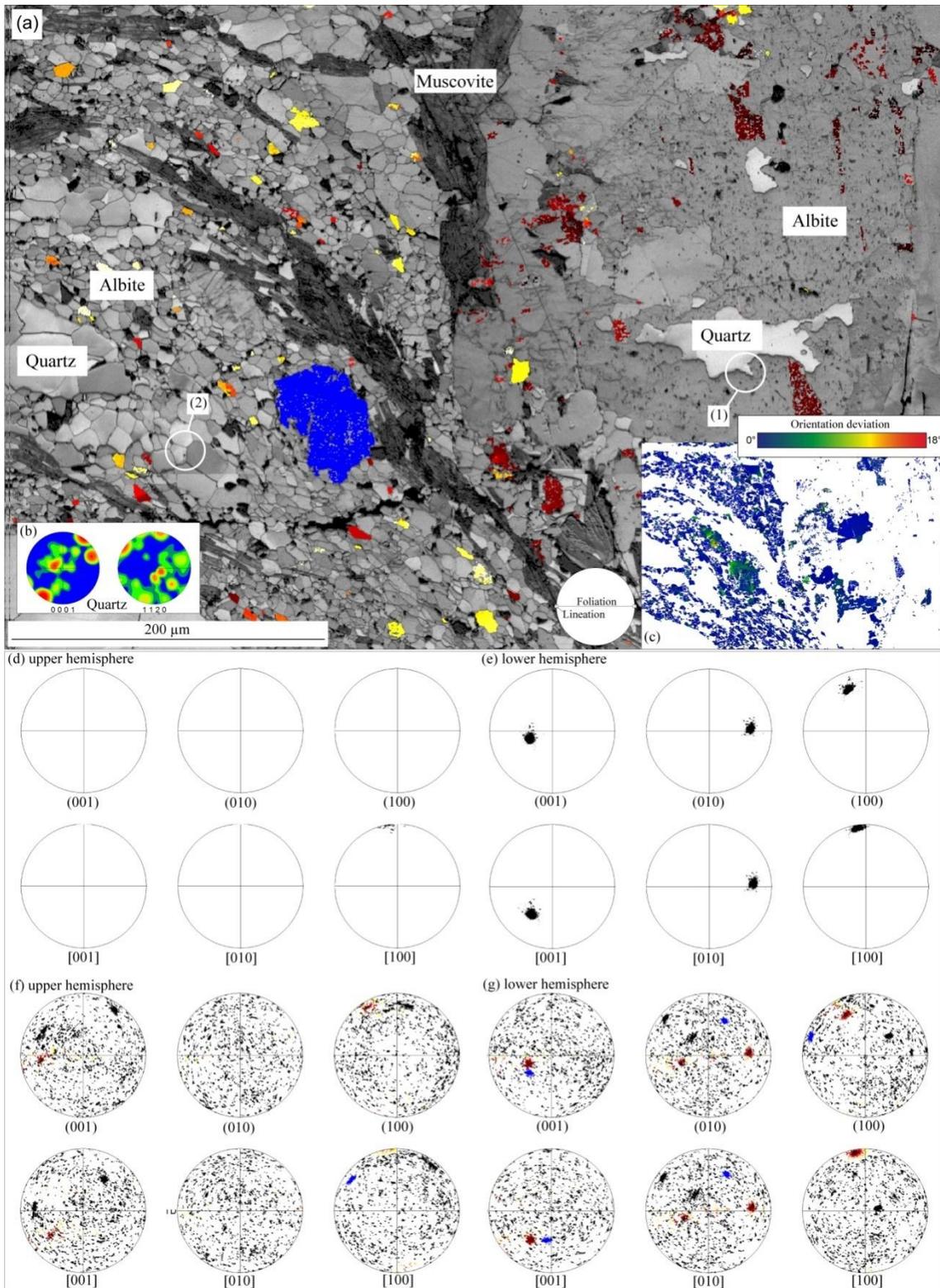


Figure 3.3 (a) EBSD pattern quality map (IQ) of the lower portion of the albite clast II with blue scale highlighting relative to the reference point and a grain-scale profile from A to B, detailed in (b). (c) Upper and (d) lower hemisphere equal area projections of orientations of the clast and clast fragments in the pressure shadow (e.g. (1) in (a)). (e) Image quality map (IQ) and (f) orientation deviation map for feldspar grains $< 50 \mu\text{m}$ in the pressure shadows. Red–yellow highlighting in (e) corresponds to the highlighting in (g–h) the upper and lower hemisphere equal area projections of the crystallographic orientations of the grains $< 50 \mu\text{m}$. Highlighting was generated in the same way as described in the figure captions for Fig. 4 of paper#1.

Supplementary data

Mylonitic sample M1201 – Albite clast I

This scan focuses on the pressure shadow of an albite clast in the mylonitic sample M1201 (Fig. 3.4). Muscovite clasts from this sample have been used for Rb–Sr and in-situ $^{40}\text{Ar}/^{39}\text{Ar}$ dating, as detailed in papers #1 and #3.



Supplementary data

Figure 3.4 (previous page) (a) EBSD pattern quality map (IQ) of the albite clast I from the mylonitic sample M1201 with highlighting as described in the text. (b) Quartz texture of recrystallised grains from the pressure shadow. (c) Orientation deviation map of the fine-grained feldspar (<70 μm) within the pressure shadow. (d–e) Upper and lower hemisphere equal area projections of the crystallographic orientation of the large albite clast on the right side of (a). (f–g) Upper and lower hemisphere equal area projections of the crystallographic orientation of the small feldspar grains (<70 μm) within the pressure shadow. Blue and red–yellow color gradient highlighting as in (a). The red–yellow color gradient highlighting is explained in the figure captions for Fig. 4 in paper#1. See text for discussion.

The albite clast is characterised by a porous rim and an inclusion of quartz (Fig. 3.4a). The shape of the associated grain boundary resembles a pinning microstructure related to grain boundary migration ((1) in Fig. 3.4a). Contrastingly, quartz grains within the pressure shadow, and hence outside the albite clast, are smaller, show straight grain boundaries and near 120° dihedral angles ((2) in Fig. 3.4a). The quartz texture of these grains, resulting from a combination of different active slip systems, is comparable to those from other mylonitic samples presented in paper #3. Several of the smaller feldspar grains in the pressure shadow and larger fragments, as shown by the red–yellow color gradient and blue highlighting, respectively, have an orientation, that is similar to the crystallographic orientation of the clast. Furthermore, especially the larger, blue highlighted fragment, is characterised by some grain–internal misorientation of up to 18° (Fig. 3.4c).

The microstructural and textural observations from this scan are broadly consistent with those mentioned above and the conclusions presented in paper #1. The observed features formed by intimately linked fluid–assisted dissolution–precipitation and brittle fracturing, coupled with some intracrystalline deformation of feldspar during upper–greenschist facies deformation in the Cretaceous. Quartz, that formed during this process, exhibits a texture, similar to that in other mylonitic samples. The pattern quality of muscovite is too low, as indicated by the dark grey–scales in Fig. 3.4a, for a proper analysis.

Mylonitic sample M1201 – Albite clast II

This EBSC scan is focused on a fold, which, in turn, is related to brittle deformation of a large albite feldspar clast in the mylonitic sample M1201. A microphotograph of this clast is also presented in Fig. 2d of paper #1. As the image quality map generally shows numerous sample preparation–related scratches and generally poor image quality (Fig. 3.5), as indicated by the dark grey scales, the focus of this sub–section is on the quartz textures within the fold and their relative formation timing with respect to this folding.

Supplementary data

For this purpose, the fold is divided into 3 different limbs, which are labelled I, II and III, respectively, in Fig. 3.5. Quartz textures for each of the 3 different limbs are presented as insets into Fig. 3.5.

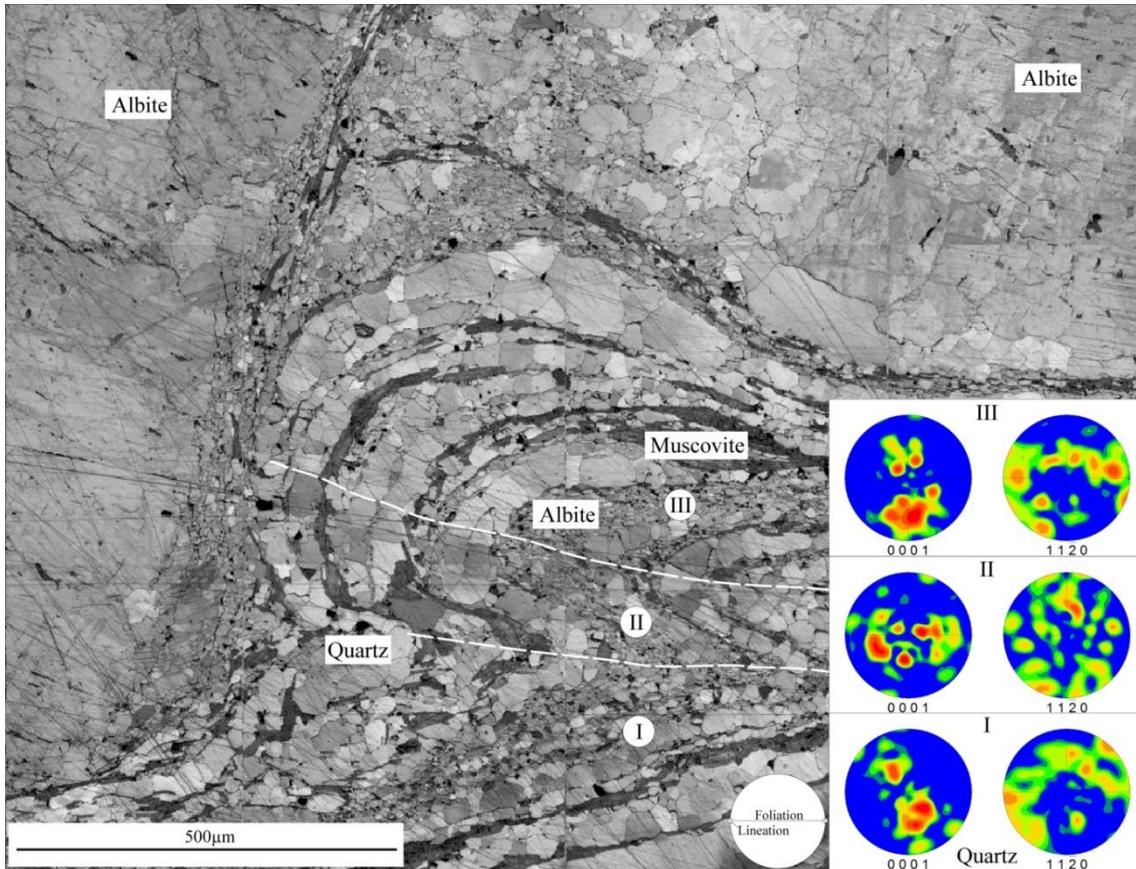


Figure 3.5 Image quality map (IQ) of a fold, associated with brittle deformation of albite. A thin section microphotograph with crossed polarised light of this situation is shown in Fig. 2d of paper#1. The inset shows the quartz textures of the 3 different limbs, which are labelled I–III.

It is directly obvious, that the quartz textures from the limbs I and III are similar. Both are different from those in limb II. This suggests, that the mylonitic foliation around the albite clast and the associated quartz textures formed first and were later passively folded. If the formation of the quartz texture post-dated the folding, the textures should be similar in all three fold limbs.

Supplementary Muscovite EBSD scans

The remaining EBSD scans are focused on muscovite clasts and microkinks (see also paper #3) within these from the ultramylonitic sample M1206 (Fig. 3.6). However, the quality of the sample preparation was generally low and problems with misindexing of muscovite were abundant. Thus, the scans presented below were omitted in the papers

Supplementary data

and are only briefly introduced here. Quartz textures are presented in 2 cases. These are comparable to those presented already.

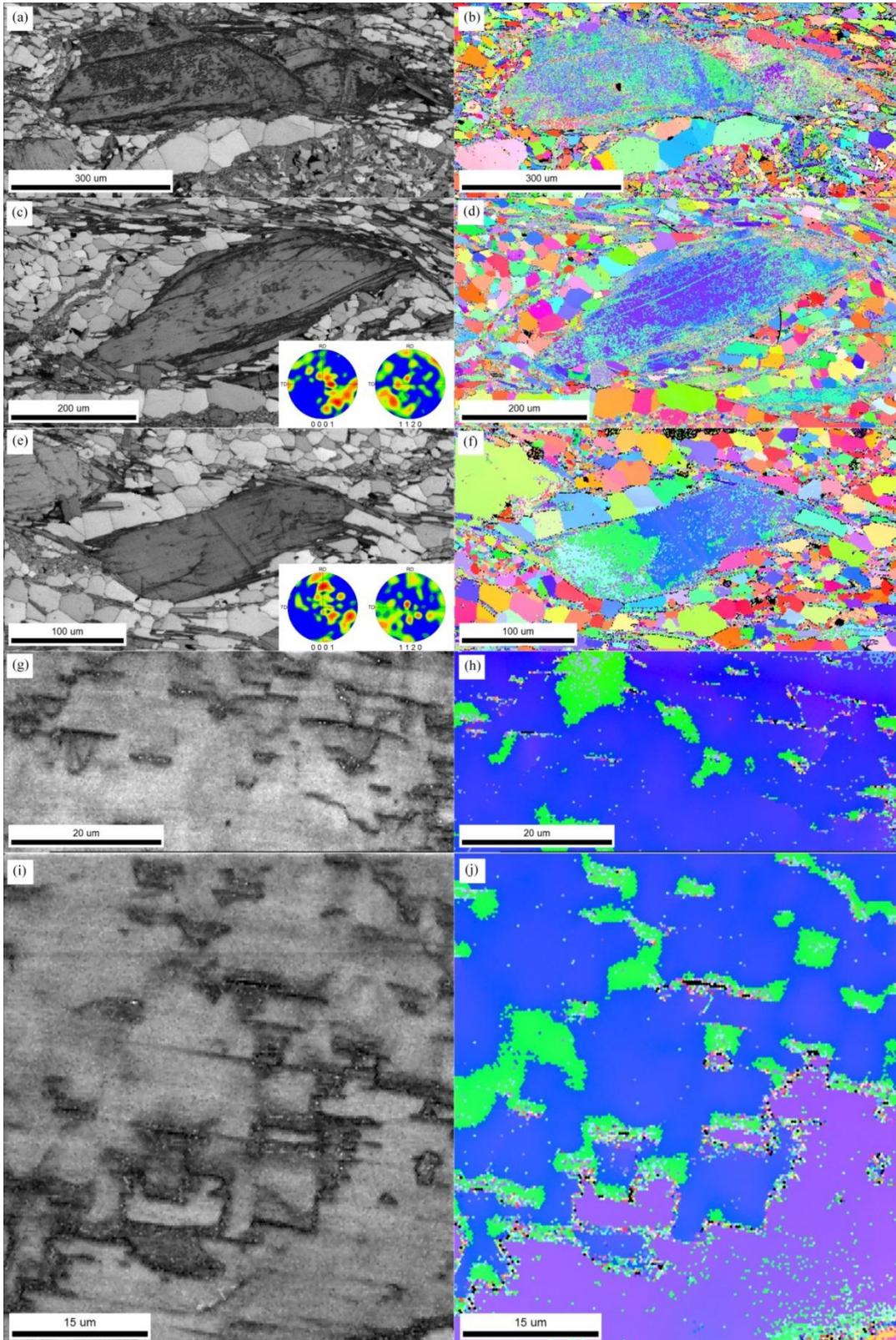


Figure 3.6 Remaining EBSD scans of muscovite clasts and microkinks in the ultramylonitic sample M1206. Image quality maps are presented in the left column (a,c,e,g,i) and corresponding inverse pole figure maps (IPF) are presented in the right column (b,d,f,h,j). Quartz textures in 2 cases are shown as insets in (c) and (e).

Supplementary data

Despite applying different settings during re-calculations of the analysed datasets, results of the EBSD scans, presented in Fig. 3.6, were generally poor. This is indicated by the inverse pole figure maps and the patchy color distribution within these, which indicates, that it was not possible for the software to find one single correct solution (i.e. crystal orientation). Additionally it is not expected, that these datasets provide more information, that are not covered by the datasets presented in paper #3. However, quartz textures presented in Fig. 3.6, generally confirm those presented in other (ultra)mylonitic rocks.

3.4 Sm/Nd whole rock results

In addition to the Rb/Sr data presented in paper #2, Sm/Nd ID-TIMS analyses of Permian meta-pegmatite whole rocks were also performed. These are presented below in Table 3.5.

Table 3.5 ID-TIMS Sm/Nd whole rock data for Permian meta-pegmatites from this study plus data from Habler et al. (2009), Thöni and Miller (2000), Thöni (2003) and Thöni and Miller (2000) for comparison.

Samples	Nd [ppm]	Sm [ppm]	$^{147}\text{Sm}/^{144}\text{Nd}$	1% error	$^{143}\text{Nd}/^{144}\text{Nd}$	error	Source
HM00305	0.841	0.269	0.19369	0.0019369	0.512092	0.000003	this study
M1217	0.472	0.160	0.20514	0.0020514	0.512234	0.000004	this study
M1203	1.397	0.386	0.16712	0.0016712	0.512054	0.000003	this study
M1206	5.558	1.748	0.19016	0.0019016	0.512365	0.000005	this study
HM28704	0.445	0.101	0.13746	0.0013746	0.512051	0.000006	Habler et al 2009
HM32304	3.229	1.730	0.32382	0.0032382	0.512407	0.000004	Habler et al 2009
95T06K	11.130	3.750	0.20360	0.0020360	0.512214	0.000011	Thöni and Miller 2000
00T4K	3.297	1.138	0.20870	0.0020870	0.512239	0.000008	Thöni 2003
00T1St	8.732	2.886	0.19980	0.0019980	0.512220	0.000005	Thöni 2003
93T23Ka	12.780	2.473	0.11700	0.0011700	0.512174	0.000009	Thöni and Miller 2000
93T24	28.217	5.850	0.12532	0.0012532	0.512098	0.000009	Thöni and Miller 2000
95T14K	5.703	2.268	0.24038	0.0024038	0.512201	0.000007	Thöni and Miller 2000
SPPCM	0.133	0.119	0.54211	0.0054211	0.512834	0.000025	Thöni and Miller 2000
965KWT	0.199	0.162	0.49356	0.0049356	0.512759	0.000031	Thöni and Miller 2000

Using all data, presented in Table 3.5, in one regression calculation, a poorly defined whole rock errorchron age of 272 ± 57 Ma is obtained, generally supporting a Permian formation age for the pegmatites. However, when only the data from this study (samples HM00305, M1217, M1203 and M1206; Table 3.5) are considered, the result is inconclusive. This might be related to different source materials for the pegmatites with different compositions or some late-stage alteration affecting the rare-earth element (REE) budget of the whole rocks. This could be, for example, reflected in the generally elevated REE contents of the ultramylonitic sample M1206. However, when the concentrations of Sm and Nd (Table 3.5) from the different samples of this study are viewed in the light of the finite strain of each sample, which increases in the order $M1217 < HM00305 < M1203 < M1206$, a positive correlation between the concentrations

Supplementary data

of these 2 elements and the overall finite strain of the respective Permian meta-pegmatite is revealed. However, such a correlation is not reflected by the ICP–MS data (see paper #2).

3.5 Mineral separate overview

Table 3.6 gives an overview on the existing mineral separates and whole rock powders, that were used for Rb/Sr and ICP–OES/MS analyses. Some of the separates were embedded in epoxy resin and also studied by scanning electron microscopy (SEM) and by electron microprobe analyses (EPMA). The amount of residual mineral separates is either characterised by “x” (enough for additional analysis) and “traces” (only a few mg). However, some of the material was completely used without any remaining material. Additional material, labelled 1, 2 and 3 is listed and can potentially be used for further analysis after some magnetic purification using the Frantz isodynamic magnetic separator.

Table 3.6 Mineral separate overview on existing material and applied methods

Sample No	Material	SEM	EPMA	Rb/Sr	ID-TIMS	ICP-OES/MS	residual
Meta-pegmatite M1210							
	TE-F0 whole-rock					x	>100 g
	TE-F1 Ms 250-450µm; nm 28V	x	x			x	x
	TE-F2 Ms 250-450µm; m 28V			x		x	x
	TE-F3 Ms >450µm; m 32V	x	x	x		x	x
	TE-F4 Ms >450µm; nm 42V	x	x			x	x
	TE-F5 Ms >450µm; m 42V	x	x			x	x
	1 BBWW, s>0.4mm (p>0.45 mm)						x
	2 BBWW, >0.45 mm, FM m 21V						x
	3 BBWW, 0.25-0.45 mm, FM m 16V						x
Meta-pegmatite M1217							
	TE-B0 whole-rock					x	>100 g
	TE-B1 Ms 250-450µm; nm 28V	x	x	x		x	x
	TE-B2 Ms 250-450µm; m 28V			x			traces
	TE-B3 Ms >450µm; m 32V	x	x	x		x	x
	TE-B4 Ms >450µm; nm 42V	x	x	x		x	x
	TE-B5 Ms >450µm; m 42V	x	x	x		x	x
	1 BBWW, s>0.4mm (p>0.45 mm)						x
	2 BBWW, >0.45 mm, FM m 18V						x
	3 BBWW, 0.25-0.45 mm, FM m 16V						x
Meta-pegmatite HM00305							
	TE-A0 whole-rock					x	>100 g
	TE-A1 Ms >250 µm (125-450); m 40V			x			traces
	TE-A2 Ms >250 µm (100-125); nm 40V			x			traces
	TE-A3 Ms >250 µm (125-450);n m 40V			x		x	x
Meta-pegmatite M1203							
	TE-C0 whole-rock					x	>100 g
	TE-C1 Ms 250-450µm; nm 28V	x	x	x		x	x
	TE-C2 Ms 250-450µm; m 28V	x	x	x		x	x
	TE-C3 Ms >450µm; m 32V	x	x	x		x	x
	TE-C4 Ms >450µm; nm 42V	x	x	x		x	x
	TE-C5 Ms >450µm; m 42V	x	x	x		x	x
	1 BBWW, s>0.4mm (p>0.45 mm)						x
	2 BBWW, >0.45 mm, FM m 21V						x
	3 BBWW, 0.25-0.45 mm, FM m 14V						x
Meta-pegmatite M1201							
	TE-E0 whole-rock					x	>100 g
	TE-E1 Ms 250-450µm; nm 28V	x	x			x	x
	TE-E2 Ms 250-450µm; m 28V			x		x	traces
	TE-E3 Ms >450µm; m 32V	x	x	x		x	x
	TE-E4 Ms >450µm; nm 42V	x	x	x		x	traces
	TE-E5 Ms >450µm; m 42V	x	x			x	x
	1 BBWW, s>0.4mm (p>0.45 mm)						x
	2 BBWW, >0.45 mm, FM m 21V						x
	3 BBWW, 0.25-0.45 mm, FM m 14V						x
Meta-pegmatite M1206							
	TE-D0 whole-rock			x		x	>100 g
	TE-D1 Ms >250; nm 20V			x		x	traces
	1 >0.25 mm, FM m 20V						
Metapelite HM07903							
	TE-G0 whole-rock			x			>100 g
	TE-G1 Bt 160-450 µm			x			x

3.6 References

- Habler, G., Thöni, M., Grasemann, B., 2009. Cretaceous metamorphism in the Austroalpine Matsch Unit (Eastern Alps): The interrelation between deformation and chemical equilibration processes. *Mineralogy and Petrology*, 97, 149–171.
- Thöni, M., Miller, C., 2000. Permo–Triassic pegmatites in the eo–Alpine eclogite–facies Koralpe complex, Austria: age and magma source constraints from mineral chemical, Rb–Sr and Sm–Nd isotope data. *Schweizerische mineralogische und petrographische Mitteilungen*, 80/2, 169–186.
- Thöni, M., 2003. Sm–Nd isotope systematics in garnet from different lithologies (Eastern Alps): age results, and an evaluation of potential problems for Sm–Nd garnet chronometry. *Chemical Geology*, 185/3–4, 255–281.

Abstract

The major focus of this thesis is on deformation–assisted re–equilibration phenomena and more specifically on the effects of deformation on Rb–Sr isotopic re–equilibration in muscovite. The selected approach includes a detailed microstructural and compositional analysis of the rock–forming minerals of Permian meta–pegmatites in order to characterize their deformation behaviour and related chemical alteration and to evaluate the behaviour of the bulk rock system during Cretaceous deformation. The link between deformation and the Rb–Sr isotope data of muscovite is established through the related major element composition.

EBSD–based microstructural and textural data show that dissolution–precipitation of albite is an important mechanism accommodating deformation at upper–greenschist facies conditions and that it is intimately related with grain–internal formation of (micro)kinks, cracks, low–angle boundaries, stylolites and chemical alteration. It is shown by the data that crystallographic anisotropies in albite exert a strong control on the development of specific deformation–related microstructures as indicated by the different deformation behaviour of two clasts with different angular relations between their (010) plane and the mylonitic foliation. Contrastingly, the deformation behaviour of muscovite is obviously not controlled by the relative orientation of crystallographic anisotropies with respect to the kinematic frame, except for the preferred orientation of the (001) planes. The Y–axis of shear flow seems to be the rotation axis for crystal lattice rotation, irrespective of the initial clast orientation.

Combined microstructural and mineral chemical analysis of the rock–forming minerals muscovite and albite feldspar indicate that significant portions of the Permian meta–pegmatites were affected by deformation, coupled with significant deformation–related chemical alteration of both, muscovite and albite feldspar. However, the data demonstrate that Rb–Sr isotopic data of muscovite obviously do not correlate with major element composition. Detailed results of the Rb–Sr isotopic analysis of several well–characterized grain size– and magnet–fractions of deformed Permian relic magmatic muscovite from single samples contest existing models of isotopic rehomogenization. The results demonstrate that a, presumably deformation–related, loss of total Sr has a significant effect on the $^{87}\text{Rb}/^{86}\text{Sr}$ ratios of muscovite without significant $^{87}\text{Sr}/^{86}\text{Sr}$ isotopic rehomogenization. The slopes of muscovite–internal ‘errorchrons’, which are constructed by up to five muscovite grain size– and magnet–

Abstract

fractions, obviously bracket the timing of the event that affected the geochronometer. Yet another point is the presence of at least one muscovite grain size– and magnet–fraction, typically the one with the lowest $^{87}\text{Rb}/^{86}\text{Sr}$ and $^{87}\text{Sr}/^{86}\text{Sr}$ ratios, in almost every sample that is interpreted to still reflect a Permo–Triassic formation or cooling age.

Investigations of different grain size– and magnet–fractions of muscovite from single samples provide a comprehensive dataset documenting significant systematic variations in the Rb–Sr isotopic system even at hand specimen scale. Furthermore, this study has demonstrated the dependence of major and trace element, and isotope distribution on local deformation and effective deformation mechanisms.

Zusammenfassung

Das Hauptaugenmerk dieser Arbeit liegt auf deformationsbezogenen Re-äquilibrierungserscheinungen und spezifischer auf den Effekten von Deformation auf Rb–Sr Äquilibrierung in Muskowit. Der gewählte Ansatz beinhaltet eine detaillierte Analyse der Mikrostrukturen und der Hauptelementzusammensetzung der gesteinsbildenden Minerale in Permischen Metapegmatiten, um deren Deformationsverhalten und die damit verbundene chemische Alteration, sowie das Verhalten der Gesamtgesteinssysteme während der Kretazischen Deformation zu evaluieren.

EBSD-basierte Mikrostruktur- und Texturdaten zeigen, dass dissolution–precipitation von Albit ein wesentlicher Deformationsmechanismus bei oberen grünschieferfaziellen Bedingungen ist und dass dieser eng mit korninterner Bildung von (Mikro)kinks, spröden Brüchen, Kleinwinkelkorngrenzen, Stylolithen und chemischer Alteration verbunden ist. Die Daten zeigen ausserdem, dass kristallographische Anisotropien in Albit einen starken Einfluss auf die Ausbildung bestimmter deformationsbezogener Mikrostrukturen haben. Dies ist in den unterschiedlichen Deformationsverhalten zweier Klasten mit unterschiedlichen Winkelbeziehungen zwischen deren (010) Fläche und der mylonitischen Foliation zu erkennen ist. Im Gegensatz dazu ist das Deformationsverhalten von Muskowit offensichtlich nicht durch die relative Orientierung kristallographischer Anisotropien zum kinematischen Rahmen kontrolliert, mit Ausnahme der Vorzugsorientierung der (001) Flächen. Die kinematische Y–Achse scheint unabhängig von der initialen Orientierung des Klasten die Rotationsachse für Kristallgitterrotationen zu sein.

Kombinierte mikrostrukturelle und mineralchemische Analysen der gesteinsbildenden Minerale Muskowit und Albit zeigen, dass ein bedeutender Anteil der Permischen Metapegmatite durch die Deformation beeinflusst wurde und dass dies mit signifikanten chemischen Alterationen einhergeht. Allerdings zeigen die Daten, dass Rb–Sr Isotopendaten von Muskowit offensichtlich nicht mit deren Hauptelementchemie korrelieren. Detaillierte Resultate der Rb–Sr Analyse von verschiedenen Korngrößen- und Magnetfraktionen von Muskowit stellen bestehende Modelle isotopischer Rehomogenisierung in Frage. Die Resultate demonstrieren einen wesentlichen Effekt von, vermutlich deformationsbezogenem, Verlust von Sr auf die $^{87}\text{Rb}/^{86}\text{Sr}$ Verhältnisse von Muskowit ohne eine signifikante $^{87}\text{Sr}/^{86}\text{Sr}$ Rehomogenisierung. Die Steigungen von

Zusammenfassung

Muskowit-internen 'Errorchronen' basierend auf bis zu 5 Korngrößen- und Magnetfraktionen, scheinen den Zeitpunkt des überprägenden Events einzugrenzen. Ein anderer wesentlicher Punkt ist die Präsenz von mindestens einer Korngrößen- und Magnetfraktion, typischerweise jene mit den niedrigsten $^{87}\text{Rb}/^{86}\text{Sr}$ und $^{87}\text{Sr}/^{86}\text{Sr}$ Verhältnissen, welche als Permotriassisches Bildungs- oder Abkühlalter interpretiert wird.

Zusammenfassend liefern die Untersuchungen von verschiedenen Korngrößen- und Magnetfraktionen von Muskowit einzelner Proben einen umfassenden Datensatz, welcher signifikante systematische Variationen im Rb-Sr Isotopensystem im Handstücksbereich dokumentiert. Ebenso zeigt diese Arbeit eine Abhängigkeit von Haupt- und Spurelement- und Isotopenverteilung von lokaler Deformation und effektiven Deformationsmechanismen.

Curriculum vitae

Curriculum vitae – Lebenslauf

1. Oktober 1985 Geburt in Mainz, Deutschland (Alter: 29)
- 1992 – 1996 Besuch der Grundschule Bodenheim, Deutschland
- 1996 – 2005 Besuch von weiterführenden Schulen in Nierstein und Mainz,
Deutschland
- März 2005 Allgemeine Hochschulreife (Abitur) am Schloß–Gymnasium
in Mainz, Deutschland
- 10/2005 – 06/2011 Studium der Geowissenschaften mit Schwerpunkten in den Fach–
bereichen Mineralogie, Petrologie und Tektonophysik
- 06/2011 Hochschulabschluß (Diplom) mit der Note 1,1 an der
Johannes Gutenberg–Universität in Mainz, Deutschland
Diplomarbeit in Fachbereich -Metamorphe Petrologie-
mit dem Titel:
„High–precision geobarometry across the Plattengneiss shear
zone in the Koralpe, Eastern Alps, Austria”
- 10/2011 – 10/2014 Doktoratsstudium an der Universität Wien
Dissertation: „The effect of strain heterogeneities on Rb–Sr and
Sm–Nd isotopic re–equilibration in minerals and rocks“
Betreuung: Univ. Prof. Mag. Dr. Rainer Abart